SATELLITE FORMATION DESIGN IN ORBITS OF HIGH ECCENTRICITY FOR MISSIONS WITH PERFORMANCE CRITERIA SPECIFIED OVER A REGION OF INTEREST

A Dissertation

by

CHRISTOPHER WILLIAM THOMAS ROSCOE

Submitted to the Office of Graduate Studies of
Texas A&M University
in partial fulfillment of the requirements for the degree of

DOCTOR OF PHILOSOPHY

Approved by:

Co-Chairs of Committee,	Srinivas R. Vadali
	Kyle T. Alfriend
Committee Members,	John L. Junkins
	Aniruddha Datta
Head of Department,	Rodney D. W. Bowersox

December 2012

Major Subject: Aerospace Engineering

ABSTRACT

Several methods are presented for the design of satellite formations for science missions in high-eccentricity reference orbits with quantifiable performance criteria specified throughout only a portion the orbit, called the Region of Interest (RoI). A modified form of the traditional average along-track drift minimization condition is introduced to account for the fact that performance criteria are only specified within the RoI, and a robust formation design algorithm (FDA) is defined to improve performance in the presence of formation initialization errors. Initial differential mean orbital elements are taken as the design variables and the Gim-Alfriend state transition matrix (G-A STM) is used for relative motion propagation. Using mean elements and the G-A STM allows for explicit inclusion of J_2 perturbation effects in the design process. The methods are applied to the complete formation design problem of the NASA Magnetospheric Multiscale (MMS) mission and results are verified using the NASA General Mission Analysis Tool (GMAT). Since satellite formations in high-eccentricity orbits will spend long times at high altitude, third-body perturbations are an important design consideration as well. A detailed analytical analysis of third-body perturbation effects on satellite formations is also performed and averaged dynamics are derived for the particular case of the lunar perturbation. Numerical results of the lunar perturbation analysis are obtained for the example application of the MMS mission and verified in GMAT.

ACKNOWLEDGEMENTS

I would first like to thank my advisors, Dr. Srinivas R. Vadali and Dr. Kyle T. Alfriend, for all of the support and guidance they have given me. They drove me to be passionate in my research, to always challenge myself, and to tackle the tough problems. Whenever I needed advice, Dr. Vadali's door was open, and his patient, caring, and humble attitude has been an inspiration. Dr. Alfriend's vast knowledge of spacecraft dynamics and control and practical experience have been invaluable resources as my research evolved and as I consider my future.

I would also like to thank Dr. Junkins and Dr. Datta for serving on my doctoral committee and for teaching me about dynamics and control. Learning celestial mechanics and estimation from Dr. Junkins was an awe-inspiring experience and I am truly grateful for having had the opportunity; his readiness to share his advice, stories, and expertise with me any time has been one of the highlights of my time at Texas A&M University. Thank you to NASA for providing funding and especially to Trevor Williams for his technical input. Special thanks go as well to Karen Knabe and Lisa Jordan, the unsung heroes of the department and the dynamics and control group, without whom I surely would never have succeeded.

Thank you to my family—my parents, grandfather, aunt, and brothers and sisters—as well as my Texas family for all of the love and support you have given me. Thanks also to my friends and colleagues for your camaraderie and good humour throughout my studies. Finally, thank you, as ever, to Caitlin for the limitless patience, understanding, support, and love you showed while we were apart.

TABLE OF CONTENTS

Page

CHAPTER Page

LIST OF FIGURES

FIGURE Page

LIST OF TABLES

CHAPTER I

INTRODUCTION

Satellite formation flying is a key area of research in modern spacecraft dynamics and control. The prospect of long duration formation flying missions offers several advantages over large, single-satellite ones, including increased reliability and upgradeability and lower overall mission costs. This concept is particularly attractive for applications requiring large apertures or distributed systems, for which a properly controlled formation could provide a synthetic aperture to emulate a system such as a large antenna or telescope for high resolution imaging, radio or optical interferometry, or magnetic and electrical interaction studies [1].

Numerous formation flying missions have been conceived over the past two decades and several have flown successfully. The European Space Agency (ESA) Cluster mission [2–4], consisting of four identical spacecraft in a highly eccentric orbit, was launched in 2000 and has provided nearly a decade's worth of valuable scientific information about the effects of the solar wind on the Earth's magnetosphere. In 2010, the German Aerospace Center (DLR) TanDEM-X satellite [5] was launched as an extension of the TerraSAR-X mission (previously launched in 2007) [6], joining it in close formation to perform synthetic aperture radar interferometry to generate a high-precision digital elevation model of the Earth. The PRISMA mission [7,8] was a two-satellite ESA formation flying technology demonstration experiment launched in 2010 and has successfully performed proximity operations and validated several key technologies and algorithms.

Other missions are currently in different stages of development around the world as well. The University of Toronto's CanX-4&5 dual nanosatellite mission (undergoing final assembly and testing) [9] consists of two satellites designed to demonstrate enabling technologies for low-cost, autonomous, precision formation flight. The JC2Sat-FF mission (in the intermediate design and assembly phase) [10] is a joint collaboration between the Canadian Space Agency (CSA) and the Japan Aerospace Exploration Agency (JAXA) to investigate the feasibility of autonomous formation control using aerodynamic differential drag, as well as serving as a platform to test newly developed nanosatellite instrumentation. The NASA Magnetospheric Multiscale (MMS) mission (scheduled for launch in 2014) [11] is a four-satellite formation flying mission designed to study magnetic reconnection, charged particle acceleration, and turbulence in key boundary regions of the Earth's magnetosphere, expanding on the results of the Cluster mission. A detailed survey of some of the most prominent ESA and NASA missions can be found in Chapter 1 of Ref. 12.

I.A. Literature Review

The need for accurate analytical models to solve the problem of satellite relative motion has been addressed in the astrodynamics literature by a wide variety of researchers over the past one and a half centuries. Analytical models have many advantages over brute force, numerical simulations, such as instant adaptability to different problems, fast simulation, and most importantly the physical insight that can be gleaned from the equations themselves. The first such "formation flying" analysis was performed by Hill [13] in 1878, whose seminal study investigated the

relative motion of the Moon and the Earth. Clohessy and Wiltshire [14] built on Hill's work in 1960 to solve the rendezvous and docking problem for the Apollo program. The resulting equations, known as the Hill-Clohessy-Wiltshire (HCW) equations, assume an unperturbed, Keplerian, circular reference orbit for the satellites, which can be sufficient over short time spans for certain applications, but is generally unacceptable for long duration formation flying missions. In addition, it is assumed that the satellites are sufficiently close to one another that the relative motion can be linearized about the size of the reference orbit.

Some additional efforts were made by London [15] in 1963 and Anthony and Sasaki [16] in 1965 to extend the HCW equations to include second-order terms from the relative motion linearization and first-order eccentricity terms. The exact linearized equations of relative motion in eccentric reference orbits with time as the independent variable were derived by de Vries [17] in 1963, along with an approximate solution. The relative motion problem in eccentric reference orbits with respect to the orbital anomalies instead of time was addressed independently by Lawden [18] in 1963 and Tschauner and Hempel [19] in 1965. The two solutions were similar, but the Tschauner-Hempel (TH) equations were not well-known in North America around that time. The TH equations were modified by Tschauner [20] in 1967, and the original form of Lawden's equations was modified by Carter [21] in 1990 to remove a singularity occurring when the true anomaly is an integer multiple of π. In 1967, Euler and Shulman [22] extended the TH equations to include second-order nonlinear terms but claimed that the resulting equations could not be solved analytically.

An excellent survey of the work performed in this area over the next 30 years was

presented by Carter [23] in 1998. This work mainly addressed various applications of the rendezvous problem as well as some early attempts at finding a linear state transition matrix (STM) for the relative motion. However, significant progress was not made until the 2000s when the long duration formation flying concept gained wide interest. In 2000, Melton [24] computed the STM for near-circular orbits as an explicit function of time using a series expansion in eccentricity. In 2002, Inalham, Tillerson, and How [25] presented conditions for the initialization of periodic formations in reference orbits of arbitrary eccentricity to modify the well-known periodic solutions of the HCW equations, valid at perigee of the reference orbit. Sengupta and Vadali [26] in 2007 completed this analysis by defining a simple linear periodicity constraint for arbitrary eccentricity and epoch, as well as a useful parameterization for solutions of the TH equations (analogous to the constants of the HCW equations). Broucke [27] in 2003 derived the STM for arbitrary reference orbit eccentricity as a function of time using the fundamental solution matrix, based on the equations of de Vries [17]. In the same year, Yamanaka and Ankersen [28] found another STM for eccentric reference orbits using a similar method but with true anomaly as the independent variable.

Based on the preceding studies, the linearized Keplerian relative motion problem is essentially solved, assuming small separations between the satellites making up the formation and including arbitrary eccentricity. However, long duration formations are impossible to design without taking into account the effect of perturbations to the Keplerian motion. Therefore, much of the recent research is focused on accounting for disturbing forces such as the J_2 oblateness perturbation, atmospheric drag, third-

body effects, and solar radiation pressure. J_2 is the dominant perturbation in low-Earth orbit (LEO) and medium-Earth orbit (MEO), followed by atmospheric drag in LEO and lunisolar effects in MEO. In the upper MEO region and high-Earth orbit (HEO), third-body effects can be of the same order of magnitude as J_2. Solar radiation pressure can also be an important factor in MEO and HEO for satellites with large surface areas or solar panels (including solar sails).

In 2001, Schaub and Alfriend [29] and Vadali, Vaddi, and Alfriend [30] presented conditions for establishing J_2-invariant relative orbits using differential mean orbital elements, including an important constraint (known as the "along-track drift condition") on the differential mean semimajor axis, which minimizes the average along-track drift between a pair of satellites in the presence of J_2. In 2003, Gim and Alfriend [31] derived the STM (known as the G-A STM) of relative motion including arbitrary eccentricity and first-order absolute and differential J_2 effects using differential mean orbital elements and what they termed the "geometric method." This solution is valid for both circular and eccentric orbits but contains a singularity when the orbit has zero inclination; therefore, Gim and Alfriend [32] in 2005 removed this singularity by again using the geometric method to derive the STM using equinoctial elements. Vadali [33] in 2002 and Sengupta, Vadali, and Alfriend [34] in 2004 used a unit sphere approach, in which the motion of the two satellites is projected onto a unit sphere by normalizing their positions by their orbit radii, to solve the perturbed relative motion problem. Yan et al. [35] in 2004 derive the relative motion STM based on this approach.

Differential orbital elements are a natural and convenient choice for designing

general formations [36–41], since they are constants of the unperturbed motion, and using mean elements allows for the explicit inclusion of secular effects due to J_2. However, with these variables it can be difficult to visualize the relative orbit geometry, which makes it challenging to design a formation directly using differential orbital elements when geometric constraints are imposed. Schaub [39] in 2004 addresses this problem by developing simple, linearized estimates of the relative orbit motion in terms of classical orbital element differences. In this formulation, it is very easy to see the geometric effect of changing the initial conditions of various differential orbital elements as well as visualizing the effects of perturbations such as J_2.

In 2007, Hamel and de Lafontaine [42] extended this approach to develop an STM similar to that of Gim and Alfriend [31] but with slightly less complex expressions and implementation based on certain simplifying assumptions. In the same year, Gurfil [43] derived generalized solutions to the relative motion problem in the presence of arbitrary perturbations using non-osculating differential orbital elements and discovered several new types of J_2-invariant orbits. In 2008, Sengupta, Vadali, and Alfriend [44] presented expressions for J_2-perturbed averaged relative motion using orbital elements which differ slightly from results obtained using mean element theory because the averaging in this case is performed after the motion is linearized about the reference orbit.

Atmospheric drag is highly dependent on satellite geometry and attitude, so the differential effect of drag on a satellite formation depends on both differences in satellite geometry and relative attitude. Differential drag, therefore, has long been considered a potential control force for formationkeeping in LEO. Leonard, Hollis-

ter, and Bergmann [45] originally proposed this concept in 1989 and developed the appropriate equations and control algorithm for a circular reference orbit. Humi and Carter [46] in 2002 considered the relative motion problem in an eccentric reference orbit for the case of linear drag. Later that year, Carter and Humi [47] modified the HCW equations to include quadratic drag (for a circular reference orbit). In 2008, Bevilacqua and Romano [48] derived equations for rendezvous maneuvers using differential drag in a circular reference orbit under the influence of the J_2 perturbation.

The effect of the third-body perturbation on formations in particular has not been studied much in the literature; however, the effects of lunisolar perturbations on general satellites have been studied extensively. The analysis uses perturbation methods and averaging, following a similar approach to the Brouwer theory for the zonal harmonics [49]. The first lunisolar disturbing function was developed in 1959 by Kozai [50] and expanded by Musen, Bailie, and Upton [51] in 1961. The previous analysis was generalized by Kaula [52] in 1962 and revisited in 1974 by Giacaglia [53], who obtained the lunar disturbing function using orbital elements. In 1973, an alternate method for the calculation of lunisolar disturbances was derived by Kozai [54] using orbital elements for the satellite and Cartesian coordinates for the disturbing bodies. A simplified, but more analytically attractive, model was developed by Prado [55] in 2003 based on the assumptions of the circular restricted three-body problem. Using a similar formulation, Broucke [56] in the same year investigated the effect of lunisolar perturbations on high-altitude satellites in nearly circular orbits. In 2012, Lara, San Juan, and Lòpez [57] used canonical perturbation theory to solve a higher-order lunisolar problem, including J_2, J_3, fifth-order lunar terms, and

second-order solar terms. The effect of this perturbation on satellite formations has been investigated numerically in modern research, such as McLaughlin et al. [58] in 2002 and Wnuk and Golebiewska [59] in 2005, but analytical analyses are absent.

Similarly to atmospheric drag, the use of solar radiation pressure has been advocated recently as a method for controlling satellite formations by using reflective solar wings or sails. Williams and Wang [60] first proposed the concept of formation flying using differential solar radiation pressure in 2002 and derived the governing relative motion equations for eccentric orbits. In 2003, Wang and Williams [61] derived an optimal solar wing steering law for formation-keeping in the presence of J_2. More recently, Gong, Yunfeng, and Li [62] in 2011 investigated the prospect of near-Earth solar sail formation flying, which naturally uses solar radiation pressure for propulsion and differential solar radiation pressure for formation control.

Errors due to linearizing the relative motion about the reference orbit depend on the ratio of the distance between the satellites to the size of the reference orbit. Karlgaard and Lutze [63] in 2002 and Richardson and Mitchell [64] in 2003 obtained conditions for initializing periodic formations which account for second- and third-order nonlinear terms in circular reference orbits. Vaddi, Vadali, and Alfriend [65] in 2003 derived periodicity conditions to account for both nonlinearity and eccentricity, but the conditions are only valid for small eccentricities. In 2005, Gurfil [66] derived a periodicity condition for the full nonlinear problem based on an energy-matching approach, the solution of which requires numerical iteration. In 2006, Sengupta, Sharma, and Vadali [67] obtained periodicity conditions valid for second-order nonlinearity and arbitrary eccentricity, essentially solving the equations of Euler and

Shulman [22].

These errors also depend on the choice of coordinates with which the linearization is performed: Junkins, Akella, and Alfriend [68] in 1996 and Junkins [69] in 2003 demonstrated that using differential orbital elements is more accurate than using either Cartesian or curvilinear coordinates. In 2002, Alfriend, Yan, and Vadali [70] and Alfriend and Yan [38] used differential orbital elements to address the nonlinear relative motion problem. Sengupta, Vadali, and Alfriend [71] in 2007 extended this approach to derive a state transition tensor for perturbed relative motion including second-order nonlinear effects.

Numerous papers have been written on the application of the various relative motion formulations and solutions to formation flying guidance and control, both for specific missions and general problems; therefore, only a selection will be described here. For example, Alfriend, Schaub, and Gim [72] in 2000 investigated the effects of reference orbit eccentricity, nonlinearity, and the J_2 perturbation on errors in relative motion prediction and fuel consumption for formation establishment and maintenance when formation guidance is accomplished using the HCW equations. Also in 2000, Schaub et al. [73] presented two nonlinear feedback control laws for J_2-invariant formation reestablishment using differential mean orbital elements. Alfriend and Yan [74] in 2005 compared the accuracy of several different relative motion theories based on a modeling error index derived therein.

In 2006, D'Amico and Montenbruck [75] described a strategy of passive perturbation rejection and collision avoidance for synthetic apertures using eccentricity/inclination vector separation, originally developed for geostationary satellites [76],

for the near-circular, LEO TanDEM-X/TerraSAR-X mission. Griffith, Singh, and How [77] in 2007 presented a method of optimally designing satellite formations for tracking missions using differential orbital elements by penalizing expected maintenance maneuver fuel expenditure due to relative drift caused by J_2. In the same year, Eyer et al. [78] defined a control algorithm using the HCW equations for the near-circular, LEO CanX-4&5 precision formation flying demonstration mission. In 2009, Roscoe [79] investigated the problem of formation reconfiguration and recovery for the CanX-4&5 mission using a number of different relative motion models. Also in 2009, Yan et al. [80] derived a method of optimally selecting initial differential elements for a formation using the G-A STM along with a least-squares approach.

I.B. Dissertation Outline

This dissertation deals with the problem of optimal satellite formation design for missions with quantifiable science return criteria. In 2008, Hughes [81] presented a general method for optimal guidance of such missions using initial Cartesian relative states as design variables and direct numerical integration for state propagation. In the present work, the design variables of interest are the initial differential mean orbital elements and propagation will be accomplished analytically using the G-A STM. Using this method provides for a very efficient optimization scheme for the formation design problem, including providing analytical gradients with respect to the design variables as trivial byproducts of the state propagation process. More specifically, this dissertation will focus on long-duration design problems in reference orbits of high eccentricity, thus spanning a wide range of altitudes, with performance

criteria prescribed on a specific segment of the orbit: the Region of Interest (RoI).

In Chapter II, the concept of "formation flying" will be precisely defined, and the governing dynamics and equations will be introduced. In Chapter III, the concepts of "performance criteria" and "formation stability" will be quantified and a number of general formation design techniques will be presented. In particular, two nominal formation design algorithms (FDAs), the single-orbit constrained (SOC) optimization and the multi-orbit unconstrained (MOU) optimization, and a robust FDA, using a stochastic optimization approach, will be introduced, as well as conditions to ensure long-term stability and a method for initializing a tetrahedron formation. A simple single-variable example problem will be used to illustrate the effects of these different approaches.

In Chapter IV, the methods of Chapter III will be tested by applying them to the formation design problem of the MMS mission. Complete formation design results (nominal and robust) will be presented for both phases of MMS, including detailed analyses of long-term stability with respect to the J_2 perturbation and formation initialization errors. These results, which will be computed using the G-A STM, will be verified using the NASA General Mission Analysis Tool (GMAT). In addition, a physical interpretation of the various formation design methods will be offered, which yields valuable insight into the geometry of formations exhibiting desirable characteristics such as good long-term nominal performance and robustness.

Finally, since satellite formations in highly eccentric reference orbits will spend significant amounts of time in high-altitude regimes, it is expected that third-body perturbations will also be important considerations for the formation design pro-

cess. Therefore, Chapter V will provide a detailed, analytical analysis of third-body perturbation effects on satellite formations for the particular case of the lunar perturbation. Averaged absolute and differential effects of the lunar perturbation will be derived, including the transformation between the osculating and lunar-averaged elements. Without this transformation, the method of averaging produces inaccurate results over time due to the effect of discrepancies in initial conditions. Numerical results for lunar perturbation effects on the MMS mission will be presented and verified in GMAT, and the effects of this perturbation on formation performance will be compared to those of J_2.

CHAPTER II

DYNAMICS

The precise definition of "satellite formation flying" is not something that is universally agreed upon in the spacecraft dynamics and control literature. According to Ref. 12, most of the space community would agree to the NASA Goddard Space Flight Center (GSFC) definition, "The tracking or maintenance of a desired relative separation, orientation or position between or among spacecraft." This definition makes a distinction between satellite formations and the broader category of "distributed space systems," in which multiple satellites work cooperatively but not necessarily in close proximity or with relative separation, orientation, or position requirements.

The present work involves the design of formations of multiple satellites in arbitrary Earth reference orbits, in particular high-altitude and high-eccentricity reference orbits. One satellite (0) is designated the "chief" or "reference" satellite (to follow the reference orbit). The chief need not be an actual satellite but may instead be taken as a fictitious reference point, for example the formation center of mass. The remaining satellites $(1, 2, \ldots, n)$ are designated the "deputies" and their relative states are the variables which are to be designed. The satellites are assumed to be sufficiently close to one another compared to the size of the reference orbit at all times so that the motion of the deputies can be linearized about the motion of the chief. Therefore, the dynamics of the system will be completely described by the reference orbit and the relative or "differential" states of the deputies to this orbit.

II.A. Reference Orbit

The reference orbit is characterized by six independent parameters which define its size, orientation, and initial phase. Many sets of parameters, called orbital elements, are possible—for examples, see Battin [82] or Schaub and Junkins [83]. Three sets of elements will be referred to in the present work: the classical orbital elements $(a, e, i, \Omega, \omega, M_0)$, defined in Table II.1; the non-singular orbital elements $(a, \theta, i, q_1, q_2, \Omega)$, where $\theta = f + \omega$ is the true argument of latitude, f is the true anomaly, and $q_1 = e\cos\omega$ and $q_2 = e\sin\omega$ are the orbit plane components of the eccentricity vector; and the Delaunay elements (l, g, h, L, G, H), which will be defined in Chapter V.

The non-singular elements are sometimes chosen instead of the classical elements because they are not singular in the case of a circular orbit; however, they are still singular for equatorial orbits. All of the orbital elements are constants of the unperturbed (Keplerian) motion with the exception of the anomalies f (and consequently θ) and l, which define instantaneous position on the orbit ellipse.

The orbital, or perifocal, reference frame, $\mathcal{O}$, is related to the geocentric inertial reference frame, $\mathcal{I}$, by a 3-1-3 Euler rotation sequence through the angles Ω, i, and

Table II.1. The classical orbital elements.

Element	Description
a	Semimajor axis
e	Eccentricity
i	Inclination
Ω	Right ascension of the ascending node
ω	Argument of periapsis
M_0	Initial mean anomaly

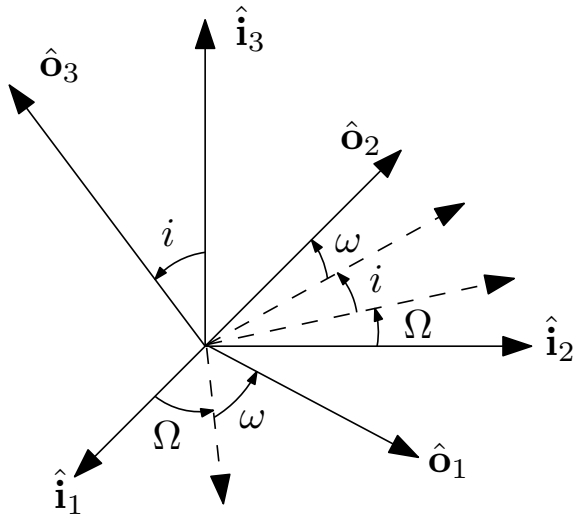

Figure II.1. Rotation from inertial to orbital reference frame.

ω, as shown in Figure II.1,

$$\begin{aligned}\mathbf{C}_{oi} &= \mathbf{C}_3(\omega)\mathbf{C}_1(i)\mathbf{C}_3(\Omega) \\ &= \begin{bmatrix} c_\omega c_\Omega - s_\omega c_i s_\Omega & c_\omega s_\Omega + s_\omega c_i c_\Omega & s_\omega s_i \\ -s_\omega c_\Omega - c_\omega c_i s_\Omega & -s_\omega s_\Omega + c_\omega c_i c_\Omega & c_\omega s_i \\ s_i s_\Omega & -s_i c_\Omega & c_i \end{bmatrix}\end{aligned} \tag{2.1}$$

where $\mathbf{C}_i(\cdot)$ is the principal rotation matrix about the ith axis, $s_\gamma = \sin\gamma$, and $c_\gamma = \cos\gamma$.

A Keplerian orbit then forms an ellipse lying in the $\hat{\mathbf{o}}_1$-$\hat{\mathbf{o}}_2$ plane with $\hat{\mathbf{o}}_1$ in the direction of periapsis. The geometry of the orbit ellipse is shown in Figure II.2 along with numerous common orbit/ellipse parameters. a is the half-length of the major axis and e is the ratio of the distance between the center of the ellipse and the focus F to the length of the semimajor axis. The other parameters shown in Figure II.2 are defined in Table II.2, many of which can be obtained directly from the ellipse

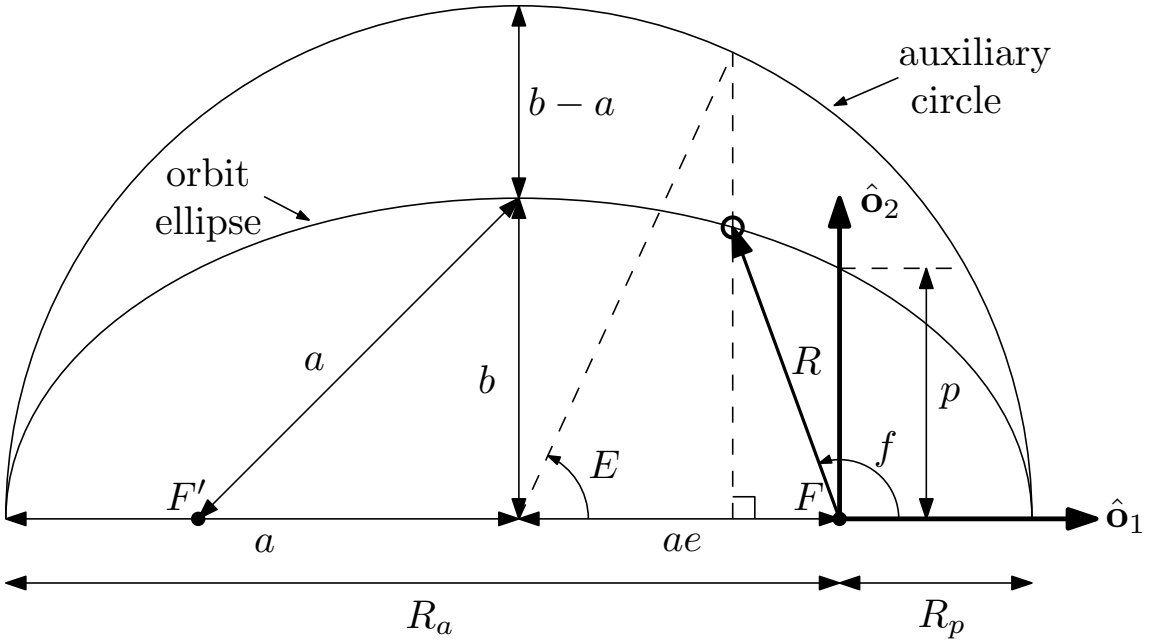

Figure II.2. Orbit ellipse geometry.

geometry:

$$b = a\sqrt{1 - e^2} \tag{2.2}$$

$$p = a\left(1 - e^2\right) \tag{2.3}$$

$$R_p = a\left(1 - e\right) \tag{2.4}$$

$$R_a = a\left(1 + e\right) \tag{2.5}$$

Position in the orbit is defined by R and f, which are related by the orbit equation:

$$R = \frac{p}{1 + e\cos f} \tag{2.6}$$

Alternatively, R can be expressed in terms of the eccentric anomaly E,

$$R = a\left(1 - e\cos E\right) \tag{2.7}$$

Table II.2. Miscellaneous orbital parameters.

Parameter	Description
b	Semiminor axis
p	Semilatus rectum
R	Orbit radius
R_p	Periapsis distance
R_a	Apoapsis distance
E	Eccentric anomaly

where f and E are related by the expressions

$$\cos f = \frac{\cos E - e}{1 - e\cos E} \tag{2.8}$$

$$\sin f = \frac{\sqrt{1-e^2}\sin E}{1 - e\cos E} \tag{2.9}$$

The instantaneous rates of change of f and E are

$$\dot{f} = \frac{\sqrt{\mu p}}{R^2} \tag{2.10}$$

$$\dot{E} = \frac{n}{1 - e\cos E} \tag{2.11}$$

where $\mu = 3.98593 \times 10^{14}$ m^3/s^2 is the geocentric gravitational constant and n is the mean motion,

$$n = \sqrt{\frac{\mu}{a^3}} \tag{2.12}$$

but the anomalies are more conveniently related to time through Kepler's equation

$$M = M_0 + nt = E - e\sin E \tag{2.13}$$

in which M is the mean anomaly. Finally, the orbit period is

$$T = \frac{2\pi}{n} \tag{2.14}$$

the magnitude of the orbit angular momentum is

$$h = \sqrt{\mu p} \tag{2.15}$$

and the useful parameter η is defined as the positive root of

$$\eta^2 = 1 - e^2 \tag{2.16}$$

II.A.1. Osculating and Mean Orbital Elements

Small disturbances to the spherical gravity field of the Earth will introduce perturbations to the elliptical, Keplerian motion. At any point in time, a set of orbital elements can be found to instantaneously describe the perturbed motion according to the previous equations—such a set of elements is called "osculating" because it just touches (or "kisses") the perturbed orbit. Computing or collecting the osculating orbital elements over time will precisely describe the motion at any point in the orbit, but the variables will exhibit small, rapid oscillations which make them difficult to propagate efficiently (such nonlinearity will necessarily require numerical integration techniques).

Brouwer [49] in 1959 used perturbation theory and the method of averaging to address this problem for an oblate Earth, solving the problem for the J_2–J_5 perturbations. The main part of that work applies to the J_2 perturbation which, as mentioned in Chapter I, is the primary perturbation for Earth-orbiting satellites. Brouwer theory removes the short- and long-period oscillations from the dynamics, leaving only secular variations due to J_2. The resulting transformed orbital elements are called the "mean" elements; with the oscillations removed, the mean elements a, e, and i are constant and Ω, ω, and M vary linearly in time:

$$\dot{\Omega} = -\frac{3}{2} J_2 n \left(\frac{R_e}{p}\right)^2 \cos i \tag{2.17}$$

$$\dot{\omega} = \frac{3}{4} J_2 n \left(\frac{R_e}{p}\right)^2 \left(5\cos^2 i - 1\right) \tag{2.18}$$

$$\dot{M} = n + \frac{3}{4} J_2 n \left(\frac{R_e}{p}\right)^2 \eta \left(3\cos^2 i - 1\right) \tag{2.19}$$

where the second zonal harmonic coefficient is $J_2 = 1.08263 \times 10^{-3}$ and the Earth's equatorial radius is $R_e = 6378.15$ km.

Because of the simplicity of the dynamics, these elements are very useful for orbit propagation and formation design. However, to obtain a precise description of the perturbed orbit motion at a given time the mean elements must first be transformed into osculating elements before applying the previous equations. For the remainder of the present work, all orbital elements mentioned will refer to mean orbital elements unless noted otherwise, with the exception of Chapter V which deals specifically with third-body perturbations.

II.B. Equations of Motion

The acceleration of a satellite with respect to Earth as the primary body is

$$\ddot{\mathbf{R}} = \underbrace{-\frac{\mu}{R^3}\mathbf{R}}_{\mathbf{f}_g} + \mathbf{f}_{\text{dis}} \tag{2.20}$$

where $\mathbf{R}$ is the position of the satellite relative to Earth, $\mathbf{f}_g$ is the Keplerian acceleration, and $\mathbf{f}_{\text{dis}}$ is the acceleration due to disturbances to the spherical gravity field of the Earth. If all forces are conservative, the gravitational potential acting on the satellite can be written as

$$V = -\frac{\mu}{R} - R_{\text{dis}} \tag{2.21}$$

where R_{dis} is the disturbing potential and such that

$$\ddot{\mathbf{R}} = -\nabla V \tag{2.22}$$

The two disturbing forces of interest in the present work are the primary Earth oblateness, or J_2, perturbation and the third-body gravitational perturbation. As noted in Chapter I, J_2 is the dominant perturbation in low-Earth orbit (LEO) and medium-Earth orbit (MEO), and in upper MEO and high-Earth orbit (HEO), third-body effects can be of the same order of magnitude.

II.B.1. J_2 Perturbation

Each of these disturbing forces is conservative and can be written in the form of a potential. The disturbing potential due to J_2 is [82]

$$R_{J_2} = -\frac{\mu}{R} J_2 \left(\frac{R_e}{R}\right)^2 P_2\left(\cos\phi\right) \tag{2.23}$$

where $P_k\left(\cdot\right)$ is the kth Legendre polynomial with

$$P_2\left(\gamma\right) = \frac{1}{2}\left(3\gamma^2 - 1\right) \tag{2.24}$$

and ϕ is the colatitude of the satellite in frame $\mathcal{I}$. That is, it is the angle between the satellite's position vector and $\hat{\mathbf{i}}_3$. In terms of orbital elements, $\cos\phi$ can be expressed

$$\cos\phi = \sin\theta \sin i \tag{2.25}$$

Therefore, Eq. (2.23) can also be written

$$R_{J_2} = -\frac{1}{2}\frac{\mu}{R^3} J_2 R_e^2 \left(3\sin^2\theta \sin^2 i - 1\right) \tag{2.26}$$

II.B.2. Third-Body Perturbation

The disturbing acceleration acting on a satellite in Earth orbit due to an additional celestial body is [82]

$$\mathbf{f}_{3\text{body}} = Gm_2\left(\frac{1}{d^3}\mathbf{d} - \frac{1}{R'^3}\mathbf{R}'\right) \tag{2.27}$$

where $\mathbf{d}$ is the position of the third body relative to the satellite, $\mathbf{R}'$ is its position relative to Earth, m_1 is the mass of the Earth, m_2 is the mass of the body, and G is the universal gravitational constant, assuming that the mass of the satellite is small compared to m_1 and m_2. In potential form, this can be written

$$R_{3\text{body}} = \mu' G\left(m_1 + m_2\right)\left(\frac{1}{d} - \frac{1}{R'^3}\mathbf{R}\cdot\mathbf{R}'\right) \tag{2.28}$$

where

$$\mu' = \frac{m_2}{m_1 + m_2} \tag{2.29}$$

The geometry of the system is shown in Figure II.3, therefore applying the cosine law, with S denoting the angle between the third body and the satellite as seen from

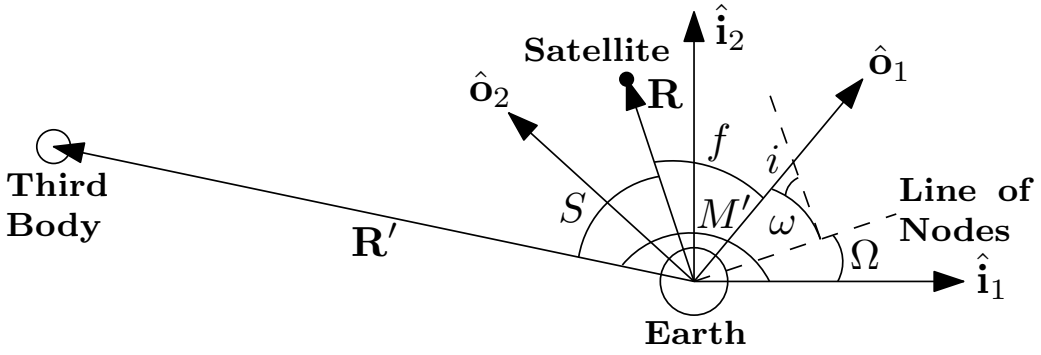

Figure II.3. Geometry of the restricted three-body problem.

the Earth, yields the relation

$$d^2 = R^2 + R'^2 - 2RR' \cos S \tag{2.30}$$

Note that Figure II.3 is valid for any arbitrary third-body orbit (with respect to the Earth), except for the illustration of the angle M', the mean anomaly of the body, which is only valid when its orbit is circular and equatorial. Using Eq. (2.30), Eq. (2.28) becomes

$$R_{3\text{body}} = \mu' G\left(m_1 + m_2\right)\left(\frac{1}{\sqrt{R^2 + R'^2 - 2RR'\cos S}} - \frac{R}{R'^2}\cos S\right) \tag{2.31}$$

Assuming that the satellite is much closer to the Earth than to the third body, the quantity R/R' will be small. Expanding Eq. (2.31) in Legendre polynomials about this quantity, the disturbing potential can be rewritten in the more convenient form,

$$R_{3\text{body}} = \frac{\mu' n'^2 a'^3}{R'}\left[1 + \sum_{k=2}^{\infty}\left(\frac{R}{R'}\right)^k P_k\left(\cos S\right)\right] \tag{2.32}$$

where n' and a' are the osculating mean motion and semimajor axis, respectively, of the third body's reference orbit. These quantities obey the relation,

$$n'^2 a'^3 = G\left(m_1 + m_2\right) \tag{2.33}$$

Since the first term in Eq. (2.32) does not depend on the position of the satellite it can be omitted. If only the $k = 2$ term in the summation is retained, a simplified disturbing potential is obtained:

$$R_{3\text{body}} = \frac{1}{2}\frac{\mu' n'^2 a'^3}{R'}\left(\frac{R}{R'}\right)^2\left(3\cos^2 S - 1\right) \tag{2.34}$$

Further simplification can be performed if the third body is assumed to be in a circular, equatorial orbit about the Earth (that is in the $\hat{\mathbf{i}}_1$-$\hat{\mathbf{i}}_2$ plane). Referring again

to Figure II.3, the $\cos S$ term can now be determined from the orbital elements of the satellite and the mean anomaly of the third body:

$$\cos S = \cos(\omega + f)\cos(M' - \Omega) + \sin(\omega + f)\cos i \sin(M' - \Omega) \tag{2.35}$$

$$= \alpha \cos f + \beta \sin f \tag{2.36}$$

where

$$\alpha = \cos\omega \cos(M' - \Omega) + \sin\omega \cos i \sin(M' - \Omega) \tag{2.37}$$

$$\beta = -\sin\omega \cos(M' - \Omega) + \cos\omega \cos i \sin(M' - \Omega) \tag{2.38}$$

Under these assumptions, Eq. (2.34) becomes

$$R_{3\text{body}} = \frac{1}{2}\frac{\mu' n'^2 a'^3}{R'}\left(\frac{R}{R'}\right)^2 \left[3\left(\alpha \cos f + \beta \sin f\right)^2 - 1\right] \tag{2.39}$$

II.C. Local-Vertical–Local-Horizontal Frame

The local-vertical–local-horizontal (LVLH) frame, $\mathcal{H}$, of the reference satellite is defined in Figure II.4, with $\hat{\mathbf{h}}_1$ in the direction of its orbit radius, $\hat{\mathbf{h}}_3$ in the direction of its angular momentum, and $\hat{\mathbf{h}}_2$ completing the right-hand coordinate system. The rotation matrix from frame $\mathcal{I}$ to frame $\mathcal{H}$ is

$$\mathbf{C}_{hi}(t) = \begin{bmatrix} \dfrac{\mathbf{R}}{R} & \dfrac{\mathbf{h}\times\mathbf{R}}{|\mathbf{h}\times\mathbf{R}|} & \dfrac{\mathbf{h}}{h} \end{bmatrix}^T \tag{2.40}$$

where $\mathbf{h}$ is the reference satellite's angular momentum (per unit mass):

$$\mathbf{h} = \mathbf{R} \times \mathbf{V} \tag{2.41}$$

and $\mathbf{V}$ is the reference satellite's velocity. The position of the jth deputy in this frame is defined relative to the position of the chief, such that

$$\mathbf{r}_j = \mathbf{R}_j - \mathbf{R} \tag{2.42}$$

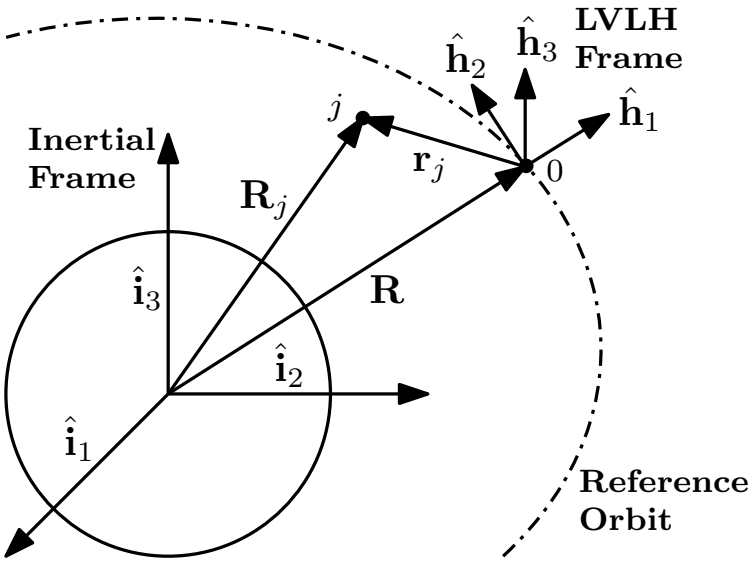

Figure II.4. Local-vertical–local-horizontal reference frame.

The LVLH frame is very useful for designing satellite formations because of its straightforward geometric interpretation and simple relative motion dynamics for circular reference orbits. However, for higher eccentricity reference orbits, the increasingly complex dynamics make it more difficult to use simple, intuitive rules for design.

In order to minimize linearization errors in the transformation between relative position and velocity and differential orbital elements, which will be the design variables for all applications in the present work, the LVLH curvilinear coordinate system, frame $\mathcal{C}$, is used. This system is illustrated in Figure II.5 and has the same orientation as the LVLH frame, but the x coordinate is the difference in the orbit radii and the y and z coordinates are the curvilinear distances along imaginary circular orbits in the reference orbital plane and perpendicular to the reference orbit, respectively. Expressing satellite relative position and velocity in curvilinear coordinates,

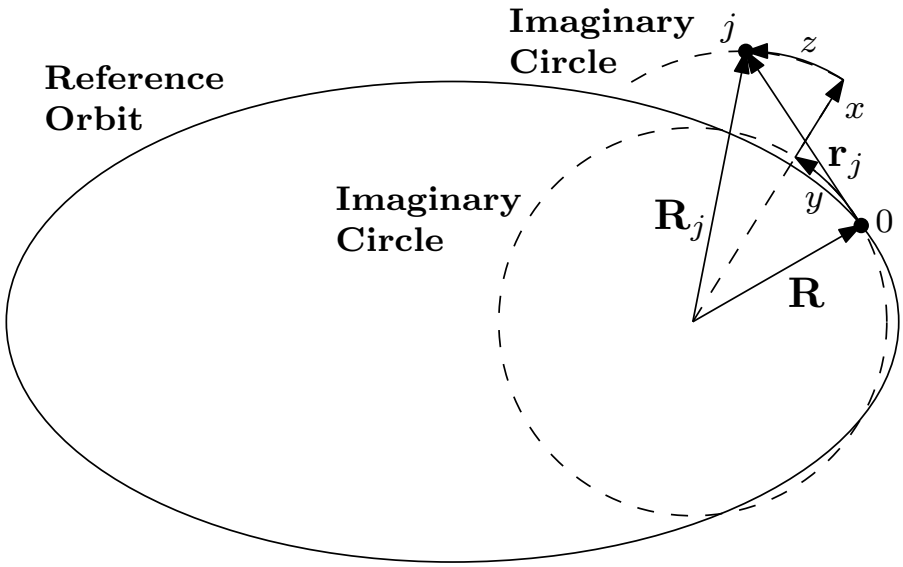

Figure II.5. LVLH curvilinear reference frame.

the state of the jth satellite is defined as

$$\mathbf{x}_j = \begin{bmatrix} {}^{c}\mathbf{r}_j \\ \\ {}^{c}\dot{\mathbf{r}}_j \end{bmatrix} \tag{2.43}$$

where ${}^{a}\mathbf{w}$ denotes the matrix expression of a vector $\mathbf{w}$ in a frame $\mathcal{A}$.

II.D. Relative Motion

LVLH coordinates are very useful for visualizing formations and defining or checking geometric relative motion requirements, but they are not ideal variables for long-term relative motion propagation because of the linear projection inherent in the definition of the frame as well as the nonlinearity of the dynamics. Instead, differential orbital elements will be used as design variables for each of the deputies.

Defining the non-singular mean orbital elements of the reference orbit as

$$\mathbf{e} = \begin{bmatrix} a & \theta & i & q_1 & q_2 & \Omega \end{bmatrix}^T \tag{2.44}$$

the initial differential non-singular mean orbital elements of the jth satellite are

$$\delta\mathbf{e}_j = \mathbf{e}_j(t_0) - \mathbf{e}(t_0) = \begin{bmatrix} \delta a_j & \delta\theta_j & \delta i_j & \delta q_{1j} & \delta q_{2j} & \delta\Omega_j \end{bmatrix}^T \tag{2.45}$$

where t_0 is the initial time. Note that although the argument (t_0) is omitted from $\delta\mathbf{e}_j$ these represent the initial differential mean orbital elements.

The curvilinear state $\mathbf{x}_j$ of the jth satellite can be computed at an arbitrary time t from its initial differential mean orbital elements $\delta\mathbf{e}_j$ using the Gim-Alfriend state transition matrix (G-A STM) [31],

$$\mathbf{x}_j(t) = \boldsymbol{\Sigma}(t)\,\mathbf{D}(t)\,\boldsymbol{\phi}_{\mathbf{e}}(t, t_0)\,\delta\mathbf{e}_j \tag{2.46}$$

where $\boldsymbol{\Sigma}(t)$ is the transformation matrix between the differential osculating elements and the curvilinear state,

$$\mathbf{D}(t) = \frac{\delta\mathbf{e}_{\text{osc}}(t)}{\delta\mathbf{e}_{\text{mean}}(t)} \tag{2.47}$$

is the transformation matrix between the differential mean and osculating elements, and $\boldsymbol{\phi}_{\mathbf{e}}(t, t_0)$ is the STM for the differential mean elements. The G-A STM is valid for arbitrary reference orbit eccentricity and includes first-order absolute and differential J_2 effects. Similarly, the initial differential elements can be obtained from the initial state,

$$\delta\mathbf{e}_j = [\mathbf{D}(t_0)]^{-1}[\boldsymbol{\Sigma}(t_0)]^{-1}\mathbf{x}_j(t_0) \tag{2.48}$$

The matrices $\boldsymbol{\Sigma}(t)$, $\mathbf{D}(t)$, and $\boldsymbol{\phi}_{\mathbf{e}}(t, t_0)$ can be found in Ref. 31.

CHAPTER III

FORMATION DESIGN ALGORITHMS*

Satellite formation design is defined in the present work as "The selection of initial relative parameters or states for a formation of satellites about a given reference orbit in order to accomplish a set of specific mission goals and requirements." These mission goals and requirements can include specific geometric constraints on the relative separation, orientation, or position between the satellites as well as more abstract quantities based on their relative states. For example, performance indices which evaluate the quality of scientific measurements obtainable for a given formation configuration are common. Mission requirements may be specified at all times or only for portions of the orbit and may also include provisions for collision avoidance, inter-satellite communication availability, etc.

In this chapter, several methods will be presented for long-duration satellite formation design (without corrective thrusting) in high-eccentricity reference orbits

---

*Part of this chapter is reprinted with permission from "Design of Satellite Formations in Orbits of High Eccentricity with Performance Constraints Specified over a Region of Interest" by Roscoe, C. W. T., Vadali, S. R., and Alfriend, K. T., 2011, *Advances in the Astronautical Sciences*, Vol. 139, pp. 145–162. Copyright 2011 by the American Astronautical Society.

*Part of this chapter is reprinted with permission from "Optimal Formation Design for Magnetospheric Multiscale Mission Using Differential Orbital Elements" by Roscoe, C. W. T., Vadali, S. R., Alfriend, K. T., and Desai, U. P., 2011, *Journal of Guidance, Control, and Dynamics*, Vol. 34, No. 4, pp. 1070–1080. Copyright 2011 by Christopher W. T. Roscoe, Srinivas R. Vadali, Kyle T. Alfriend, and Uri P. Desai.

*Part of this chapter is reprinted with permission from "Robust Formation Design for the Magnetospheric Multiscale Mission using a Stochastic Optimization Approach" by Roscoe, C. W. T., Vadali, S. R., and Alfriend, K. T., 2012, *Adventures on the Interface of Mechanics and Control*. Copyright 2012 by Tech Science Press.

for science return missions. The satisfaction of mission goals is quantified by a general performance index called the "quality factor" (QF), evaluated on a specific segment of the orbit called the "Region of Interest" (RoI) and related to the size and shape of the instantaneous formation, and additional requirements may be incorporated as performance constraints. Without loss of generality, the QF will be assumed to be scalar and positive, with higher values indicating better performance, and purely a function of the relative positions of the deputies. In general, the reference orbit will be assumed to be specified and the design variables will be the initial differential non-singular mean orbital elements of the deputies: the n $\delta\mathbf{e}_j$ variables defined in Chapter II. The only disturbance to the Keplerian motion treated in this chapter will be the J_2 perturbation, and relative state propagation will be performed using the Gim-Alfriend state transition matrix (G-A STM), also introduced in Chapter II.

III.A. Along-Track Drift Condition

In most formation flying applications, including the present work, the satellites are assumed to be close to one another compared to the size of the reference orbit at all times. For this to be true over many successive orbits, the satellites must be dynamically constrained or controlled through periodic thrusting maneuvers to ensure boundedness of the relative motion. In the absence of perturbations, the dynamic requirement is to select the orbital period of all of the satellites to be the same: this is accomplished by setting $\delta a_j = 0$ for all deputies.

In the presence of J_2 it is not possible to match the periods of all of the satellites using a single constraint for each. For formations, the differential J_2 perturbation

causes drift in the along-track, radial, and out-of-plane directions. This drift is caused by a difference in inclination, eccentricity, and semimajor axis. The only way to precisely guarantee long-term bounded motion (in terms of mean elements) is to set $\delta a_j = \delta e_j = \delta i_j = 0$ for all deputies, which does not leave enough free design variables left over to be useful for most applications.

The most common approach taken to obtain long-term formation stability in the presence of J_2 is to instead impose a condition on the semimajor axis difference to minimize the average along-track drift throughout an orbit between all of the satellites, since rate differences in this direction will cause the satellites to rapidly drift apart. The drift caused by the eccentricity difference is actually the result of the difference in the square of the eccentricity; thus, this effect is small for formations in near-circular orbits, and the inclination difference is the main cause of the drift. However, for formations in highly eccentric orbits, an eccentricity difference can cause just as much of an effect as an inclination difference. In addition, the radial drift resulting from differential perigee rotation has a more pronounced effect.

The along-track position of the jth satellite as a function of its differential orbital elements is [31]

$$\frac{y_j}{R} = \delta f_j + \delta\omega_j + \delta\Omega_j \cos i \tag{3.1}$$

For small $\delta\Omega_j$ and δi_j, the condition to negate the instantaneous along-track drift rate at some point in the orbit is

$$\delta\dot{f}_j + \delta\dot{\omega}_j + \delta\dot{\Omega}_j \cos i = 0 \tag{3.2}$$

Therefore, to minimize average along-track drift throughout an entire orbit, the

condition is [30]

$$\delta\dot{M}_j + \delta\dot{\omega}_j + \delta\dot{\Omega}_j \cos i = 0 \tag{3.3}$$

To first order in J_2, the change in the semimajor axis required to enforce this constraint is

$$\delta a_j = \frac{J_2 R_e^2 \left(3\eta + 4\right)}{2a\eta^4} \left[\left(3\cos^2 i - 1\right) \frac{e\delta e_j}{\eta^2} - \sin 2i \ \delta i_j \right] \tag{3.4}$$

This result is obtained by taking the first variation of the mean rates of Ω, ω, and M, found in Eqs. (2.17), (2.18), and (2.19), respectively.

III.A.1. Modified Along-Track Drift Condition

Although the along-track drift condition results in a single constraint for each deputy, even this δa_j constraint can be overly restrictive for formation design problems in which performance criteria are only evaluated during certain parts of the orbit. In the present work, since the RoI is only defined as a portion of the orbit, better results could be obtained by evaluating along-track drift only within the RoI. Neglecting J_2, the relationship between $\dot{f}$ and $\dot{M}$ is given by

$$\dot{f} = \frac{\dot{M}}{\eta^3}(1 + e\cos f)^2 \tag{3.5}$$

Taking the first variation of this equation while holding e and f as constants yields

$$\delta\dot{f}_j = \frac{\delta\dot{M}_j}{\eta^3}(1 + e\cos f)^2 \tag{3.6}$$

Substituting Eq. (3.6) into Eq. (3.2) and comparing with Eq. (3.3) suggests a modified along-track drift condition of the form

$$\delta\dot{M}_j + k_j \left(\delta\dot{\omega}_j + \delta\dot{\Omega}_j \cos i\right) = 0 \tag{3.7}$$

where k_j is a parameter defining the relative weighting of the mean motion to the differential argument of perigee and nodal precession rates. Proceeding by taking the first variations of Eqs. (2.17)–(2.19), as before, and substituting into Eq. (3.7) yields the modified δa_j condition

$$\delta a_j = \frac{J_2 R_e^2 \left(3\eta + 4k_j\right)}{2a\eta^4} \left[\left(3\cos^2 i - 1\right) \frac{e\delta e_j}{\eta^2} - \sin 2i \; \delta i_j \right] \tag{3.8}$$

Depending on the particular application, the k_j parameter may be defined analytically or chosen by other means. For example, substitution of Eq. (3.6) into Eq. (3.2), and a comparison of the result obtained with Eq. (3.7) provides an expression for the instantaneous value of k_j as

$$k_{j,\text{inst}} = \frac{\eta^3}{(1 + e\cos f)^2} \tag{3.9}$$

As another example, Eq. (3.6) can be averaged over a portion of the orbit before substitution into Eq. (3.2). If this averaging is performed over an entire orbit the result is precisely the traditional along-track drift condition of Eq. (3.3), hence that condition can be thought of as a special case of the modified condition in which $k_j = 1$. On the other hand, the effect of perturbations and the nonlinearity of both the dynamics and the relationship between the QF and the design variables may mean that values of k_j determined by numerical analysis will yield better results than approximate analytical values. In such cases, however, analytical values can still be used to support and validate the analysis.

For brevity in later sections, the leading coefficient on the right-hand side of Eq. (3.8) is defined as C_j:

$$C_j = \frac{J_2 R_e^2 \left(3\eta + 4k_j\right)}{2a\eta^4} \tag{3.10}$$

III.B. Tetrahedron Formation

One important type of satellite formation is the tetrahedron formation, useful for a variety of synthetic aperture-type mission applications including the NASA Magnetospheric Multiscale (MMS) mission, which will be used as an example application in Chapter IV. This type of formation generally requires four satellites to form a regular tetrahedron of a certain side length at a specific point or throughout a certain region of the reference orbit. Formations of more than four satellites with analogous geometric shapes are also possible.

Initial formation design is performed by defining, at some initial time t_0, a regular tetrahedron of side length L and associated reference frame, $\mathcal{T}$, as shown in Figure III.1. The chief satellite (0) is placed at the origin of this frame and the deputy satellites (1, 2, and 3) are placed at the remaining vertices of the tetrahedron. This frame is defined with $\hat{\mathbf{t}}_1$ in the direction of 1; $\hat{\mathbf{t}}_2$ in the plane of 1 and 2, oriented such that $\mathbf{r}_2 \cdot \hat{\mathbf{t}}_2 > 0$; and $\hat{\mathbf{t}}_3$ completing the right-hand coordinate system. Note that

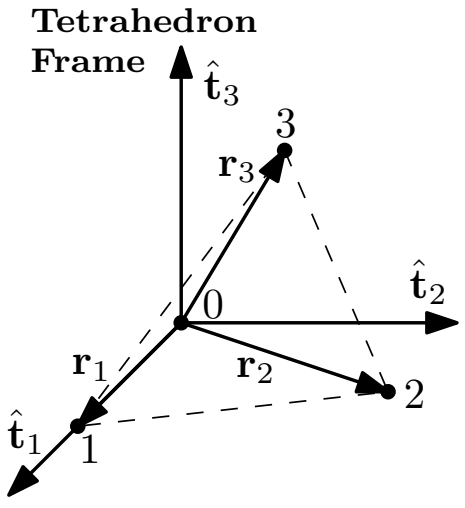

Figure III.1. Geometry of a regular tetrahedron.

the ordering of the deputies can always be chosen such that $\mathbf{r}_3 \cdot \hat{\mathbf{t}}_3 > 0$ as well. The positions of the deputies in frame $\mathcal{T}$ are therefore defined by simple geometry:

$$ {}^t\mathbf{r}_1 = \begin{bmatrix} L \\ 0 \\ 0 \end{bmatrix} \quad , \quad {}^t\mathbf{r}_2 = \begin{bmatrix} \frac{1}{2}L \\ \frac{\sqrt{3}}{2}L \\ 0 \end{bmatrix} \quad , \quad {}^t\mathbf{r}_3 = \begin{bmatrix} \frac{1}{2}L \\ \frac{1}{2\sqrt{3}}L \\ \sqrt{\frac{2}{3}}L \end{bmatrix} \tag{3.11} $$

Frame $\mathcal{T}$ is related to the local-vertical–local-horizontal (LVLH) frame, $\mathcal{H}$, of the reference satellite by a 3-2-1 (ϕ-ψ-γ) Euler rotation sequence,

$$ \mathbf{C}_{th} = \mathbf{C}_1(\gamma)\mathbf{C}_2(\psi)\mathbf{C}_3(\phi) \tag{3.12} $$

which allows for the definition of a tetrahedron of any possible orientation in the LVLH frame. The positions of the deputy satellites in frame $\mathcal{H}$ are obtained from

$$ {}^h\mathbf{r}_j = \mathbf{C}_{th}^T \, {}^t\mathbf{r}_j \quad , \quad j \; = \; 1, 2, 3 \tag{3.13} $$

Since the G-A STM uses LVLH curvilinear coordinates, the positions of the satellites must then be converted from frame $\mathcal{H}$ to frame $\mathcal{C}$. The relationship between these two systems is shown in Figures III.2(a) and (b) (with primed variables indicating Cartesian coordinates), assuming that the angles ϕ' and ψ' are small, which they will be if the satellites are sufficiently close together compared to the size of the reference orbit. The velocities of these satellites relative to the reference satellite, in frame $\mathcal{C}$, are initially chosen to be zero.

The initial differential elements of the satellites can then be determined from Eq. (2.48). Directly applying Eq. (3.8) (or Eq. (3.4)) to each of these initial sets of elements (and replacing δa_j) would satisfy the modified along-track drift condition, but would also unacceptably alter the initial tetrahedron configuration. Therefore,

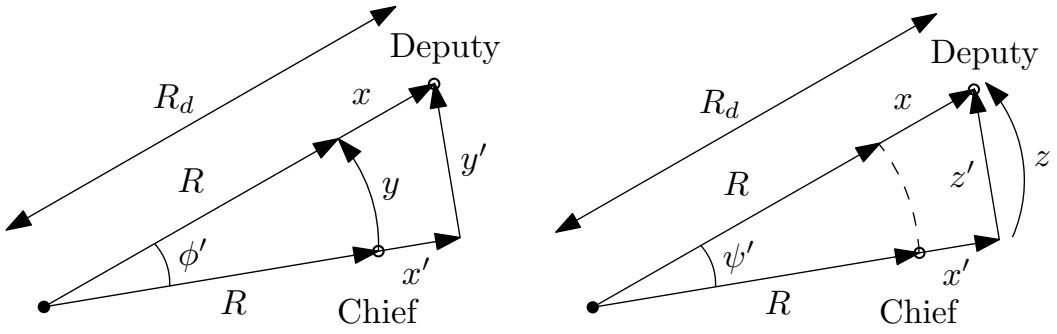

(a) $\hat{\mathbf{h}}_1 - \hat{\mathbf{h}}_2$ plane. **(b) $\hat{\mathbf{h}}_1 - \hat{\mathbf{h}}_3$ plane.**

Figure III.2. Relationship between LVLH Cartesian and curvilinear coordinates.

to compensate for the change in δa_j required to obtain long-term stability, the other elements must be modified to maintain the desired relative position.

The curvilinear position components of the jth satellite can be written [31],

$$\frac{x_j}{R} = \frac{1}{a}\delta a_j + \frac{V_r}{V_t}\delta\theta_j - \frac{1}{p}\left(2aq_1 + R\cos\theta\right)\delta q_{1j} - \frac{1}{p}\left(2aq_2 + R\sin\theta\right)\delta q_{2j} \tag{3.14}$$

$$\frac{y_j}{R} = \delta\theta_j + \cos i\ \delta\Omega_j \tag{3.15}$$

$$\frac{z_j}{R} = \sin\theta\ \delta i_j - \cos\theta\sin i\ \delta\Omega_j \tag{3.16}$$

where

$$V_r = \sqrt{\frac{\mu}{p}}\left(q_1\sin\theta - q_2\cos\theta\right) \tag{3.17}$$

$$V_t = \sqrt{\frac{\mu}{p}}\left(1 + q_1\cos\theta + q_2\sin\theta\right) \tag{3.18}$$

Since only the first component depends on δa_j and δe_j (through δq_{1j} and δq_{2j}), which are related by Eq. (3.8), then it will suffice to only modify δe_j in order to maintain the desired relative position [84]. Manipulating δq_{1j} and δq_{2j} and defining the quantities

A and B,

$$\begin{aligned}\delta q_{1j} &= q_1\left(\cos\delta\omega_j - 1\right) - q_2\sin\delta\omega_j + \cos\left(\omega + \delta\omega_j\right)\delta e_j \\ &= A + \cos\left(\omega + \delta\omega_j\right)\delta e_j \end{aligned} \tag{3.19}$$

$$\begin{aligned}\delta q_{2j} &= q_2\left(\cos\delta\omega_j - 1\right) + q_1\sin\delta\omega_j + \sin\left(\omega + \delta\omega_j\right)\delta e_j \\ &= B + \sin\left(\omega + \delta\omega_j\right)\delta e_j \end{aligned} \tag{3.20}$$

the required condition for δe_j becomes

$$\begin{aligned}\delta e_j = \Bigg[&\frac{x_j}{R} + \frac{C_j}{a}\sin 2i\ \delta i_j - \frac{V_r}{V_t}\delta\theta_j + \frac{A}{p}\left(2aq_1 + R\cos\theta\right) \\ &+\frac{B}{p}\left(2aq_2 + R\sin\theta\right)\Bigg] \\ \Bigg/\ \Bigg[&\frac{C_j}{a\eta^2}\left(3\cos^2 i - 1\right)e - \frac{1}{p}\left(2aq_1 + R\cos\theta\right)\cos\left(\omega + \delta\omega_j\right) \\ &-\frac{1}{p}\left(2aq_2 + R\sin\theta\right)\sin\left(\omega + \delta\omega_j\right)\Bigg]\end{aligned} \tag{3.21}$$

This method results in a formation which forms a regular tetrahedron at one point in the reference orbit. Formations produced by this method are by no means optimal, but they can serve as useful initial guesses when applying the optimal methods of the following sections to tetrahedron formation applications.

III.C. Nominal Formation Design Algorithms

Hughes [81] in 2008 presented a general method for designing satellite formations to satisfy science return criteria by optimizing a performance index over a single orbit using Cartesian position and velocity as the design variables. The long-term formation design problem was addressed by Hughes [85] later that same year using a multi-revolution optimization approach, including the effect of perturbations. Both

of these methods use numerical techniques for relative state propagation. In the following two sections, two fast and efficient formation design algorithms (FDAs) will be defined using differential mean orbital elements as design variables instead.

Since the formation design goal is to obtain the best possible QF performance throughout the RoI, the following optimization problems will use as the basis for their cost functions the time average of the QF in the RoI,

$$\bar{Q}_{\text{RoI}} = \frac{1}{t_2 - t_1} \int_{t_1}^{t_2} Q \; dt \tag{3.22}$$

where Q is the instantaneous QF and t_1 and t_2 are the times at which the formation enters and exits the RoI, respectively. In order to use $\bar{Q}_{\text{RoI}}$ in a numerical optimization framework, this integration must be performed discretely. However, it is numerically advantageous to discretize the integration with respect to true anomaly rather than time; therefore, Eq. (3.22) must be rewritten in terms of f. Combining Eqs. (2.10), (2.3), (2.6), and (2.12) yields the differential relation

$$dt = \frac{\eta^3 \; df}{n \left(1 + e \cos f\right)^2} \tag{3.23}$$

Substituting Eq. (3.23) into Eq. (3.22) and using Kepler's equation, Eq. (2.13), then leads to

$$\bar{Q}_{\text{RoI}} = \frac{\eta^3}{M_2 - M_1} \int_{f_1}^{f_2} \frac{Q \; df}{\left(1 + e \cos f\right)^2} \tag{3.24}$$

Discretizing Eq. (3.24) at N_f equal spacings of true anomaly,

$$\bar{Q}_{\text{RoI}} \approx \frac{\eta^3}{N} \frac{f_2 - f_1}{M_2 - M_1} \sum_{m=1}^{N_f} \frac{Q_m}{\left(1 + e \cos f_m\right)^2} \tag{3.25}$$

In order to evaluate Eq. (3.25), the position of each satellite in frame $\mathcal{H}$ must be known at each discretization point. As mentioned in Chapter II, the curvilinear

state $\mathbf{x}_j$ of the jth satellite can be computed at an arbitrary time t from its initial differential mean orbital elements $\delta\mathbf{e}_j$ using the G-A STM, Eq. (2.46). The Cartesian position ${}^h\mathbf{r}_j$ can then be computed as a function of ${}^c\mathbf{r}_j$ and R, as shown in Figure III.2.

The G-A STM also provides a convenient way to compute the gradient of $\bar{Q}_{\text{RoI}}$ with respect to the design variables $\delta\mathbf{e}_j$. Proceeding in a similar fashion to Hughes [85], applying the chain rule to Eq. (3.25) yields

$$\begin{aligned}\frac{\partial \bar{Q}_{\text{RoI}}}{\partial \delta \mathbf{e}_j} &= \left[\begin{array}{cccccc} \dfrac{\partial \bar{Q}_{\text{RoI}}}{\partial \delta a_j} & \dfrac{\partial \bar{Q}_{\text{RoI}}}{\partial \delta \theta_j} & \dfrac{\partial \bar{Q}_{\text{RoI}}}{\partial \delta i_j} & \dfrac{\partial \bar{Q}_{\text{RoI}}}{\partial \delta q_{1j}} & \dfrac{\partial \bar{Q}_{\text{RoI}}}{\partial \delta q_{2j}} & \dfrac{\partial \bar{Q}_{\text{RoI}}}{\partial \delta \Omega_j} \end{array} \right] \\ &= \frac{\eta^3}{N} \frac{f_2 - f_1}{M_2 - M_1} \sum_{m=1}^{N_f} \frac{1}{(1 + e\cos f_m)^2} \frac{\partial Q_m}{\partial\, {}^h\mathbf{r}_j} \frac{\partial\, {}^h\mathbf{r}_j}{\partial \delta \mathbf{e}_j} \end{aligned} \tag{3.26}$$

making use of the fact that the position of the jth satellite depends only on its own initial differential elements. In the present work, the gradient of a scalar function with respect to an n-dimensional state is a $1 \times n$ matrix, and the gradient of an m-dimensional function with respect to an n-dimensional state is an $m \times n$ matrix. For the purposes of calculating the gradients, the linearization of the LVLH frame is acceptable—thus, it is assumed that ${}^h\mathbf{r}_j \approx {}^c\mathbf{r}_j$ in this case. The gradient of the position of the ith satellite with respect to the initial differential mean orbital elements of the jth satellite is obtained from Eq. (2.46):

$$\frac{\partial\, {}^h\mathbf{r}_i}{\partial \delta \mathbf{e}_j} = \left[\begin{array}{cc} \mathbf{1}_3 & \mathbf{0}_{3\times 3} \end{array} \right] \mathbf{\Sigma}(t)\, \mathbf{D}(t)\, \boldsymbol{\phi}_{\mathbf{e}}(t, t_0)\, \delta_{ij} \tag{3.27}$$

where $\mathbf{1}_n$ is the $n \times n$ identity matrix, $\mathbf{0}_{n\times m}$ is the $n \times m$ zero matrix, and δ_{ij} is the Kronecker delta.

III.C.1. Single-Orbit Constrained Optimization

The objective of the single-orbit constrained (SOC) optimization to maximize $\bar{Q}_{\text{RoI}}$ for one orbit while imposing the modified along-track drift condition of Eq. (3.7) to yield long-term formation stability. The SOC optimization problem is defined as

$$\begin{aligned} \text{minimize} \quad & -\bar{Q}_{\text{RoI}} \\ \text{with respect to} \quad & \delta\mathbf{e}_j \quad , \quad j = 1, 2, \ldots, n \\ \text{subject to} \quad & \delta a_j = C_j \left[\left(3\cos^2 i - 1 \right) \frac{e\delta e_j}{\eta^2} - \sin 2i \; \delta i_j \right] \end{aligned} \tag{3.28}$$

Using the G-A STM for state propagation and analytical gradient evaluation, this optimization is extremely fast and efficient since it is only performed over one orbit and the δa_j condition essentially removes one degree of freedom for each deputy.

III.C.2. Multi-Orbit Unconstrained Optimization

To maximize QF performance and achieve long-term formation stability without using the δa_j constraint, the multi-orbit unconstrained (MOU) optimization problem is defined as

$$\begin{aligned} \text{minimize} \quad & -\sum_{k=1}^{N_{\text{orb}}} \bar{Q}_{\text{RoI},k} \\ \text{with respect to} \quad & \delta\mathbf{e}_j \quad , \quad j = 1, 2, \ldots, n \end{aligned} \tag{3.29}$$

where $\bar{Q}_{\text{RoI},k}$ is the average QF in the RoI in the kth orbit and N_{orb} is the total number of orbits to be considered. Since this optimization allows more freedom in the design variables it should generally produce slightly better long-term performance results, but at a much greater cost in terms of computation requirements.

III.D. Robust Formation Design Algorithm

All satellite missions involve some uncertainty in their dynamic parameters and formulation, and formation flying missions are no exception. Imperfect maneuvering systems cannot deliver exactly the desired thrust at precisely the correct time, and imperfect attitude control systems cannot point the thrust vector in exactly the desired direction. Limitations of space-based navigation systems mean that position and velocity (and differential position and velocity) are never known completely accurately. The dynamic model itself is usually simplified in the interests of reducing computational overhead and easing implementation. The combination of these factors can introduce significant errors into the design process and drastically alter the predicted performance of a mission.

Some of these errors can be mitigated by using more complex dynamic or physical models, but a certain amount of uncertainty will always remain. In formation flying applications, the most important factor is the initialization of a desired formation. This is because, no matter how much care is taken to design a high-quality, stable formation, these errors mean that it can never be achieved exactly. This is a significant problem, since long-term formation stability is typically very sensitive to initialization errors. Therefore, the goal of this section is to outline a method in which some performance in the nominal, error-free, case can be sacrificed in order to gain robustness with respect to initialization errors.

III.D.1. Stochastic Optimization

A stochastic optimization problem is an optimization problem in which the performance index is a function of some random variables in addition to the deterministic design variables. Numerous methods exist for addressing such problems, all of which involve converting the stochastic system into a reduced deterministic substitute system [86]. None of these solutions will be unique, however, since some design choice must be made in terms of how to eliminate the random variables from the problem.

The overall optimization goal is to minimize a performance index

$$\begin{aligned} & f(\mathbf{x}, \mathbf{a}) \in \mathbb{R} \\ & \mathbf{x} \in \mathbb{R}^n \quad , \quad \mathbf{a} \in \mathbb{R}^l \end{aligned} \tag{3.30}$$

which is a function of the design variable $\mathbf{x}$ and a random variable $\mathbf{a}$. $\mathbf{a}$ has a mean of $\boldsymbol{\mu}_{\mathbf{a}}$ and covariance of $\boldsymbol{\Sigma}_{\mathbf{a}}$, but no assumption is made yet regarding the form of its probability distribution. Since $\mathbf{a}$ represents an error parameter, it will typically be zero-mean, but, for generality, no such assumption will be made at this time. The deterministic optimization approach is to let

$$\mathbf{a} = \boldsymbol{\mu}_{\mathbf{a}} \tag{3.31}$$

and minimize

$$f_{\text{det}}(\mathbf{x}) = f(\mathbf{x}, \boldsymbol{\mu}_{\mathbf{a}}) \tag{3.32}$$

Note that, with the application of Eq. (3.31), Eq. (3.32) depends only on $\mathbf{x}$ and can be minimized using standard techniques.

This approach is simple to use and is equivalent to ignoring error sources and optimizing solely based on nominal performance, which is precisely the method used

in Section III.C. It is practical when errors are small or have little impact on the performance index, mission timelines are short and error effects do not have long enough to accumulate, or when periodic correction maneuvers are allowed (and are inexpensive).

The expected value of an arbitrary function $\mathbf{g}(\mathbf{a})$ of a random variable $\mathbf{a}$ is defined as

$$E(\mathbf{g}) = \int_{\Omega} \mathbf{g}(\mathbf{a}) P(\mathbf{a}) \ d\mathbf{a} \tag{3.33}$$

where $P(\mathbf{a})$ is the probability density function (PDF) of $\mathbf{a}$ and Ω is its domain. Given the performance index defined in Eq. (3.30), the stochastic optimization approach is to minimize the expected value of $f(\mathbf{x}, \mathbf{a})$

$$f_{\text{rob}}(\mathbf{x}) = E(f) \tag{3.34}$$

This approach requires some knowledge of the probability distribution of $\mathbf{a}$ but takes into account the error parameter distribution and its effect on the performance index. Note that, although Eq. (3.33) explicitly requires the PDF of $\mathbf{a}$, this method will only require knowledge of some of its moments if the error parameter appears as a polynomial in the performance index.

III.D.2. Approximate Stochastic Optimization

For complex performance indices, it may not be possible or practical to solve the expectation integral, Eq. (3.33). In this section, an approximate method is described for evaluating this equation, which can be used instead of the integral form in such cases. This method has the primary advantage that it can be computed by sampling the error distribution at discrete points and evaluating the performance index a finite

number of times to approximate the expectation integral.

To approximate Eq. (3.33), the integral is expanded as a Riemann sum in each of the l components of $\mathbf{a}$. To accomplish this in a finite series, the domain of $\mathbf{a}$ (that is, Ω) must be finite or must be truncated at some reasonable, finite boundary. For example, if $\mathbf{a}$ is normally distributed (the domain of which is all of $\mathbb{R}^l$), truncating the domain of each element at its $\pm 3\sigma$ points will still yield a reasonably accurate solution. Each component a_j of $\mathbf{a}$ is then discretized into N_j equal intervals of length Δa_j, such that the entire (truncated) domain is split into $N_1 \times N_2 \times \cdots \times N_l$ elements, where

$$\Delta V = \Delta a_1 \Delta a_2 \cdots \Delta a_l \tag{3.35}$$

is the hypervolume of each one. The integral can then be approximated as

$$E\left(f\right) \approx \sum_{a_1}^{N_1} \cdots \sum_{a_l}^{N_l} f\left(\mathbf{x}, \mathbf{a}\right) P\left(\mathbf{a}\right) \Delta V \tag{3.36}$$

in which the performance index and the PDF are sampled at one point in each of the discrete elements of the domain. This is only one of many integral approximation methods, and, depending on the desired degree of accuracy, other techniques could also be employed. For the present formation design algorithms, the actual accuracy of the approximation is not as important as its ability to capture trends in the behavior of the performance index as the design variable is varied. Furthermore, since ΔV is invariant with respect to the optimization being performed, it can be omitted in the final formulation of the robust cost function.

The performance index can be further refined to allow for more control over the tradeoff between nominal performance and robustness if some assumptions are made regarding the form of the distribution of $\mathbf{a}$. Assuming that each component of $\mathbf{a}$ is

independent and normally distributed with mean of zero and variance σ^2, then the PDF of $\mathbf{a}$ can be written

$$P(\mathbf{a}) = \frac{1}{\sqrt{(2\pi)^l \sigma^2}} \exp\left[-\frac{\mathbf{a}^T\mathbf{a}}{2\sigma^2}\right] \tag{3.37}$$

Defining a weighting parameter w and letting each $N_j = N$ then yields the robust performance index

$$f^*_{\text{rob}}(\mathbf{x}) = \sum_{i=1}^{N^l} f(\mathbf{x}, \mathbf{a}_i) \exp\left[-\frac{\mathbf{a}_i^T\mathbf{a}_i}{2\sigma^2 w}\right] \tag{3.38}$$

where the constant coefficients, which are independent of the optimization, have been omitted. w controls the design tradeoff between nominal performance and robustness, such that: $0 < w < 1$ places more emphasis on nominal performance; $1 < w < \infty$ places more emphasis on robustness; and $w = 1$ corresponds to maximizing the expected value of f in the case in which $\mathbf{a}$ is distributed normally, as in Eq. (3.37). Note that if $w \neq 1$, minimizing Eq. (3.38) does not actually minimize the approximate expected value of f since the PDF of $\mathbf{a}$ has been modified by the introduction of w. Instead, this is a new performance index which is related to the previous one but allows more control over the outcome of the design process.

III.D.3. Robust Formation Optimization

For many formation flying missions, the main sources of initialization errors include inaccurate maneuver magnitude, direction, and timing as well as errors in the navigation system. In the following formulation, initialization errors are considered based only on their effects on the deputies' initial differential semimajor axes, since the effect of δa errors on formation stability is $\mathcal{O}(1)$, whereas the effect of errors in any other element is $\mathcal{O}(J_2)$ or smaller. Furthermore, δa errors will be assumed to be

zero-mean normally distributed and independent of one another.

The expected value of $\bar{Q}_{\text{RoI}}$, given a PDF $P\left(\delta a_{e1}, \ldots, \delta a_{en}\right)$ of the deputies' δa errors, can be written

$$E\left(\bar{Q}_{\text{RoI}}\right) = \int_{-\infty}^{\infty} \cdots \int_{-\infty}^{\infty} \bar{Q}_{\text{RoI}} P\left(\delta \mathbf{a}_e\right) \; d\delta \mathbf{a}_e \tag{3.39}$$

where

$$\delta \mathbf{a}_e = \begin{bmatrix} \delta a_{e1} & \cdots & \delta a_{en} \end{bmatrix}^T \tag{3.40}$$

Since the components of $\delta \mathbf{a}_e$ are independently normally distributed and zero-mean, their PDF can be written in the form of Eq. (3.37):

$$P\left(\delta \mathbf{a}_e\right) = \frac{1}{\sqrt{\left(2\pi\right)^3 \sigma^2}} \exp\left[-\frac{\delta \mathbf{a}_e^T \delta \mathbf{a}_e}{2\sigma^2}\right] \tag{3.41}$$

Therefore, sampling each component at N points and introducing the w parameter as before, the robust performance index is

$$J_r = -\sum_{i=1}^{N^n} \bar{Q}_{\text{RoI},i} \exp\left[-\frac{\delta \mathbf{a}_{e,i}^T \delta \mathbf{a}_{e,i}}{2\sigma^2 w}\right] \tag{3.42}$$

where the $\bar{Q}_{\text{RoI},i}$ are the value of $\bar{Q}_{\text{RoI}}$ based on each sampling of the $\delta \mathbf{a}_e$ distribution.

The robust optimization problem is defined as

$$\begin{aligned} \text{minimize} \quad & \sum_{k=1}^{N_{\text{orb}}} J_{r,k} \\ \text{with respect to} \quad & \delta \mathbf{e}_{\text{nom},j} \quad , \quad j = 1, 2, \ldots, n \\ \text{subject to} \quad & \delta a_{\text{nom},j} = C_j \left[\left(3\cos^2 i - 1\right) \frac{e \delta e_j}{\eta^2} - \sin 2i \; \delta i_j\right] \end{aligned} \tag{3.43}$$

where $\delta a_{\text{nom},j}$ is the nominal or "target" δa_j, given by the modified along-track drift condition defined in Eq. (3.7). Similarly, $\delta \mathbf{e}_{\text{nom},j}$ are the nominal differential orbital elements; however, no errors are being applied to any element except for δa_j. The

optimization is performed over multiple orbits since long-term formation stability is of paramount importance.

Since $\delta a_{\text{nom},j}$ is explicitly specified by the along-track drift condition, the design variables are essentially the remaining $5n$ differential elements of the deputies. Denoting the 5 non-δa elements of the jth deputy by $\delta\mathbf{e}_{r,j}$, the gradient of J_r with respect to $\delta\mathbf{e}_{r,j}$ is then

$$\frac{\partial J_r}{\partial \delta \mathbf{e}_{r,j}} = -\sum_{i=1}^{N^n} \frac{\partial \bar{Q}_{\text{RoI},i}}{\partial \delta \mathbf{e}_{r,j}} \exp\left[-\frac{\delta \mathbf{a}_{e,i}^T \delta \mathbf{a}_{e,i}}{2\sigma^2 w}\right] \tag{3.44}$$

since $\delta\mathbf{a}_{e,i}$ is a random variable (not a design variable). Note that the gradient of a scalar function with respect to the 5 non-δa elements of one deputy can be computed from the gradient with respect to all 6 elements using the expression

$$\frac{\partial(\cdot)}{\partial \delta \mathbf{e}_{r,j}} = \frac{\partial(\cdot)}{\partial \delta \mathbf{e}_j} \begin{bmatrix} \mathbf{0}_{1\times 5} \\ \\ \mathbf{1}_5 \end{bmatrix} \tag{3.45}$$

III.E. Single-Variable Example

In this section, the application and effects of the deterministic and stochastic optimization strategies are illustrated using a simple example performance index. The single-variable example function is defined as

$$f(x,a) = \frac{ka^2}{x} + \frac{(x-c)^2}{\sigma^2} \tag{3.46}$$

where $x > 0$ is the design variable, a is a zero-mean random variable, and k, c, and σ are positive constants. This function is selected because of the specific way in which the design variable x affects the gradient of f with respect to the error parameter a. As shown in Figure III.3, when the value of x is lower (denoted by x_1,

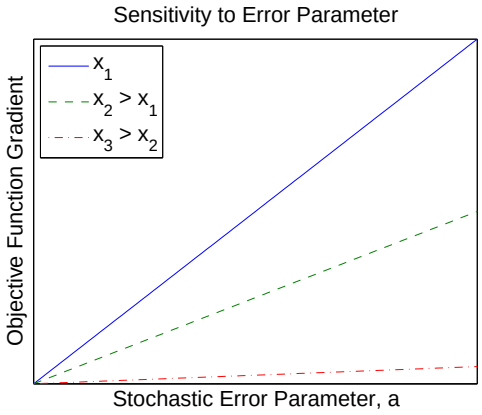

Figure III.3. Effect of the design variable on the gradient of the performance index.

closer to the deterministic minimum), the slope of $\frac{\partial f}{\partial a}$ becomes steeper; as $x \to \infty$, a no longer affects f at all. In many formation optimization problems, solutions near deterministic minima are similarly very sensitive to initialization errors but become less sensitive farther away.

Letting $a = \mu_a$ and minimizing $f_{\text{det}}(x) = f(x, \mu_a)$ with respect to x yields the first-order optimality condition

$$f'_{\text{det}}(x) = 0 = -\frac{k\mu_a^2}{x^2} + \frac{2(x-c)}{\sigma^2} \quad , \quad \mu_a = 0 \tag{3.47}$$

$$\therefore \quad x^*_{\text{det}} = c \tag{3.48}$$

which can be confirmed to be a minimum by checking the second-order optimality condition

$$f''_{\text{det}}(x^*_{\text{det}}) = \frac{2k\mu_a^2}{x^{*3}_{\text{det}}} + \frac{2}{\sigma^2} > 0 \tag{3.49}$$

Therefore, $f_{\text{det}}(x^*_{\text{det}})$ is the minimum value of f when a is considered to be a deterministic parameter. In fact, this is the lowest possible value of f for any a, when $x > 0$.

The expected value of the performance index, $E(f)$, assuming a PDF $P(a)$ for a is

$$\begin{aligned} E(f) &= \int_{-\infty}^{\infty} f(x,a)\, P(a)\ da \\ &= \frac{k}{x} \int_{-\infty}^{\infty} a^2 P(a)\ da + \frac{(x-c)^2}{\sigma^2} \int_{-\infty}^{\infty} P(a)\ da \\ &= \frac{k\sigma_a^2}{x} + \frac{(x-c)^2}{\sigma^2} \end{aligned} \tag{3.50}$$

according to the definition of the variance (second moment)

$$\sigma_a^2 = \int_{-\infty}^{\infty} (a-\mu_a)^2 P(a)\ da \tag{3.51}$$

(since $\mu_a = 0$) and the fundamental property of the PDF (zeroth moment)

$$\int_{-\infty}^{\infty} P(a)\ da = 1 \tag{3.52}$$

Minimizing $f_{\text{rob}}(x) = E(f)$ with respect to x yields the first-order optimality condition

$$f'_{\text{rob}}(x) = 0 = -\frac{k\sigma_a^2}{x^2} + \frac{2(x-c)}{\sigma^2} \tag{3.53}$$

$$\therefore \quad 0 = 2x_{\text{rob}}^{*3} - 2cx_{\text{rob}}^{*2} - k\sigma^2\sigma_a^2 \tag{3.54}$$

Note that the robust minimum x_{rob}^* depends on the variance of a. Given a general cubic equation of the form

$$0 = ax^3 + bx^2 + cx + d \tag{3.55}$$

the nature of the roots can be determined by examining the cubic discriminant [87]

$$\Delta = 18abcd - 4b^3d + b^2c^2 - 4ac^3 - 27a^2d^2 \tag{3.56}$$

If $\Delta > 0$, the equation has three distinct, real roots; if $\Delta = 0$, the equation has three real roots with at least one multiple root; and if $\Delta < 0$, the equation has one real root and one complex conjugate pair of roots. The discriminant of Eq. (3.54) is

$$\Delta = -32c^3k\sigma^2\sigma_a^2 - 108k^2\sigma^4\sigma_a^4 < 0 \tag{3.57}$$

which is less than zero since c and k are positive constants. Therefore, the robust minimum x^*_{rob} will be the real solution of Eq. (3.54). The second-order optimality condition is

$$f''_{\text{rob}}\left(x^*_{\text{rob}}\right) = 2\left(3x^*_{\text{rob}} - 2c\right)x^*_{\text{rob}} \tag{3.58}$$

which is positive (that is, $f_{\text{rob}}\left(x^*_{\text{rob}}\right)$ is a minimum) when $x^*_{\text{rob}} > \frac{2c}{3}$.

The performance index is shown in Figure III.4 for a range of a values, given the sample parameters listed in Table III.1. Clearly, the performance index is much more sensitive to errors in the deterministic optimization case than in the stochastic optimization one. The values of the design variable, the performance index (at $a = 0$), and the expected value of the performance index at the deterministic and

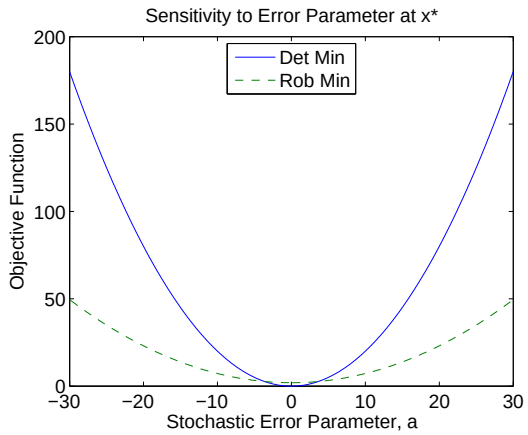

Figure III.4. Effect of the error parameter on the optimal performance index.

Table III.1. Sample cost function parameters.

Parameter	Value
k	1
c	5
σ	10
σ_a	10

robust minima are listed in Table III.2. As expected, the nominal value of the performance index at the robust minimum is slightly higher than the nominal value at the deterministic minimum, but the expected value in the presence of uncertainties is much lower at the robust minimum.

To illustrate the differences between these optimization strategies in a more practical setting, a Monte Carlo analysis is performed by computing the value of the performance index for a set of 5000 sample values of a, pseudo-randomly generated in MATLAB using a zero-mean normal distribution; that is, assuming $a \sim N(0, \sigma_a^2)$. The resulting distributions of the performance index are shown in Figures III.5(a) and (b) for the deterministic and robust optimizations, respectively. The sample mean and standard deviation of these distributions are listed in Table III.3: the mean values are identical to the theoretical expected values of f listed in Table III.2, and the standard deviation of the robust distribution is much lower than that of the deterministic distribution, as expected.

The results of applying the approximate stochastic optimization technique are

Table III.2. Optimal performance index values.

Optimization	x^*	$f(x^*, 0)$	$E(f)$
Deterministic	5	0	20
Robust	18.9	1.9	7.2

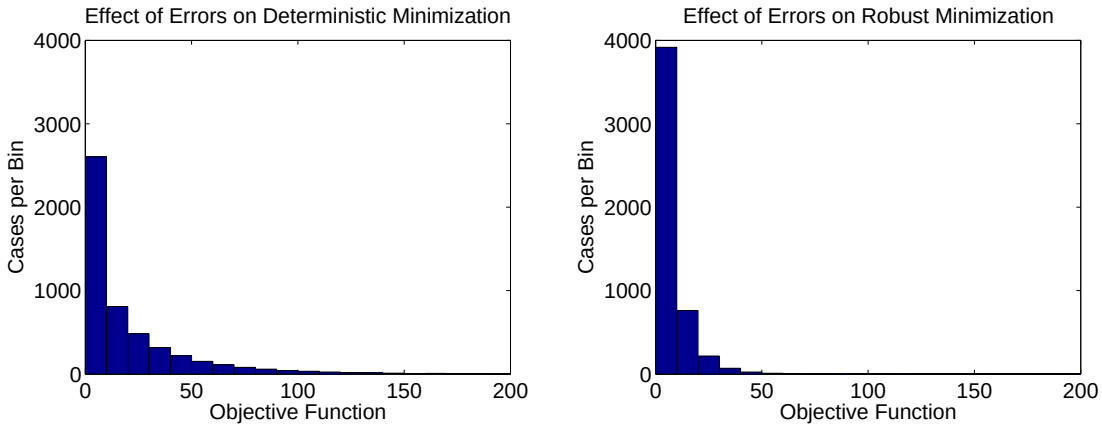

(a) Deterministic optimization. **(b) Robust optimization.**

Figure III.5. Performance index distributions for normally distributed a.

shown in Figures III.6(a) and (b). These distributions were obtained by sampling the a distribution at 3 points, -3σ, 0, and 3σ, with $w = 1$ and $w = 9$, respectively, and running the same 5000 case Monte Carlo simulation with normally distributed a. As expected, the $w = 9$ case has less spread in the data at the cost of some performance in the nominal case. This can be further illustrated by examining the distributions' mean and standard deviation characteristics, listed in Table III.4: the $w = 1$ case has a slightly lower mean but a significantly higher standard deviation. Comparing the values of the design variable, nominal performance index, and expected value to the analytical values (for $w = 1$) listed in Table III.2, the loss of accuracy in performing the approximation with so few sample points can be readily seen. However, compared

Table III.3. Monte Carlo performance index distribution characteristics.

Optimization	μ_f	σ_f
Deterministic	20.0	28.3
Robust	7.2	7.5

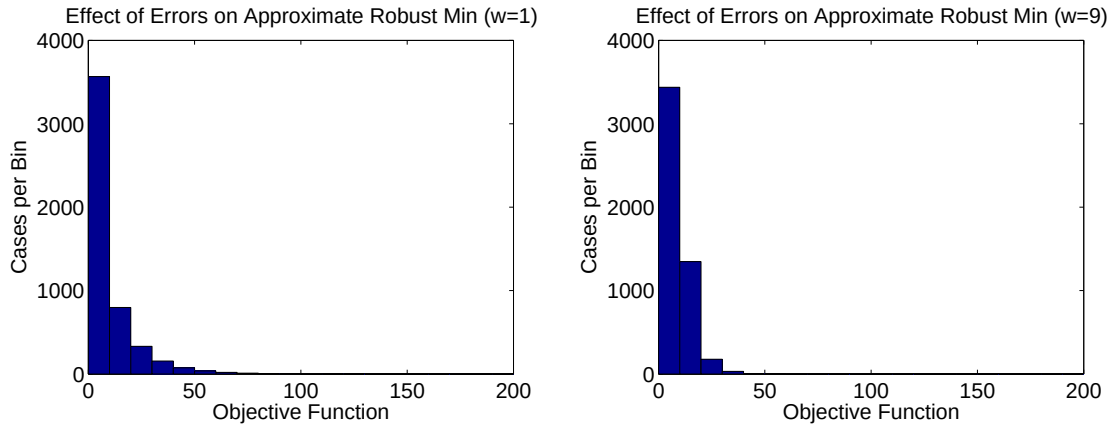

(a) $w = 1$. **(b)** $w = 9$.

Figure III.6. Performance index distributions for approximate robust optimization.

to the results of the nominal optimization case, these values are still quite reasonable; therefore, such a coarse discretization may be acceptable in certain cases if the main goal is to only improve the results over the nominal case without drastically increasing computational cost or problem complexity. This table also lists the characteristics for the corresponding cases in which the a distribution is sampled at 7 points, -3σ, -2σ, $-\sigma$, 0, σ, 2σ, and 3σ. These results are indistinguishable from those obtained using the analytical expectation integral solution to the precision shown here.

Table III.4. Approximate robust optimization results.

Discretization	w	x^*	$f(x^*, 0)$	$E(f)$	μ_f	σ_f
0, $\pm 3\sigma$	1	11.9	0.5	8.9	8.9	11.9
	9	30.9	6.7	9.9	9.9	4.6
0, $\pm\sigma$, $\pm 2\sigma$, $\pm 3\sigma$	1	18.9	1.9	7.2	7.2	7.5
	9	27.4	5.0	8.7	8.7	5.2

CHAPTER IV

MMS FORMATION DESIGN*

The objective of the NASA Magnetospheric Multiscale (MMS) mission is to study magnetic reconnection, charged particle acceleration, and turbulence in key boundary regions of the Earth's magnetosphere [11]. The mission will employ a unique orbital strategy of two main phases, in which the reference orbit apogee is placed at 12 R_e and 25 R_e, respectively, corresponding to the distances of the Earth's day-side magnetopause and night-side neutral sheet in the magnetotail where these processes are expected to be encountered. With perigee of both phases at 1.2 R_e this means a highly eccentric orbit, with $e = 0.81818$ in Phase I and $e = 0.9084$ in Phase II. This high eccentricity, combined with a moderate inclination of 28.5° (which makes the J_2 perturbation a significant factor), and the long duration of the mission make the design of a high quality, stable formation a challenging prospect. Furthermore, once such a formation has been designed, the limitations of on-board

*Part of this chapter is reprinted with permission from "Design of Satellite Formations in Orbits of High Eccentricity with Performance Constraints Specified over a Region of Interest" by Roscoe, C. W. T., Vadali, S. R., and Alfriend, K. T., 2011, *Advances in the Astronautical Sciences*, Vol. 139, pp. 145–162. Copyright 2011 by the American Astronautical Society.

*Part of this chapter is reprinted with permission from "Optimal Formation Design for Magnetospheric Multiscale Mission Using Differential Orbital Elements" by Roscoe, C. W. T., Vadali, S. R., Alfriend, K. T., and Desai, U. P., 2011, *Journal of Guidance, Control, and Dynamics*, Vol. 34, No. 4, pp. 1070–1080. Copyright 2011 by Christopher W. T. Roscoe, Srinivas R. Vadali, Kyle T. Alfriend, and Uri P. Desai.

*Part of this chapter is reprinted with permission from "Satellite formation design in orbits of high eccentricity with performance constraints specified over a region of interest: MMS phase II" by Roscoe, C. W. T., Vadali, S. R., Alfriend, K. T., Desai, U. P., 2012, *Acta Astronautica*. Copyright 2012 by Elsevier Ltd.

maneuvering and navigation systems make exactly achieving the desired formation impossible. The complete sets of reference orbital elements for MMS Phases I and II are listed in Table IV.1.

Both phases of the MMS mission call for a formation of four satellites which is to form a nearly regular tetrahedron near apogee. A formation with such a geometric shape is required in order to build a 3-dimensional model of the electric and magnetic fields governing the scientific processes being investigated. Different formation sizes are needed since it is unknown on exactly what length scale these processes will occur. Phase I requires tetrahedra with side lengths of 10 km, 25 km, 60 km, and 160 km; Phase II requires side lengths of 25 km, 40 km, 60 km, 160 km, and 400 km. The quality factor (QF) is a metric used to compare the size and shape of the instantaneous tetrahedron with a regular tetrahedron of acceptable size, defined on a range from 0 to 1, with 1 indicating a regular tetrahedron of acceptable size. The mission requires a QF which exceeds 0.7 for 80% of the time spent in the science Region of Interest (RoI), defined as all portions of the orbit above radius 9 R_e, for Phase I, and 15 R_e, for Phase II (resulting in a true anomaly range of approximately $\pm 20^\circ$ of apogee for both phases). Additionally, for collision avoidance the satellites

Table IV.1. MMS reference orbital elements.

	Phase I	Phase II
a (km)	42095	83554
e	0.81818	0.9084
i (deg)	28.5	
Ω (deg)	357.857	
ω (deg)	298.2253	
M_0 (deg)	180	

must remain at least 4 km apart at all times, and separations of greater than 6 km are desired near perigee due to the high speeds at which the spacecraft travel in that region.

A general method for designing formations to satisfy science return criteria was presented by Hughes [81] and applied to the single-orbit design of an MMS formation. The long-term formation design problem was addressed by Hughes [85], using a multi-revolution optimization approach with Cartesian position and velocity as the design parameters. Gim and Alfriend [84] presented a formation design approach for the MMS mission using differential mean orbital elements, and they investigated a number of properties of the tetrahedron formations, such as their initial orientation with respect to the orbital frame.

In this chapter, the formation design algorithms (FDAs) defined in Chapter III will be applied to the formation design problems of MMS Phases I and II. In addition, long-term stability and error sensitivity of MMS formations will be investigated in the presence of expected maneuver and navigation errors. Simulation results will be verified using the NASA General Mission Analysis Tool (GMAT), and a physical interpretation of the various formation design methods will be offered.

IV.A. Quality Factor

The MMS QF is a metric that determines, at a particular instant in time, the usefulness of the size and shape of the tetrahedron formed by the four MMS satellites. The QF is broken down into two subfunctions: Q_v that measures the quality of the shape of the tetrahedron and Q_s that measures the quality of the size

of the tetrahedron [81].

Based on the geometry shown in Figure III.1, the instantaneous volume of the tetrahedron formed by the four satellites can be computed using

$$V_a = \frac{1}{6} \left| \mathbf{r}_1 \cdot (\mathbf{r}_2 \times \mathbf{r}_3) \right| \tag{4.1}$$

where V_a stands for the volume of the actual tetrahedron, as opposed to the desired volume. There are six unique sides in the formation, three of which are already known. The remaining ones are

$$\mathbf{s}_4 = \mathbf{r}_2 - \mathbf{r}_1 \quad , \quad \mathbf{s}_5 = \mathbf{r}_3 - \mathbf{r}_1 \quad , \quad \mathbf{s}_6 = \mathbf{r}_3 - \mathbf{r}_2 \tag{4.2}$$

and the average side length is

$$\bar{L} = \frac{1}{6} \left(r_1 + r_2 + r_3 + s_4 + s_5 + s_6 \right) \tag{4.3}$$

The volume of a regular tetrahedron with side length equal to the average side length of the actual tetrahedron is

$$V_r = \frac{\sqrt{2}}{12} \bar{L}^3 \tag{4.4}$$

The volumetric performance metric for MMS is defined as the ratio of the actual tetrahedron volume to the volume of the desired regular tetrahedron [88, 89]:

$$Q_v = \frac{V_a}{V_r} = \frac{\sqrt{2}}{\bar{L}^3} \left| \mathbf{r}_1 \cdot (\mathbf{r}_2 \times \mathbf{r}_3) \right| \tag{4.5}$$

This metric has the useful property: $0 \leq Q_v \leq 1$. However, it does not take into account the actual size of the tetrahedron. Q_v will be equal to 1 when the volume of the tetrahedron equals that of a regular tetrahedron, and it will be equal to 0 when all four satellites lie in a plane.

A polynomial function is used as the size performance metric for MMS [81]:

$$Q_s\left(\bar{L}\right) = \begin{cases} 0 & \bar{L} < \ell_1 \\ \frac{\left(\bar{L}-\ell_1\right)^2\left(\bar{L}+\ell_1-2\ell_2\right)^2}{\left(\ell_2-\ell_1\right)^4} & \ell_1 \leq \bar{L} < \ell_2 \\ 1 & \ell_2 \leq \bar{L} \leq \ell_3 \\ \frac{\left(\bar{L}-\ell_4\right)^2\left(\bar{L}-2\ell_3+\ell_4\right)^2}{\left(\ell_4-\ell_3\right)^4} & \ell_3 < \bar{L} \leq \ell_4 \\ 0 & \bar{L} > \ell_4 \end{cases} \tag{4.6}$$

The constants ℓ_1, ℓ_2, ℓ_3, and ℓ_4 are used to change the shape of the function and are prescribed for the various formation sizes of interest for MMS. The important properties of this metric are that it will be equal to 1 when the formation is within a desired size range (based on its average side length), it will be equal to 0 when the formation size is unacceptable (either too large or too small), and it will vary continuously between 0 and 1 in the intermediate range.

The MMS QF is defined as the product of the volumetric performance metric and the size performance metric

$$Q = Q_v Q_s = \frac{\sqrt{2}Q_s}{\bar{L}^3}\left|\mathbf{r}_1 \cdot (\mathbf{r}_2 \times \mathbf{r}_3)\right| \tag{4.7}$$

With components expressed in frame $\mathcal{H}$, this vector equation becomes the matrix equation

$$Q = \frac{\sqrt{2}Q_s}{\bar{L}^3}\left|{}^h\mathbf{r}_1^T \ {}^h\mathbf{r}_2^\times \ {}^h\mathbf{r}_3\right| \tag{4.8}$$

where ${}^a\mathbf{v}^\times$ is the 3×3, skew-symmetric cross-product matrix of a vector $\mathbf{v}$ expressed in a frame $\mathcal{A}$

$$ {}^{a}\mathbf{v} = \begin{bmatrix} v_1 \\ v_2 \\ v_3 \end{bmatrix} \quad , \quad {}^{a}\mathbf{v}^{\times} = \begin{bmatrix} 0 & -v_3 & v_2 \\ v_3 & 0 & -v_1 \\ -v_2 & v_1 & 0 \end{bmatrix} \tag{4.9} $$

With this definition, the following vector-matrix equation holds for the cross product of two vectors $\mathbf{v}$ and $\mathbf{w}$:

$$ {}^{a}\left(\mathbf{v} \times \mathbf{w}\right) \;=\; {}^{a}\mathbf{v}^{\times}\ {}^{a}\mathbf{w} \tag{4.10} $$

The MMS mission requirements call for a QF that exceeds 0.7 for 80% of the time in the RoI. A good approximation to the QF requirement is that $\bar{Q}_{\mathrm{RoI}}$ exceeds 0.78[1], and it is this condition which will be used throughout the rest of this chapter to determine whether or not a given formation is satisfactory. In addition, a requirement is imposed such that the minimum separation distance between any pair of satellites, $d_{\min}$, must be greater than 6 km at all times—this is slightly more conservative than the actual mission requirement of 4 km at all times and 6 km near perigee.

[1]Personal communications with Steven P. Hughes, NASA Goddard Space Flight Center, Greenbelt, MD, 17 March 2010.

IV.A.1. Quality Factor Gradient

In order to use the optimal FDAs of Chapter III the gradient of Q with respect to the design variables $\delta\mathbf{e}_j$ must be determined. Proceeding in precisely the same manner as Hughes [81], the gradient of Q is obtained from Eq. (4.8):

$$\frac{\partial Q}{\partial \delta \mathbf{e}_j} = Q_s \frac{\partial Q_v}{\partial \delta \mathbf{e}_j} + Q_v \frac{\partial Q_s}{\partial \delta \mathbf{e}_j} \tag{4.11}$$

As noted in Section III.C, for the purposes of calculating the gradients, the linearization of the LVLH frame is acceptable—thus, it is again assumed that ${}^h\mathbf{r}_j \approx {}^c\mathbf{r}_j$ here. The gradients of Q_v and Q_s then become

$$\frac{\partial Q_v}{\partial \delta \mathbf{e}_j} = \frac{\sqrt{2}}{\bar{L}^3} \frac{\partial}{\partial \delta \mathbf{e}_j} \left| {}^h\mathbf{r}_1^T \ {}^h\mathbf{r}_2^\times \ {}^h\mathbf{r}_3 \right| - \frac{3\sqrt{2}}{\bar{L}^4} \left| {}^h\mathbf{r}_1^T \ {}^h\mathbf{r}_2^\times \ {}^h\mathbf{r}_3 \right| \frac{\partial \bar{L}}{\partial \delta \mathbf{e}_j} \tag{4.12}$$

$$\frac{\partial Q_s}{\partial \delta \mathbf{e}_j} = \frac{\partial Q_s}{\partial \bar{L}} \frac{\partial \bar{L}}{\partial \delta \mathbf{e}_j} \tag{4.13}$$

$$\begin{aligned} \frac{\partial}{\partial \delta \mathbf{e}_j} \left| {}^h\mathbf{r}_1^T \ {}^h\mathbf{r}_2^\times \ {}^h\mathbf{r}_3 \right| = \frac{{}^h\mathbf{r}_1^T \ {}^h\mathbf{r}_2^\times \ {}^h\mathbf{r}_3}{\left| {}^h\mathbf{r}_1^T \ {}^h\mathbf{r}_2^\times \ {}^h\mathbf{r}_3 \right|} \Bigg(& - {}^h\mathbf{r}_3^T \ {}^h\mathbf{r}_2^\times \frac{\partial \ {}^h\mathbf{r}_1}{\partial \delta \mathbf{e}_j} - {}^h\mathbf{r}_1^T \ {}^h\mathbf{r}_3^\times \frac{\partial \ {}^h\mathbf{r}_2}{\partial \delta \mathbf{e}_j} \\ & + {}^h\mathbf{r}_1^T \ {}^h\mathbf{r}_2^\times \frac{\partial \ {}^h\mathbf{r}_3}{\partial \delta \mathbf{e}_j} \Bigg) \end{aligned} \tag{4.14}$$

$$\begin{aligned} \frac{\partial \bar{L}}{\partial \delta \mathbf{e}_j} = \frac{1}{6} \Bigg[& \left(\frac{{}^h\mathbf{r}_1}{r_1} - \frac{{}^h\mathbf{s}_4}{s_4} - \frac{{}^h\mathbf{s}_5}{s_5} \right)^T \frac{\partial \ {}^h\mathbf{r}_1}{\partial \delta \mathbf{e}_j} \\ & + \left(\frac{{}^h\mathbf{r}_2}{r_2} + \frac{{}^h\mathbf{s}_4}{s_4} - \frac{{}^h\mathbf{s}_6}{s_6} \right)^T \frac{\partial \ {}^h\mathbf{r}_2}{\partial \delta \mathbf{e}_j} \\ & + \left(\frac{{}^h\mathbf{r}_3}{r_3} + \frac{{}^h\mathbf{s}_5}{s_5} + \frac{{}^h\mathbf{s}_6}{s_6} \right)^T \frac{\partial \ {}^h\mathbf{r}_3}{\partial \delta \mathbf{e}_j} \Bigg] \end{aligned} \tag{4.15}$$

$$\frac{\partial Q_s}{\partial \bar{L}} = \begin{cases} 0 & \bar{L} < \ell_1 \\ \frac{4\left(\bar{L}-\ell_1\right)\left(\bar{L}+\ell_1-2\ell_2\right)\left(\bar{L}-\ell_2\right)}{\left(\ell_2-\ell_1\right)^4} & \ell_1 \le \bar{L} < \ell_2 \\ 0 & \ell_2 \le \bar{L} \le \ell_3 \\ \frac{4\left(\bar{L}-\ell_4\right)\left(\bar{L}-2\ell_3+\ell_4\right)\left(\bar{L}-\ell_3\right)}{\left(\ell_4-\ell_3\right)^4} & \ell_3 < \bar{L} \le \ell_4 \\ 0 & \bar{L} > \ell_4 \end{cases} \tag{4.16}$$

IV.B. Quantification of Errors

Hughes [85] performed an extensive error sensitivity analysis for the MMS mission. Error sources—including maneuver magnitude, direction, and timing as well as navigation—were evaluated by comparing the resulting differential semimajor axis errors. As noted in Section III.D.3, it is reasonable to examine only errors in δa since their effect on formation stability is $\mathcal{O}(1)$, whereas the effect of errors in any other element is $\mathcal{O}(J_2)$ or smaller.

According to the statistical model described by Hughes [85], δa errors due to maneuver magnitude errors are distributed normally with a mean of 0 and a standard deviation σ of about 17 m. δa errors due to maneuver direction errors are distributed normally with $\sigma \approx 3$ m. For Phase I, the worst-case maneuver timing error results in a δa error of about 4 m, and navigation errors result in δa errors normally distributed with $\sigma \approx 1$ m. For Phase II, the worst-case maneuver timing error results in a δa error of about 7 m, and navigation errors result in δa errors normally distributed with $\sigma \approx 2$ m. To account for all of these error sources, in the present work a slightly conservative estimate of $3\sigma = 80$ m is used for the distribution of δa errors in Phase I and $3\sigma = 100$ m for Phase II.

IV.C. Phase I

In this section, the complete formation design for MMS Phase I will be performed using the methods of Chapter III. First, the nominal FDAs will be applied to the error-free design case. Second, the performance of the nominally designed FDAs will be evaluated in the presence of δa errors. Third, the robust FDA will be used to

improve performance in the presence of errors. Finally, the results will be verified by simulation in GMAT.

IV.C.1. Nominal Formation Design

The results of using the nominal FDAs defined in Section III.C, the single-orbit constrained (SOC) optimization and the multi-obit unconstrained (MOU) optimization, to design a 10 km tetrahedral formation are shown in Figure IV.1 for a variety of optimization parameters: SOC optimization with $k_j = 1$ for all deputies, SOC optimization with $k_j = 3$ for all deputies, MOU optimization with $N_{\text{orb}} = 60$, and MOU optimization with $N_{\text{orb}} = 90$. Results are evaluated by comparing the evolution of the average QF in the RoI over a number of orbits. Initial guesses for the optimizations were generated using the method of Section III.B to specify a regular tetrahedron at apogee of the initial orbit.

Examining the SOC result with $k_j = 1$ first (which corresponds to the traditional along-track drift condition of Eq. (3.3)), this result violates the $\bar{Q}_{\text{RoI}} \geq 0.78$

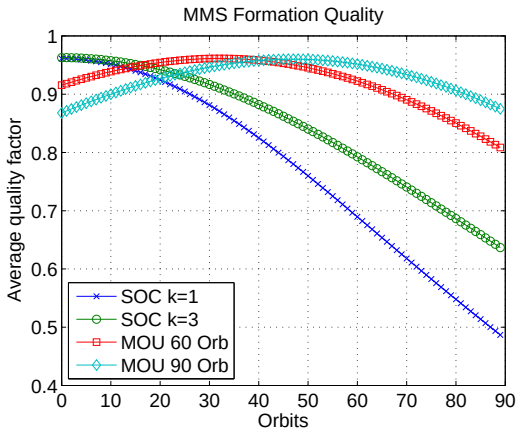

Figure IV.1. Comparison of average QF per RoI pass for 10 km Phase I formation.

requirement after approximately 45 days (1 orbit $\approx$ 1 day). On the other hand, the SOC result with $k_j = 3$ does not violate this requirement until approximately 65 days. Clearly, the traditional along-track drift condition is not optimal for problems such as this one in which performance constraints are only specified throughout part of the orbit, as suggested in Section III.A.1.

Both of the MOU results satisfy the $\bar{Q}_{\mathrm{RoI}}$ requirement for more than 90 days. Their most striking feature, however, is the fact that the peak QF has moved from the first orbit to about halfway through the optimization time frame, and the rest of the results are approximately symmetric about this point. This is not the first time symmetry has appeared in relation to this problem: the QF for optimal formations is also symmetric about apogee within each orbit [81]. The symmetry of the MOU optimization result was also noted by Hughes [85]. This type of symmetry could also be produced using the SOC method by optimizing a later orbit and then propagating the design variables back to a different initial time t_0. The optimized initial differential classical mean orbital elements for the 60 and 90 orbit MOU optimizations are listed in Table IV.2. The results of performing the MOU optimization over 60 orbits are shown in Figure IV.2 for all of the remaining MMS Phase I formation sizes, and they are very similar to the 10 km formation results. This is an indication that nonlinear effects on the performance measure may not be significant for the formation sizes and reference orbit considered here.

Table IV.2. MOU optimized initial differential mean orbital elements for 10 km Phase I formation.

	60 Orbit MOU			90 Orbit MOU		
	1	2	3	1	2	3
δa (10^{-2} km)	2.7798	1.2337	1.1075	−1.0505	−2.6651	−0.9956
δe (10^{-4})	1.1289	0.5138	0.5076	−0.4966	−1.1068	−0.4270
δi (10^{-3} deg)	−0.7684	−2.9939	0.2346	0.5115	0.9352	3.1723
$\delta\Omega$ (10^{-3} deg)	5.9210	−3.2803	5.7262	−4.8813	−6.2941	4.5884
$\delta\omega$ (10^{-3} deg)	−7.6302	6.1207	1.3357	−1.7756	9.2095	−5.7428
δM_0 (10^{-2} deg)	0.8895	−1.0073	−1.7281	1.7096	−1.2715	0.6481

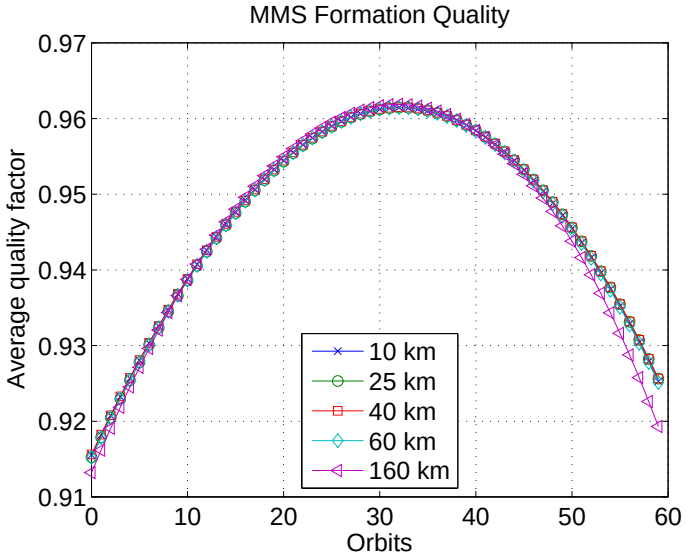

Figure IV.2. Average QF per RoI pass for 60 orbit MOU optimization for Phase I formations.

IV.C.2. Determination of k_j Factor

In order to obtain the best possible results from the SOC optimization using the modified along-track drift condition, appropriate values of k_j must be found to emulate the long-term stability of the MOU-designed formations. To see if such a condition is reasonable, the average drift rates of the three deputies resulting from the 10 km, 60 orbit MOU optimization are extracted and substituted into Eq. (3.7).

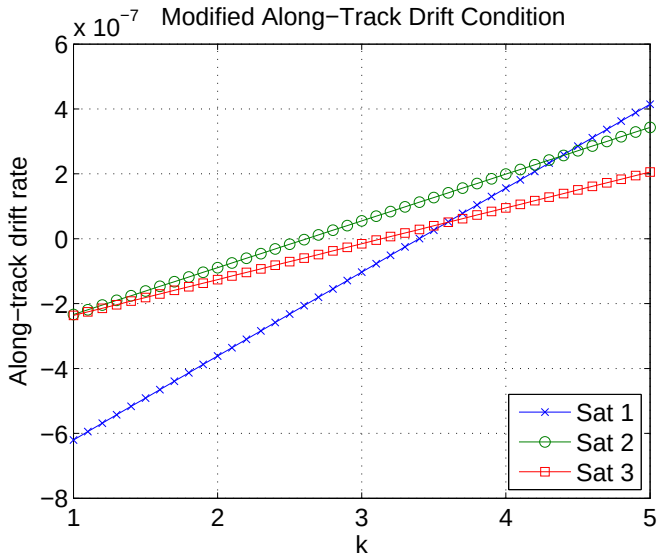

Figure IV.3. Modified drift rates for 60 orbit MOU optimization result.

The results are plotted in Figure IV.3 for different values of k_j. Eq. (3.7) is satisfied for $k_j = 3.40$, 2.62, and 3.14 for each of the deputies, respectively. The resulting k_j values for the other formation sizes and MOU optimization ranges are listed in Table IV.3. In each set of results, the average k_j is approximately equal to 3 and the individual k_j values are distributed in a common pattern (different ordering of the results indicates an exchange in the vertices of the tetrahedron).

A similar number for k (same for all the satellites) can also be obtained by evaluating the SOC optimization result. Figure IV.4 is generated by applying the

Table IV.3. k_j values from Phase I MOU optimization.

	Formation Size (60 orbits)					Orbits (10 km)		
	10 km	25 km	40 km	60 km	160 km	60	90	120
k_1	3.40	3.07	3.10	3.06	3.07	3.40	2.81	2.76
k_2	2.62	3.40	3.41	3.40	3.23	2.62	3.29	3.23
k_3	3.14	2.61	2.62	2.61	2.53	3.14	2.37	2.27

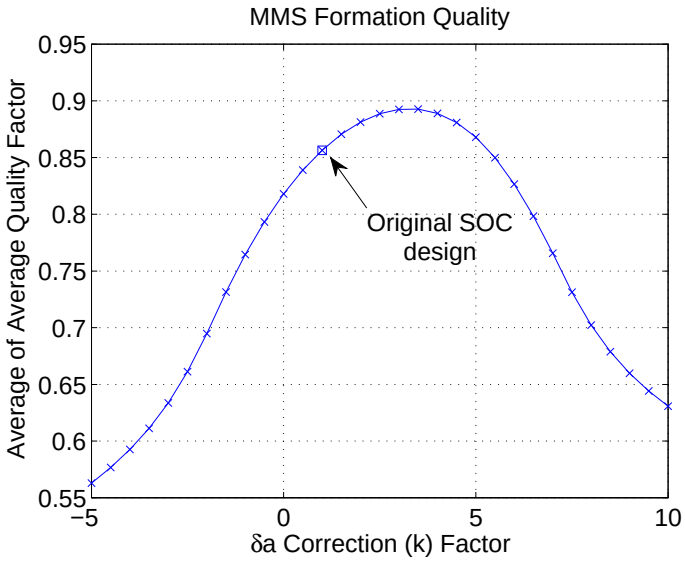

Figure IV.4. Average of average QF in RoI over 60 orbits for Phase I SOC optimization result.

modified δa_j condition, Eq. (3.8), to the initial conditions for each of the satellites resulting from the SOC optimization and propagating for 60 orbits. To maintain the same initial formation size and shape, Eq. (3.21) is also applied. The resulting averages of $\bar{Q}_{\text{RoI}}$ over 60 orbits show that the best value of k for this problem is a little greater than 3.

Finally, at the entry and exit of the RoI, that is for $f = \frac{8}{9}\pi$ or $f = \frac{10}{9}\pi$, Eq. (3.9) yields an instantaneous value of 3.56 for $k_{j,\text{inst}}$, a value in the neighbourhood of those shown in Table IV.3 and obtained from Figure IV.4. Indeed, comparing the value of $\bar{Q}_{\text{RoI}}$ for the SOC design with $k_j = 3$ after 60 days to the value of $\bar{Q}_{\text{RoI}}$ for the 60 orbit MOU design after 90 days (since the peak $\bar{Q}_{\text{RoI}}$ occurs at 30 days in that result) in Figure IV.1, the terminal performance is observed to be only marginally better in the MOU optimization case. However, the peak $\bar{Q}_{\text{RoI}}$ is slightly higher in the SOC result and the optimization process is far more computationally efficient. The

optimized initial differential classical mean orbital elements for the SOC optimization with $k_j = 3$ are listed in Table IV.4.

Table IV.4. SOC (with $k_j = 3$) optimized initial differential mean orbital elements for 10 km Phase I formation.

	Satellite		
	1	2	3
δa (10^{-2} km)	2.4203	1.5297	1.0653
δe (10^{-4})	1.1277	0.5897	0.5888
δi (10^{-3} deg)	−0.0096	−2.7459	2.0545
$\delta\Omega$ (10^{-3} deg)	0.0667	−3.0826	2.7671
$\delta\omega$ (10^{-3} deg)	−0.3977	8.3910	4.0127
δM_0 (10^{-2} deg)	0.0990	−1.5555	−1.7580

IV.C.3. Performance in the Presence of Errors

To measure the performance of a given formation in the presence of δa errors, the formation lifetime T is defined as the number of days that a formation satisfies the MMS mission requirements ($\bar{Q}_{\text{RoI}} \geq 0.78$ and $d_{\min} > 6$ km). The distribution of T values resulting from the expected δa error distribution will determine the performance of a given formation design. In particular, it is desired that the formation has a high mean T and a high probability that T will be greater than 14 days.

The results of performing Monte Carlo analyses on the 10 km SOC (with $k_j = 3$), 60 orbit MOU, and 90 orbit MOU optimized formations are summarized in Table IV.5. However, since the initial SOC and MOU optimizations for the 10 km formations generally result in initial separation distances of about 5 km, only QF performance is considered here and no minimum separation requirement is imposed. Each set of results was obtained by sampling a $3\sigma = 80$ m normal distribution for

the δa error of each deputy, using Latin hypercube sampling, and running 5000 simulations in MATLAB to calculate the T distribution. The quantities listed are the minimum $T_{\min}$, maximum $T_{\max}$, mean $\bar{T}$ time to $\bar{Q}_{\text{RoI}} < 0.78$, and the probability that T is less than or equal to 14 days, $P_T\left(T \leq 14\right)$. The note "peak" means that the location of the maximum $\bar{Q}_{\text{RoI}}$ has been shifted to the indicated orbit number, since the MOU optimization generally produces solutions in which the maximum $\bar{Q}_{\text{RoI}}$ does not occur in the first orbit.

In the absence of errors, the 10 km SOC, 60 orbit MOU, and 90 orbit MOU optimized formations satisfy the QF requirement for 65, 95, and 110 days, respectively. However, the performance of these formations is quite poor in the presence of errors, without even considering the additional minimum separation distance requirement. Examining Figure IV.5(a), which shows a histogram of the T distribution for the 60 orbit MOU case, it is clear that very few of the cases are in the vicinity of the ideal result, and most of them have much lower T values. Similarly, in Figures IV.6(a)–(c), which show the distribution of T with respect to the δa errors of the deputies, the majority of the data is concentrated at the base of the distribution, with very few near the narrow peak. The same behavior was observed in each of the Monte Carlo

Table IV.5. Monte Carlo results for 10 km SOC and MOU optimizations.

Optimization	$T_{\min}$	$T_{\max}$	T	$P_T\left(T \leq 14\right)$
SOC	7	66	26.8	0.085
MOU 60 Orb	7	97	30.6	0.082
MOU 60 Orb (peak 22)	7	86	27.8	0.118
MOU 60 Orb (peak 0)	7	68	25.5	0.143
MOU 90 Orb	5	110	27.5	0.202
MOU 90 Orb (peak 26)	6	89	27.9	0.130
MOU 90 Orb (peak 0)	7	71	25.2	0.162

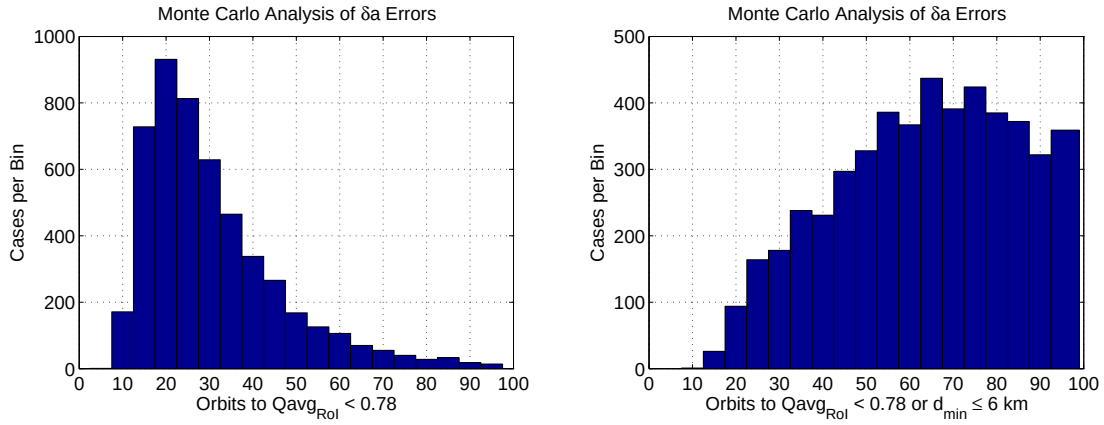

(a) 10 km formation. **(b) 25 km formation.**

Figure IV.5. Effect of $3\sigma = 80$ m δa errors in each deputy on 60 orbit MOU optimization.

simulations listed in Table IV.5.

The larger formation sizes perform better in the presence of errors than do the 10 km ones. The results of performing Monte Carlo analyses on the remaining MMS Phase I formation sizes—including the minimum separation requirement—are summarized in Table IV.6 for the 60 orbit MOU optimized formations. The results for the 60 km and 160 km formations are very good, considering that the total time MMS Phase I will spend in these formations is 15 days each. The results for the 25 km formation are adequate but could be improved, especially in the lower limit. Figure IV.5(b) shows a histogram of the T distribution for this case, in which a large portion of the data is located near the higher end of the distribution, with a fairly wide base extending towards the lower end.

According to the results of Section IV.C.1, the size of the desired tetrahedron does not significantly affect the QF evolution of the optimized formation designs for MMS, since nonlinear effects in the dynamics are very small compared with J_2

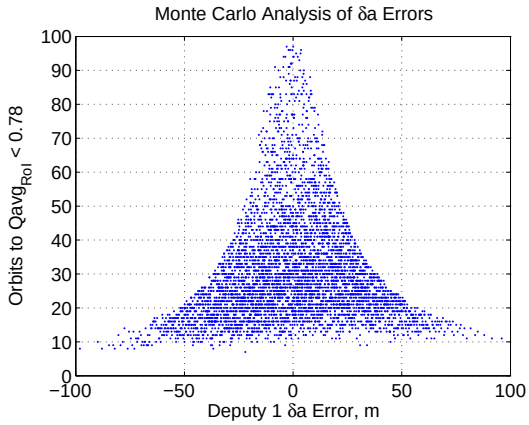

(a) Deputy 1.

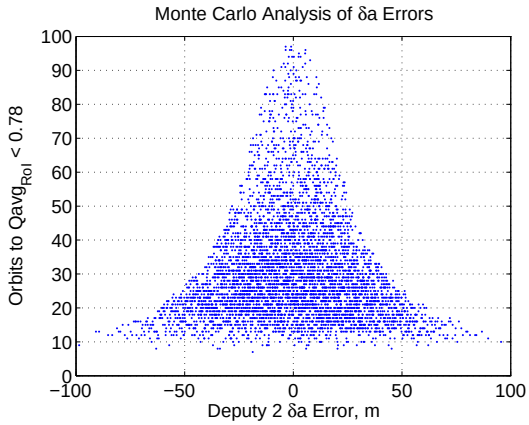

(b) Deputy 2.

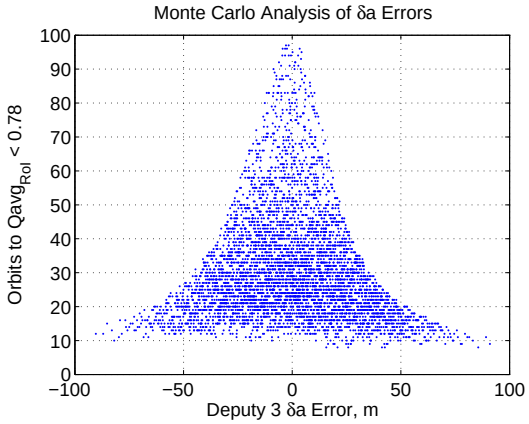

(c) Deputy 3.

Figure IV.6. T distribution for $3\sigma = 80$ m δa errors applied to 60 orbit MOU optimization.

and other perturbations. In fact, in Figure IV.2 the 60 orbit MOU optimization results were observed to be virtually identical for all of the Phase I formation sizes

Table IV.6. Monte Carlo results for 60 orbit MOU optimizations.

Formation Size	$T_{\min}$	$T_{\max}$	T	$P_T\,(T \leq 14)$
25 km	12	99	63.1	0.001
60 km	36	98	85.0	0
160 km	73	95	87.3	0

considered. Why, then, does formation size have a significant effect on the Monte Carlo analysis performed in this section?

There are two reasons: first, the minimum separation distance requirement and, second, the scaling of the formation size parameters. Since the $d_{\min}$ requirement is stated as an absolute distance (6 km) it will have much more of an effect on small formations sizes than on larger ones. In the analysis of the 10 km formations, this requirement was not even included, because all of the formation designs would have failed on the first orbit. For the 25 km formations, this requirement has some effect, producing several of the lower values of T in the distribution, but only for certain combinations of the deputies' δa errors. The 60 km and 160 km formations are completely unaffected by this requirement.

The effect of scaling the formation size parameters can be best illustrated by way of a simple example. Consider the total drift in position per orbit ρ_d resulting from a δa error for a single deputy in an unperturbed reference orbit [26],

$$\rho_d = \delta a \frac{3\pi}{\eta} \sqrt{1 + e^2 + 2e \cos f_0} \tag{4.17}$$

where f_0 is the true anomaly being considered, since in an eccentric reference orbit the drift will be different at different points in the orbit. Without perturbations, the drift rate depends on non-zero δa and not directly on the overall distance between the satellites. Therefore, a small formation will experience the same amount of drift as a larger one, although the drift will seem much larger when compared to the actual formation size. When J_2 is included, the effect of $\delta a/a$ will also cause drift of $\mathcal{O}(J_2)$ whereas the effects of δe and δi are of $\mathcal{O}(J_2^2)$.

Additionally, the Q_s side length parameters ℓ_1–ℓ_4 scale with formation size and

are consequently spaced farther apart for larger formations, and the average side length appears in the denominator of Q_v (Eq. (4.5)), thus tolerating greater absolute variations in side length throughout the RoI. It can then be concluded that a given δa error will have a greater effect on the QF of a small formation than it will on a larger one (not considering nonlinear effects), and in general the smaller formation sizes can be expected to fail the $\bar{Q}_{\text{RoI}}$ requirement sooner than the larger ones when considering the same error magnitudes.

IV.C.4. Robust Formation Design

The robust FDA defined in Section III.D is implemented by first performing either an SOC or MOU optimization, and then using that design as the initial guess for the robust optimizer. The δa error distribution is sampled at three points for each deputy, -3σ, 0, and 3σ, and a tuning parameter of $w = 9$ was selected based on the results of several test cases. For the 10 km formation size, some care had to be taken in generating the initial guess for the robust optimization in order to ensure acceptable performance in terms of the $d_{\min}$ requirement. As mentioned in Section IV.C.3, the 10 km formation optimizations generally produce results with initial side lengths of about 5 km, which is unacceptable. However, there is some flexibility in the range of possible side lengths provided by the definition of Q_s. The side length parameters for the 10 km formation are $\ell_1 = 4$ km, $\ell_2 = 6$ km, $\ell_3 = 18$ km, and $\ell_4 = 25$ km; it was found that selecting an initial tetrahedron for the SOC optimization with sides of 18 km (instead of 10 km) converged to a solution with an initial side length of about 13 km, which then produced better results in the

robust optimization process.

The results of Monte Carlo simulations for several different robust optimizations of the 10 km formation for MMS Phase I are listed in Table IV.7, with the minimum separation requirement enforced. In each Monte Carlo simulation 5000 cases were considered, with δa errors generated in the same manner as was described in Section IV.C.3. All of the robust optimized formations exhibit better overall behavior in the presence of δa errors than did those of the previous analyses (in Table IV.5). In general, the robust optimization process produces narrower and more even histograms of the formation lifetime T at a cost of some degradation in performance near the ideal case, as was expected. There are small differences between using the SOC or MOU optimizations to provide the initial guess, but the SOC method (with $k_j = 3$) produces acceptable results at a fraction of the computational requirement of the MOU method. The effect of varying N_{orb} in the robust optimization can be seen in Figures IV.7(a)–(d): lowering N_{orb} essentially narrows the histogram and increases the likelihood that the data will be near the mean value. Figures IV.8(a)–(c) show the distribution of T with respect to the δa errors of the deputies, which clearly

Table IV.7. Monte Carlo results for 10 km robust optimizations.

Initial Design	N_{orb}	T_{min}	T_{max}	T	$P_T\,(T \leq 14)$
SOC	60	8	83	42.4	0.034
MOU 60 Orb	60	9	82	44.7	0.015
MOU 90 Orb	60	8	85	41.1	0.034
SOC	40	10	75	45.6	0.005
SOC	30	12	77	44.2	0.004
MOU 60 Orb	30	9	73	43.9	0.018
MOU 90 Orb	30	11	80	42.7	0.006
SOC	20	11	73	43.3	0.003
SOC	10	11	68	41.9	0.002

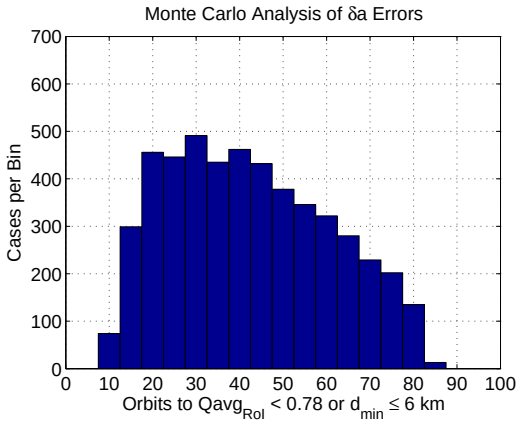

(a) 60 Orbit Robust.

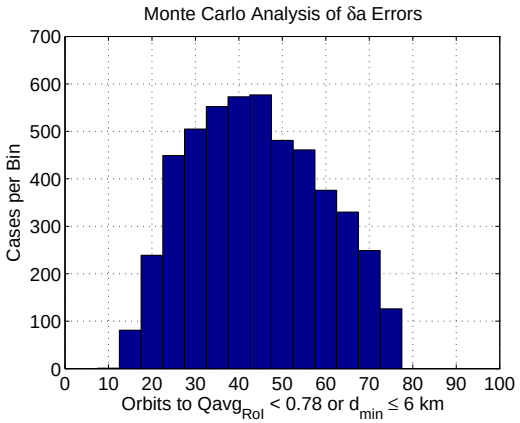

(b) 30 Orbit Robust.

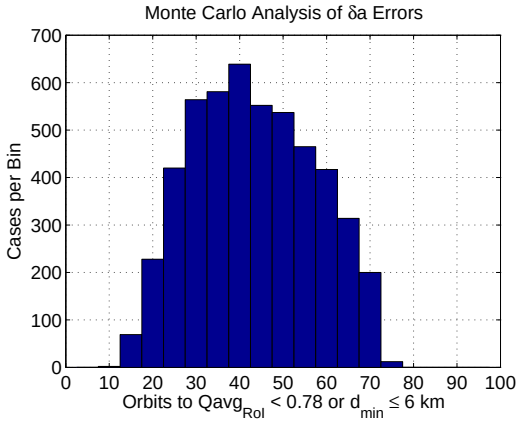

(c) 20 Orbit Robust.

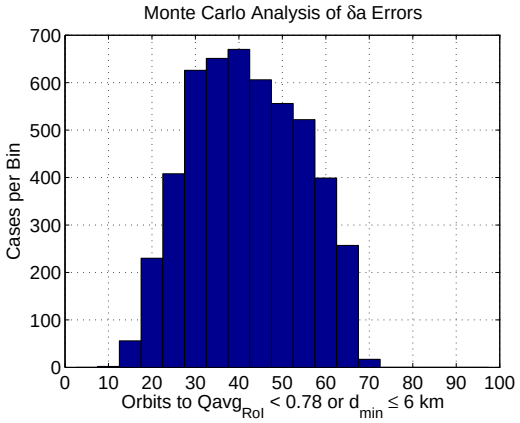

(d) 10 Orbit Robust.

Figure IV.7. Effect of $3\sigma = 80$ m δa errors on robust optimization of the 10 km SOC result.

shows an improvement over the 10 km formation results of Section IV.C.3 (which did not include the $d_{\min}$ requirement). The initial differential classical mean orbital elements for the 30 orbit robust optimization of the 10 km SOC formation are listed in Table IV.8.

The results of Monte Carlo simulations for the robust optimization of the 25 km formation are listed in Table IV.9. As was the case with the 10 km simulations, there

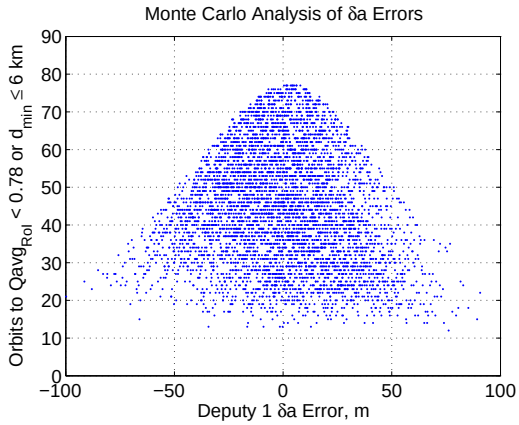

(a) Deputy 1.

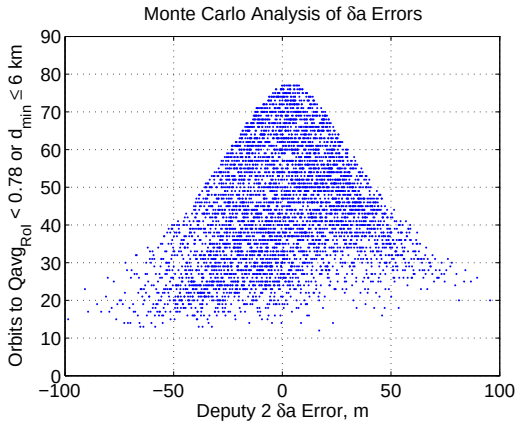

(b) Deputy 2.

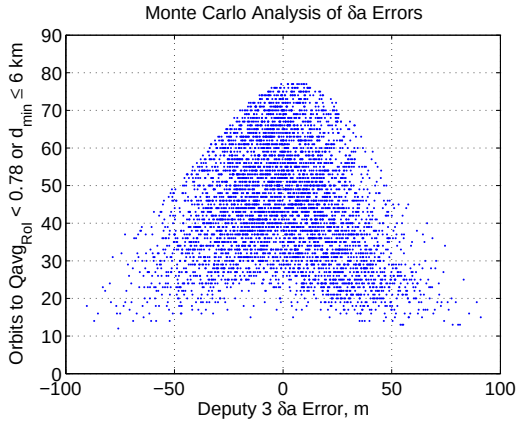

(c) Deputy 3.

Figure IV.8. T distribution for $3\sigma = 80$ m δa errors applied to the 10 km, 30 orbit robust SOC result.

is a marked improvement over the non-robust performance. In Figures IV.9(a) and (b), the same narrowing of the histogram is evident as N_{orb} gets smaller, although there is little effect when it is decreased below 40 orbits. The initial differential classical mean orbital elements for the 25 km, 40 orbit robust optimization are listed in Table IV.8 as well.

Table IV.8. Robust optimized differential mean elements from SOC initial design.

	10 km, 30 Orbit Robust			25 km, 40 Orbit Robust		
	1	2	3	1	2	3
δa (m)	−40.175	−52.664	−40.977	−90.335	−72.019	−83.197
δe (10^{-4})	−1.944	−2.528	−1.629	−4.436	−3.669	−3.438
δi (10^{-3} deg)	−1.593	−1.636	6.257	−5.024	−6.949	9.801
$\delta\Omega$ (10^{-2} deg)	−0.201	−0.109	1.350	−0.534	−0.119	1.997
$\delta\omega$ (10^{-2} deg)	−0.950	1.031	−1.275	−0.172	2.962	−0.545
δM_0 (10^{-2} deg)	2.838	−2.553	−0.014	1.115	−8.748	−4.245

Table IV.9. Monte Carlo results for 25 km robust optimizations.

Initial Design	N_{orb}	$T_{\min}$	$T_{\max}$	$\bar{T}$	$P_T\,(T \leq 14)$
SOC	60	12	87	65.0	0.000
MOU 60 Orb	60	24	87	68.2	0
SOC	40	27	79	63.2	0
SOC	30	25	75	60.7	0

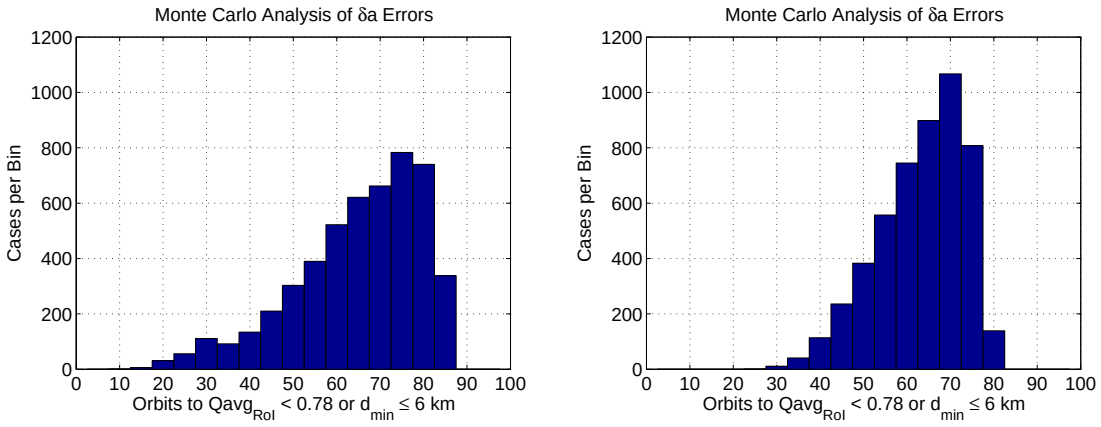

(a) 60 Orbit Robust. **(b) 40 Orbit Robust.**

Figure IV.9. Effect of $3\sigma = 80$ m δa errors on the 25 km, robust optimization of the SOC result.

IV.C.5. GMAT Verification

The Gim-Alfriend state transition matrix (G-A STM) is accurate for small satellite separations and contains terms up to first-order in J_2. Because of the high ec-

centricity of the reference orbit and the long duration of the mission, it is expected that the accuracy of the predicted motion of the satellites will degrade after a certain amount of time. Therefore, the results predicted in the previous sections will now be compared to results obtained from GMAT, using a fourth-degree, fourth-order gravity model, along with the solar and lunar gravity perturbations and the solar radiation pressure.

The average QF predicted by the G-A STM is compared to the GMAT results in Figures IV.10 for the 60 orbit MOU optimization of all of the Phase I MMS formation sizes. Note that two distinct classes of curves are apparent, will all of the G-A STM results overlapping on the upper curve and all of the GMAT results on the lower. The 60 orbit results differ only slightly after 60 days, by about 0.04 in average QF prediction. Even in the GMAT results there is no appreciable difference in QF between the various formation sizes, confirming the previous hypothesis that nonlinear effects are not significant in this problem.

Figure IV.11(a) shows the instantaneous QF for the 90 orbit MOU optimization of the 10 km formation, along with $\bar{Q}_{\text{RoI}}$. The accuracy of the G-A STM prediction is reasonable up to about 70 days. Figure IV.11(b) shows the instantaneous QF and $\bar{Q}_{\text{RoI}}$ for the 120 orbit MOU optimization of the 10 km formation. Also compared are two sets of GMAT outputs: one obtained by propagating with only first-order J_2 terms, with no other perturbations, and the other using the full perturbed gravity model described above. The G-A STM result is very close to the GMAT first-order J_2 result, which includes nonlinear effects; this further confirms that the effect of the linearization assumption is small compared to the effects of higher-order J_2 terms and

other gravitational perturbations. According to the GMAT results, the formation can satisfy the $\bar{Q}_{\mathrm{RoI}}$ requirement for more than 80 days, in the absence of initialization errors.

Four of the robust optimized formation designs described in Section IV.C.4 will be verified using GMAT as well. For each one, 1000 cases are simulated with δa errors using the same gravity model once again. Only 1000 cases are simulated in GMAT, compared to 5000 cases in MATLAB, because of the significantly longer simulation time required.

Table IV.10 lists results for the GMAT Monte Carlo simulations of the 10 km, 30 orbit robust optimized formations for the SOC, 60 orbit MOU, and 90 orbit MOU initial designs. Comparing these results with those of Table IV.7, it is clear that the GMAT results generally predict a shorter maximum formation lifetime than do the G-A STM ones, consequently lowering the mean T value as well. This is consistent

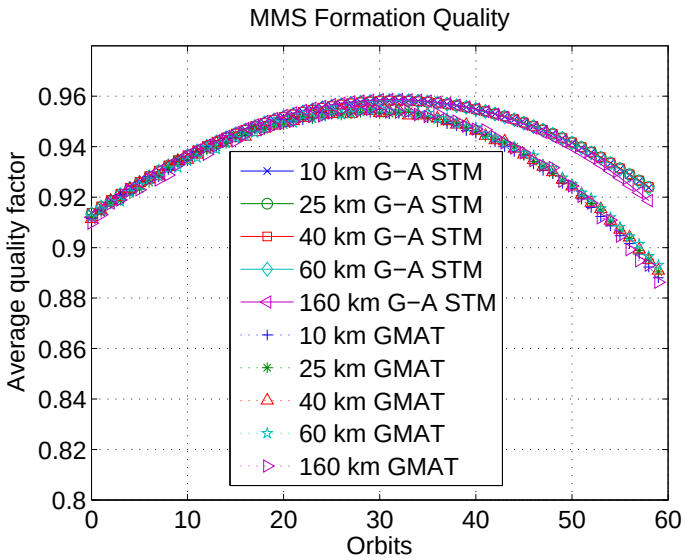

Figure IV.10. Average QF prediction compared to GMAT for Phase I.

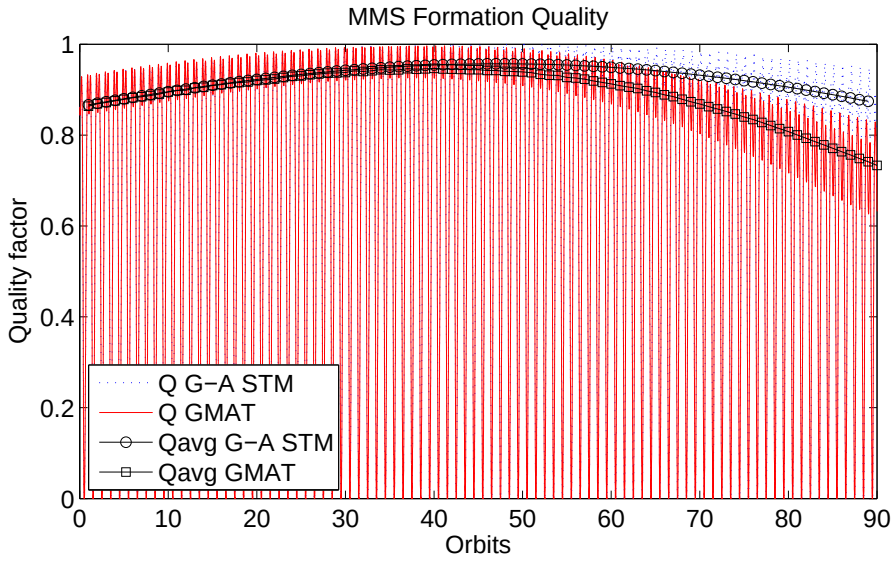

(a) 90 Orbit MOU.

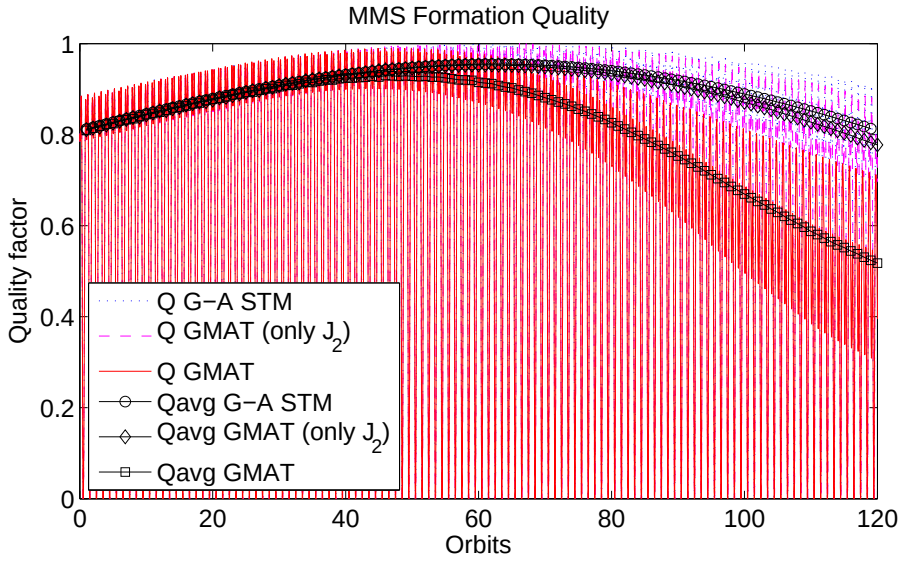

(b) 120 Orbit MOU.

Figure IV.11. Instantaneous QF prediction compared to GMAT for Phase I.

with the observations of the previous paragraphs. A histogram of the T distribution for the robust optimized SOC result is shown in Figure IV.12(a). Comparing this to

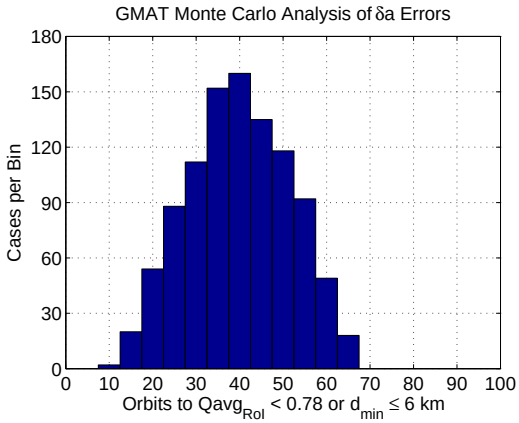

(a) 10 km, 30 Orbit Robust from SOC.

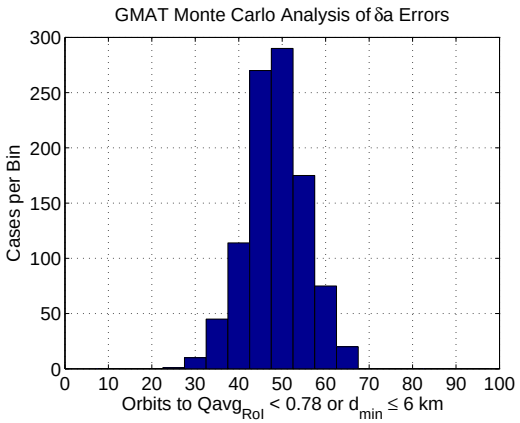

(b) 25 km, 40 Orbit Robust from SOC.

Figure IV.12. Effect of $3\sigma = 80$ m δa errors on robust optimizations, simulated in GMAT.

Figure IV.7(b), there is good agreement in the lower end of the distribution, with a much higher peak at about 40 orbits, after which the GMAT results fall off more quickly, as expected.

The results for the 25 km, 40 orbit robust optimized SOC formation are also listed in Table IV.10 and a histogram is plotted in Figure IV.12(b). As was the case with the 10 km results, there is good agreement with the G-A STM results of Figure IV.9(b) at the lower end of the distribution, a higher peak near the GMAT mean, and lower values for the upper end of the distribution.

Table IV.10. GMAT Monte Carlo results for robust optimizations.

Initial Design	N_{orb}	$T_{\min}$	$T_{\max}$	T	$P_T\,(T \leq 14)$
10 km					
SOC	30	11	66	39.8	0.008
MOU 60 Orb	30	10	65	37.7	0.018
MOU 90 Orb	30	12	69	38.5	0.005
25 km					
SOC	40	26	67	48.6	0

IV.D. Phase II

In this section, the complete formation design for MMS Phase II will be performed using the methods of Chapter III. The extremely high eccentricity and apogee of the Phase II reference orbit, as well as the nearly 3 day orbit period, mean that the satellites will spend a very long time at high altitude in the RoI. These factors, coupled with the large formation sizes, suggest that the build-up of perturbation and nonlinear effects will make designing acceptable formations with long-term, passive stability in Phase II a more difficult prospect than in Phase I.

IV.D.1. Nominal Formation Design

The results of performing the MOU optimization over 20 orbits are shown in Figure IV.13 for all of the MMS Phase II formation sizes. All of the resulting formations satisfy the QF requirement for more than 20 orbits (≈ 58 days), and the same symmetry in $\bar{Q}_{\text{RoI}}$ (with respect to the peak value) is present here as was observed in Section IV.C.1 for the Phase I formations.

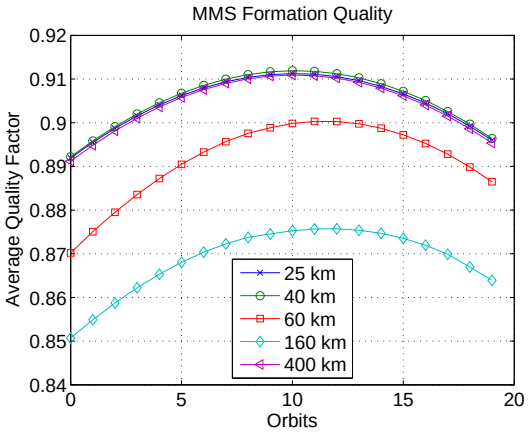

Figure IV.13. Average QF per RoI pass for 20 orbit MOU optimization.

In the Phase I results, all of the formation sizes exhibited roughly the same $\bar{Q}_{\text{RoI}}$ performance, indicating that size had little effect on the overall design using the G-A STM. In this case, the 60 km and 160 km formation sizes do not perform as well as the other sizes; however, the source of this discrepancy can be traced back to the definition of the Q_s side length parameters, ℓ_1–ℓ_4.

The Q_s parameters prescribed for MMS Phase II are listed in Table IV.11. Note that for the 25 km, 40 km, and 400 km formations the ratio of ℓ_1 to the formation size is approximately 0.6, but for the 60 km and 160 km formations it is approximately 0.75 and 0.84, respectively. Similarly, the ratio of ℓ_2 to the formation size is approximately 0.8 (for 25 km, 40 km, and 400 km) versus 0.83 and 0.88; for ℓ_3 it is 1.4 versus 1.25 and 1.2; and for ℓ_4 it is 1.6 versus 1.3. In Phase I, the difference in these ratios did not significantly affect the QF in the RoI because the average side lengths of the tetrahedra generally remained well within the ℓ_2–ℓ_3 range throughout the entire RoI. In Phase II, however, the higher eccentricity of the reference orbit means that the relative motion of the satellites will cover a larger range of distances throughout a given true anomaly span, and consequently the average side lengths of the tetrahedra do not remain between ℓ_2 and ℓ_3 throughout the RoI. Since the ratios of the side length parameters to the formation scale size are more restrictive

Table IV.11. Q_s side length parameters for MMS Phase II.

	Formation Size				
	25 km	40 km	60 km	160 km	400 km
ℓ_1	15	25	45	135	250
ℓ_2	20	30	50	140	300
ℓ_3	35	55	75	190	550
ℓ_4	40	65	80	210	600

for the 60 km and 160 km formations, the QF performance for these formations will be somewhat lower than for the other sizes, as seen in the preceding simulations.

The collision avoidance constraint can be checked by examining the evolution of the tetrahedron side lengths over time, shown for the 25 km MOU optimization in Figure IV.14. The dashed line at the bottom represents the required 6 km minimum separation distance. Note that, although no side length constraint was included in the optimization, this constraint is satisfied at all times, and the closest approach between any two satellites is 13.7 km in the 25 km formation result. The optimized initial differential classical mean orbital elements for the 25 km MOU optimization are listed in Table IV.12.

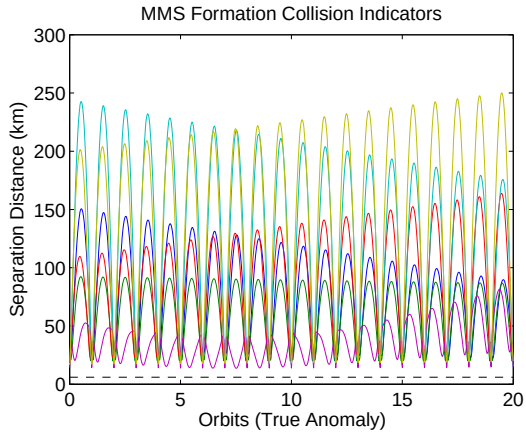

Figure IV.14. Collision indicators for 25 km Phase II MOU optimization.

IV.D.2. Determination of k_j Factor

As was the case in Section IV.C.2, in order to obtain useful results from the SOC optimization, care must first be taken to determine optimal values for the k_j parameters for MMS Phase II. Proceeding as before, the modified drift rates resulting

Table IV.12. 25 km MOU optimized differential mean orbital elements.

	20 Orbit MOU		
	1	2	3
δa (m)	−34.975	−93.071	−40.746
δe (10^{-4})	−1.6140	−3.7634	−1.6800
δi (10^{-2} deg)	−0.0293	0.2785	1.0334
$\delta\Omega$ (10^{-2} deg)	−1.7213	−2.0455	1.1784
$\delta\omega$ (10^{-2} deg)	−0.6954	2.5456	−2.0441
δM_0 (10^{-2} deg)	6.0420	−2.8072	3.1631

from the 25 km MOU optimization are plotted in Figure IV.15(a) for various values of k_j. Eq. (3.7) is satisfied for $k_j = 4.31$, 1.26, and 3.19 for each of the deputies, respectively, and the resulting k_j values for the other formation sizes are listed in Table IV.13. At the entry and exit of the RoI for Phase II, Eq. (3.9) yields an instantaneous value of 3.41 for $k_{j,\text{inst}}$ a value in the neighbourhood of most of those shown in Table IV.13.

Unfortunately, there is much more variation in k_j between the three deputies in

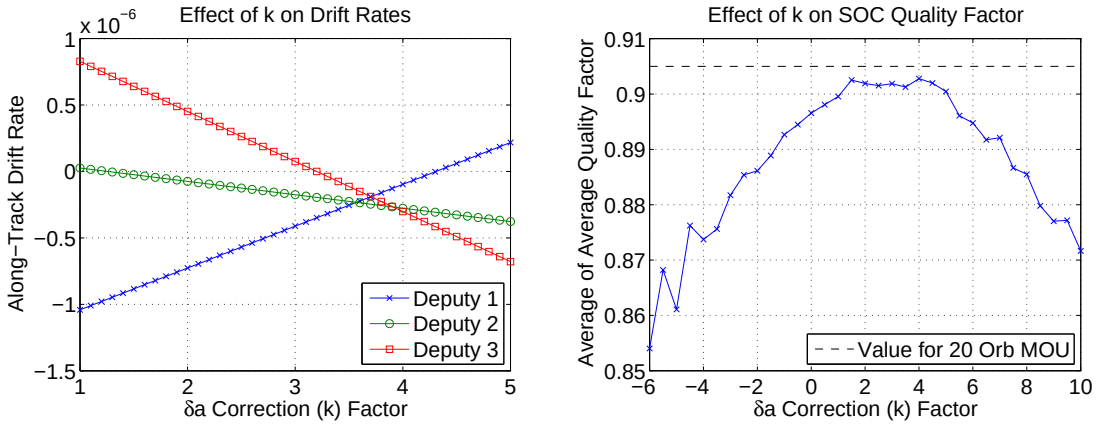

(a) Modified drift rates for 25 km MOU. (b) Average of $\bar{Q}_{\text{RoI}}$ over 10 orbits for SOC.

Figure IV.15. Comparison of effects for Phase II k_j factor.

Table IV.13. k_j values from MOU optimization for Phase II.

	Formation Size (20 orbits)				
	25 km	40 km	60 km	160 km	400 km
k_1	4.31	−0.50	−5.16	3.13	4.20
k_2	1.26	4.09	3.70	2.39	3.41
k_3	3.19	3.62	2.14	2.87	3.75

this case than there was for Phase I, and the slopes of their individual drift rates, from Figure IV.15(a), are quite different. Therefore, we can expect a greater drop in performance than in Phase I if a single k_j value is applied to all three deputies for the SOC optimization method. To see what effect this has, a set of SOC optimizations are performed on the 25 km formation for a range of k_j values, and the resulting average of $\bar{Q}_{\text{RoI}}$ over 10 orbits is plotted in Figure IV.15(b), along with the corresponding value from the 20 orbit MOU optimization. From these results, it seems that the best performance is obtained for k_j values in a broad range between 1.5 and 4.5. $\bar{Q}_{\text{RoI}}$ evolution for the SOC optimization with $k_j = 4$ is shown in Figure IV.16; comparing to Figure IV.13 (noting the difference in location of the peak $\bar{Q}_{\text{RoI}}$), there is a slight loss in QF but the computation cost is much less using the SOC method, as expected.

IV.D.3. Performance in the Presence of Errors

The results of performing Monte Carlo analyses on the 20 orbit MOU optimized formations are summarized in Table IV.14. Each set of results was obtained by sampling a $3\sigma = 100$ m normal distribution for the δa error of each deputy and running 5000 simulations to calculate the T distribution. Similarly to Section IV.C.3, T is taken to be the number of orbits (1 orbit ≈ 2.8 days) that a formation satisfies

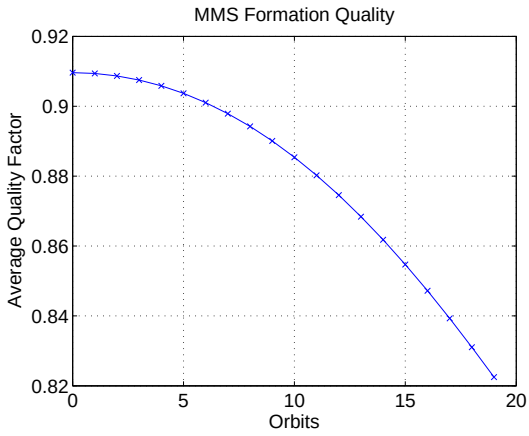

Figure IV.16. Average QF per RoI pass for 25 km Phase II SOC (with $k_j = 4$) optimization.

the MMS mission requirements ($\bar{Q}_{\text{RoI}} \geq 0.78$ and $d_{\min} > 6$ km). As before, it is desired that the formation has a high mean T and a high probability that T will be greater than 5 orbits (≈ 14 days). quantities listed are the minimum $T_{\min}$, maximum $T_{\max}$, mean $\bar{T}$ time to $\bar{Q}_{\text{RoI}} < 0.78$, and the probability that T is less than or equal to 5 orbits, $P_T\,(T \leq 5)$.

Histograms of the results for all but the 400 km formation are shown in Figures IV.17(a)–(d). The performance of all the formations is quite good in the presence of errors: none have any results with $T < 5$ orbits and all of the T histograms are biased towards the higher end of the distribution (longer formation lifetimes). It

Table IV.14. Monte Carlo results for 20 orbit MOU optimizations.

Formation Size	$T_{\min}$	$T_{\max}$	T	$P_T\,(T \leq 5)$
25 km	14	43	35.4	0
40 km	11	43	37.9	0
60 km	19	43	37.7	0
160 km	22	41	38.3	0
400 km	41	42	41.9	0

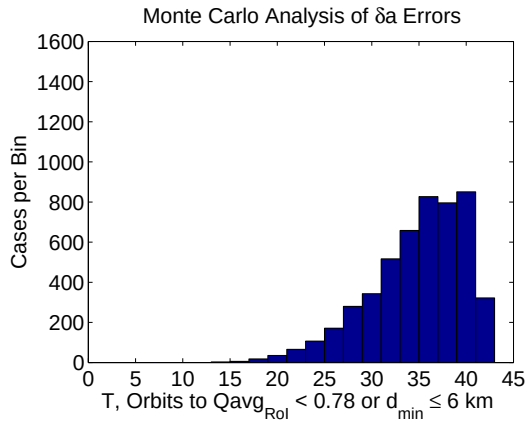

(a) 25 km formation.

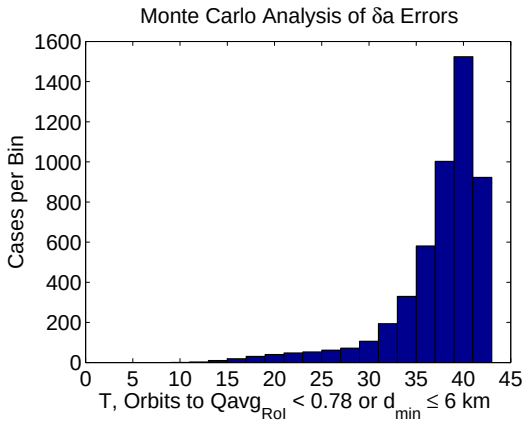

(b) 40 km formation.

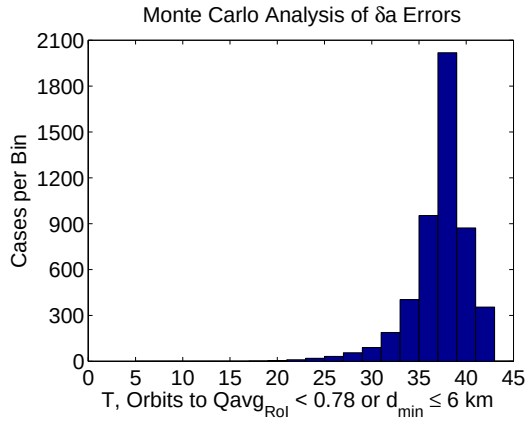

(c) 60 km formation.

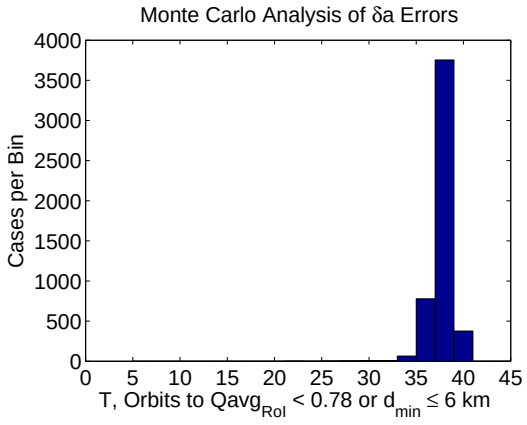

(d) 160 km formation.

Figure IV.17. Effect of $3\sigma = 100$ m δa errors in each deputy on 20 orbit MOU optimizations.

would appear that the Phase II formations are much less sensitive to errors than were the Phase I formations described in Section IV.C when considering δa errors on the same order of magnitude. Therefore, no robust optimization is necessary to improve the performance of these formation designs in the presence of the errors considered in Phase II.

IV.D.4. GMAT Verification

The instantaneous QF and $\bar{Q}_{\mathrm{RoI}}$ predicted by the G-A STM are compared to the GMAT results in Figure IV.18 for the 25 km formation. In this case, the accuracy of the G-A STM is reasonable for almost the entire simulation time, differing from the GMAT result by about 0.05 in $\bar{Q}_{\mathrm{RoI}}$ after 30 orbits. Similarly, the evolution of the tetrahedron side lengths computed by GMAT for this formation is shown in Figure IV.19; comparing to Figure IV.14, there is more variation apparent in the behavior of the side lengths in later orbits in the GMAT simulations due to higher-order gravity and lunisolar perturbation effects, but there is no discernible difference in the minimum side lengths over the time period considered here.

A comparison of the $\bar{Q}_{\mathrm{RoI}}$ results for all of the Phase II formation sizes is shown in Figure IV.20. Here, there is very little difference in the G-A STM and GMAT results for all but the 60 km and 160 km formations, which differ by about 0.04 after 20 orbits. As noted in Section IV.D.1, those formation sizes are more sensitive to

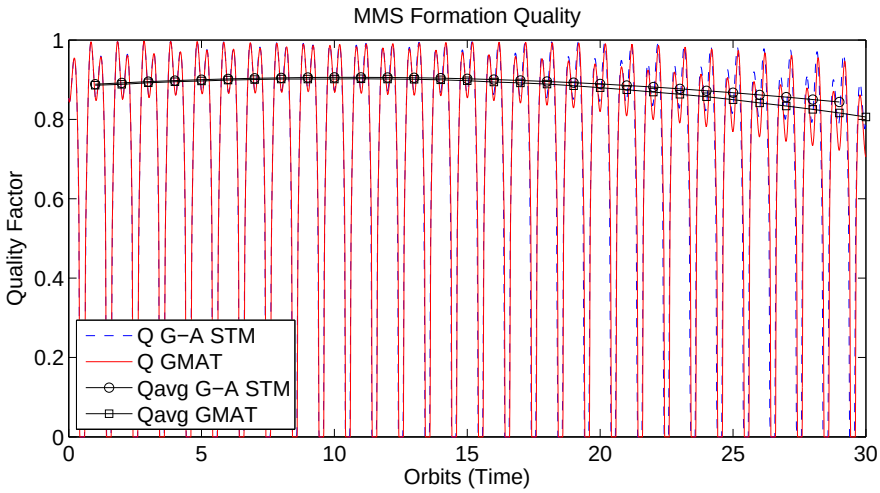

Figure IV.18. Instantaneous QF prediction compared to GMAT for Phase II.

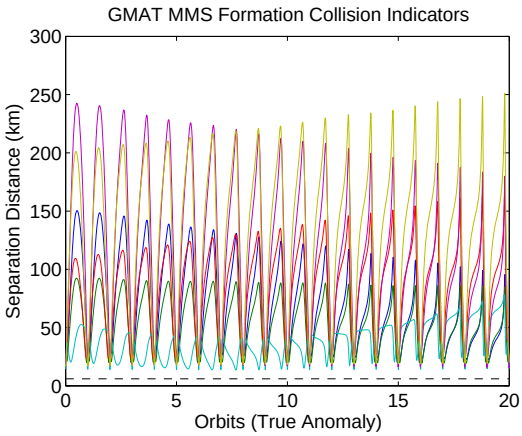

Figure IV.19. GMAT Collision indicators for 25 km Phase II MOU optimization.

changes in satellite separation distances in Phase II because of the relative spacing of the Q_s side length parameters.

Table IV.15 lists results for the GMAT Monte Carlo simulations of the 20 orbit MOU optimized formations (except the 40 km size), using 1000 cases for each, and Figures IV.21(a)–(c) show the corresponding histograms. Comparing these results with those of Table IV.14 and Figures IV.17(a)–(d), it is clear that the GMAT results

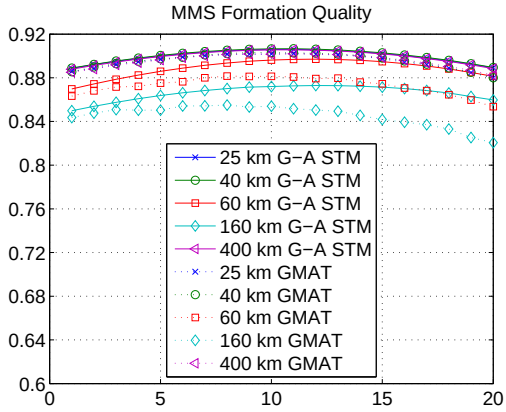

Figure IV.20. Average QF prediction compared to GMAT for Phase II.

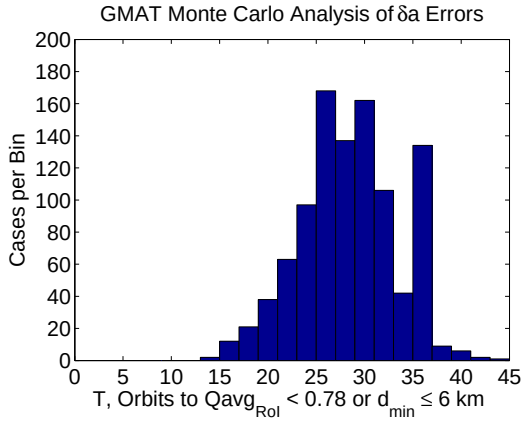

(a) 25 km formation.

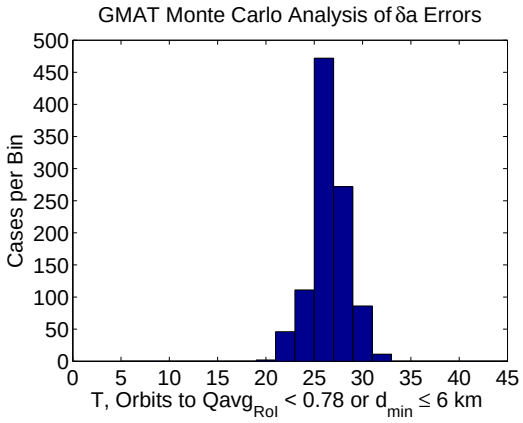

(b) 60 km formation.

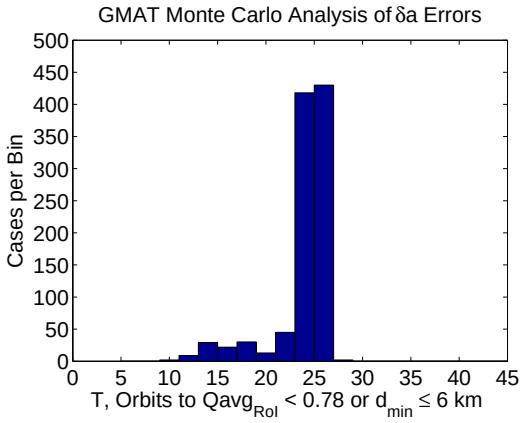

(c) 160 km formation.

Figure IV.21. Effect of $3\sigma = 100$ m δa errors in each deputy on 20 orbit MOU optimizations.

generally predict a shorter formation lifetime than do the G-A STM ones; a similar result was observed in Section IV.C.5, but the difference is greater for Phase II because of the significantly longer orbit period and more pronounced perturbation effects. Once again, the 60 km and 160 km formation results exhibit slightly poorer performance because of their sensitivity to changes in satellite separation distances in Phase II due to the relative spacing of the Q_s side length parameters.

Table IV.15. GMAT Monte Carlo results for 20 orbit MOU optimizations.

Formation Size	$T_{\min}$	$T_{\max}$	T	$P_T\,(T \leq 5)$
25 km	14	44	28.9	0
60 km	21	32	27.0	0
160 km	10	28	24.5	0
400 km	28	34	31.5	0

IV.E. Physical Significance

In this section the physics of the MMS formation design results are examined, including the geometric effects of the robust optimization. Figure IV.22 shows the apogee formation geometry (in the LVLH frame) resulting from several different design methods. Each design method is examined during the orbit of the peak average QF (as previously mentioned, most multi-orbit designs do not have their maximum $\bar{Q}_{\text{RoI}}$ in the first orbit). In each case, three of the satellites are roughly

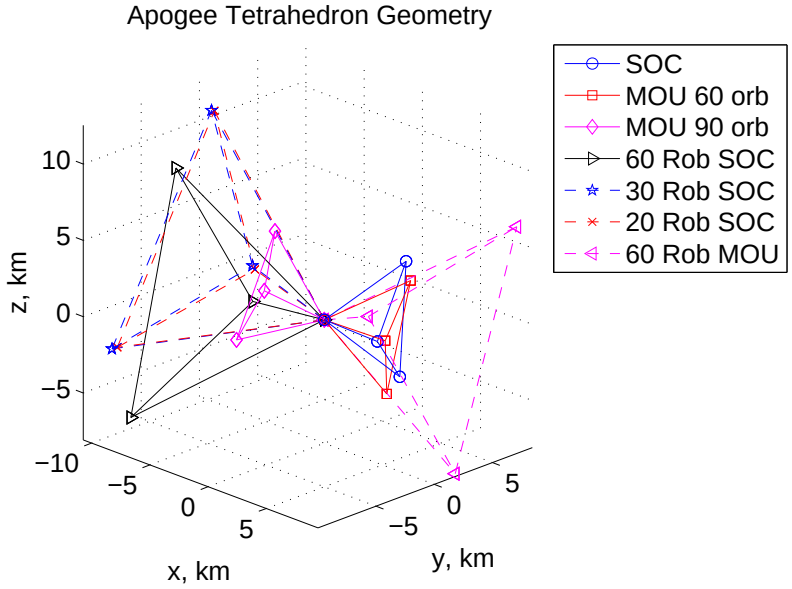

Figure IV.22. 10 km formation configuration at apogee.

in the plane of the reference orbit, forming the base of the tetrahedron, and the fourth is out of the plane. The out-of-plane deputy's displacement is created by a combination of both differential inclination and right ascension. In all of the designs, especially the longer-term ones (larger N_{orb} in the optimizations), the bases of the tetrahedra are not quite aligned with the plane of the reference orbit; this is caused by long-term secular effects due to J_2 (since later orbits are being observed in these cases).

It is interesting that the robust optimizations produced larger overall formations (about 14 km at apogee) than did the non-robust SOC or MOU optimizations even though no minimum separation constraint was imposed in the design process. The increase in size could be due to the definition of Q_v, Eq. (4.5): since $\bar{L}$ appears in the denominator, increasing the overall formation size makes Q_v less sensitive to a given δa error magnitude. The larger size also results in larger values of the nominal δa: about 40–50 m for the 10 km robust formation, according to Table IV.8, compared to about 10–30 m for the nominal results, listed in Tables IV.2 and IV.4.

To better understand the geometries of the optimal tetrahedra and to investigate possible symmetries in the solutions, 500 random initial formations were generated (by choosing 500 random values of the tetrahedron orientation angles, ϕ, ψ, and γ, defined in Eq. (3.12)) and optimized using the 60 orbit MOU method. The nominal formation lifetimes were measured and, aside from a few small clusters of lower values, were found to range from 90–95 days with a mode of 94. The geometries of the best formations, with lifetimes of 95 days, were examined and from these results were identified 8 possible optimal tetrahedron orientations, which are shown

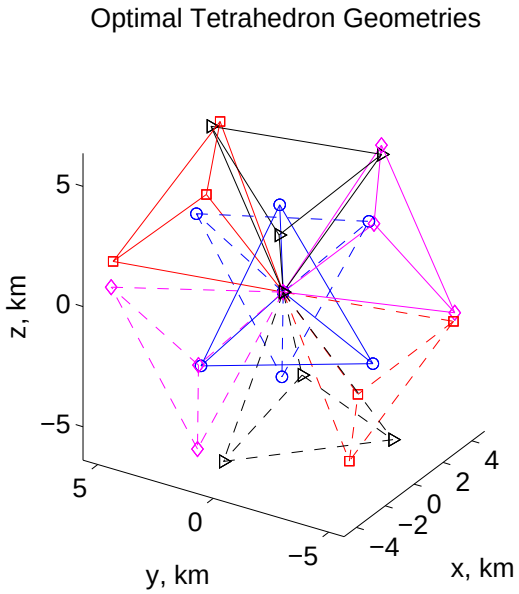

Figure IV.23. Possible optimal formation configurations (10 km).

in Figure IV.23 (the 4 solid tetrahedra are above the orbit plane and the 4 dashed tetrahedra are below the orbit plane). In fact, these can really be considered 2 possible orientations, in which the chief satellite can be placed at any of the 4 vertices to give a total of 8 configurations. Each of the tetrahedra has a "base" which lies roughly in the plane of the reference orbit and one satellite is out of the plane. Pairs of orientations do not have a plane of symmetry, but they are related by a 180° rotation about a line in the x-y plane, parallel to the side of the base furthest from the origin, as shown in Figure IV.24. In each case, the base is slightly inclined with respect to the reference orbit, most likely to account for J_2 which will cause it to precess over the course of the mission.

Figures IV.25(a)–(e) illustrate how the tetrahedron evolves throughout the RoI and Figure IV.25(f) shows the formation at perigee. Projected onto the orbit plane, the motion of the deputies is roughly elliptical, each with its own phase. As a

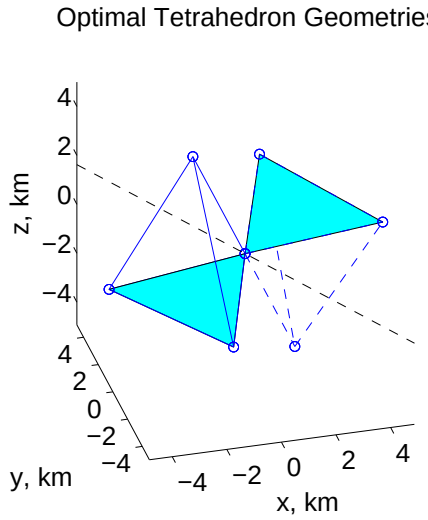

Figure IV.24. Pair of optimal formation configurations (10 km).

whole, the tetrahedron slowly revolves about the z-axis, contracting and growing taller until it reaches apogee, then expanding symmetrically. The formation forms a regular tetrahedron at two points, in Figures IV.25(b) and (d), which correspond to the peaks of the QF (shown in Figure IV.26(a)). Outside the RoI, the tetrahedron continues to revolve but distorts as it nears perigee; the deputy with the large out-of-plane displacement crosses briefly through the base of the tetrahedron as the formation passes through this point.

Figures IV.26(a) and (b) show the QF and average QF for several different formation design methods. Figure IV.26(a) shows the instantaneous QF over the orbit corresponding to the maximum $\bar{Q}_{\mathrm{RoI}}$ for each case, and the vertical lines indicate the location of the RoI. The main distinguishing characteristic of the robust optimized results is that they produce a narrower peak in the QF curve than do the other optimizations. The times of Figures IV.25(a)–(e) refer to, respectively, the beginning of the RoI, the first peak of the QF, apogee, the second peak of the QF, and the end of

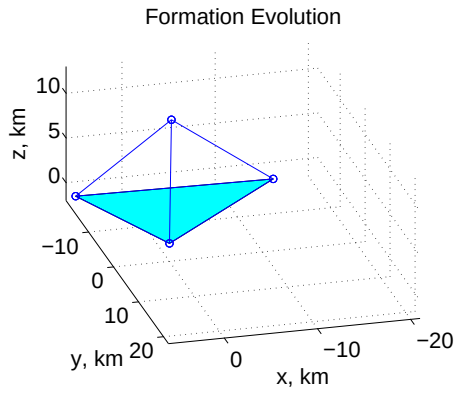

(a) $f = 160°$, $t = 0.23T$.

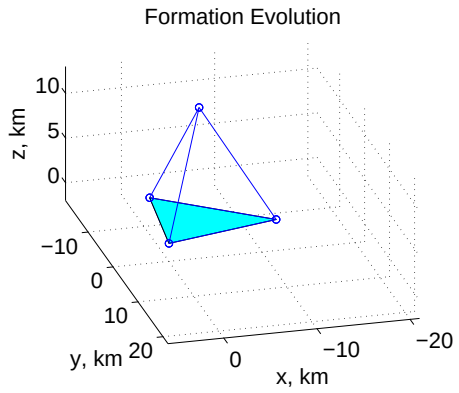

(b) $f = 171°$, $t = 0.36T$.

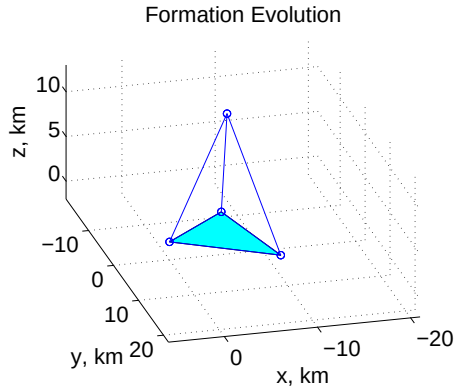

(c) $f = 180°$, $t = 0.5T$.

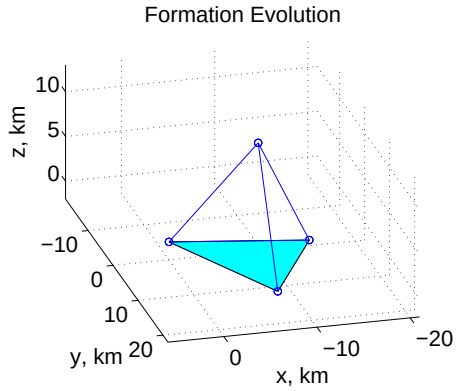

(d) $f = 190°$, $t = 0.66T$.

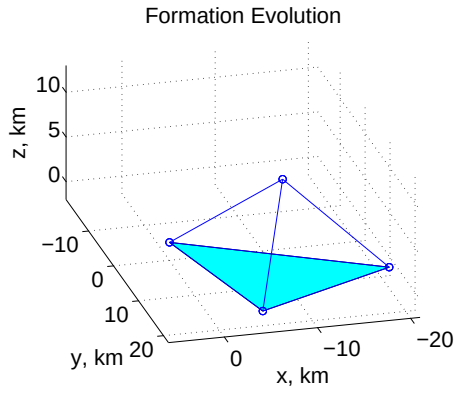

(e) $f = 200°$, $t = 0.77T$.

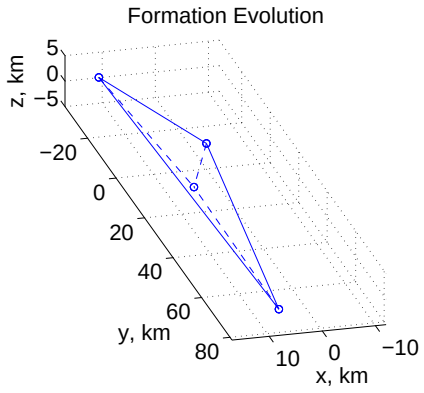

(f) $f = 360°$, $t = T$.

Figure IV.25. Evolution of 30 orbit robust 10 km MMS formation.

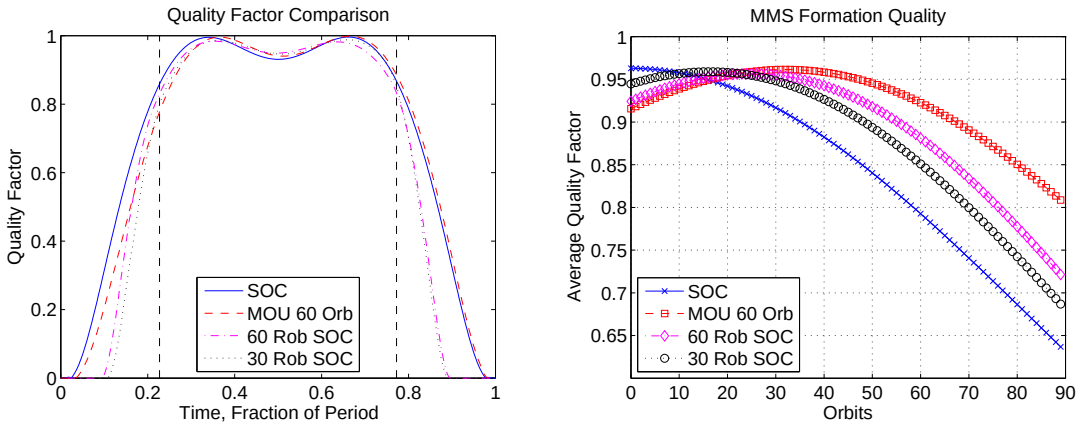

(a) Quality factor. **(b) Average quality factor.**

Figure IV.26. Comparison of robust and nominal QF performance.

the RoI. Figures IV.26(b) shows that the average QFs for the robust optimizations do not quite reach the maxima of either the SOC or 60 orbit MOU optimizations, and they fall off more steeply as well, illustrating the fact that some performance has been sacrificed in the error-free case to gain a more robust formation design.

Some investigation was also undertaken to attempt to determine what characteristics made certain formations more or less susceptible to close approaches in the presence of maneuver/navigation errors. Close approaches are a practical concern for missions like MMS because they can require emergency maneuvers to be carried out in order to keep the satellites apart. As mentioned in Chapter I, D'Amico and Montenbruck [75] in 2006 introduced a strategy for passive close approach avoidance of a pair of formation flying satellites using eccentricity/inclination (E/I) vector separation. This formulation, valid for circular orbits only, mitigates collision hazards in the presence of along-track uncertainty by aligning the relative E/I vectors in a parallel (or anti-parallel) configuration. This is equivalent to ensuring that the deputy's

along-track motion is out of phase with both its radial and out-of-plane motions, which maximizes separation in one direction when the deputy crosses a node in another. In the case of a circular reference orbit, the relative motion of a deputy is described by coupled harmonic oscillators. It is challenging to expand the theory of E/I vector separation to the case of highly eccentric orbits, however, because of the more complex motion that occurs. Furthermore, in MMS there are four satellites to deal with, any pair of which could experience a close approach.

Some additional insight can be gained by analyzing the actual trajectories of the deputies in the LVLH plane for different formation designs. Figure IV.27 shows the evolution of a formation which has good $\bar{T}$ properties but a high incidence of close approaches in the presence of δa errors. Figure IV.28 shows the evolution of a formation which experiences very few close approaches with slightly lower $\bar{T}$. In both cases, the circled points indicate the formation configuration at apogee. Note that in the maximum $\bar{T}$ case the motion evolves as described in previous paragraphs: two deputies roughly in the x-y plane and one out of the plane. In the minimum close approach case this situation is reversed.

Figures IV.29 and IV.30 show the same two formation designs, this time with all four satellites' trajectories plotted about the formation center. From Figure IV.29 it is clear that in the max $\bar{T}$ case there are three satellites which have very little separation in the z direction, and especially in the x-z plane, throughout the orbit. Therefore, if there is uncertainty in the along-track direction there is a high probability of close approaches amongst these three satellites at points in the orbit where their radial separation is also small. Figure IV.30 shows that in the min close

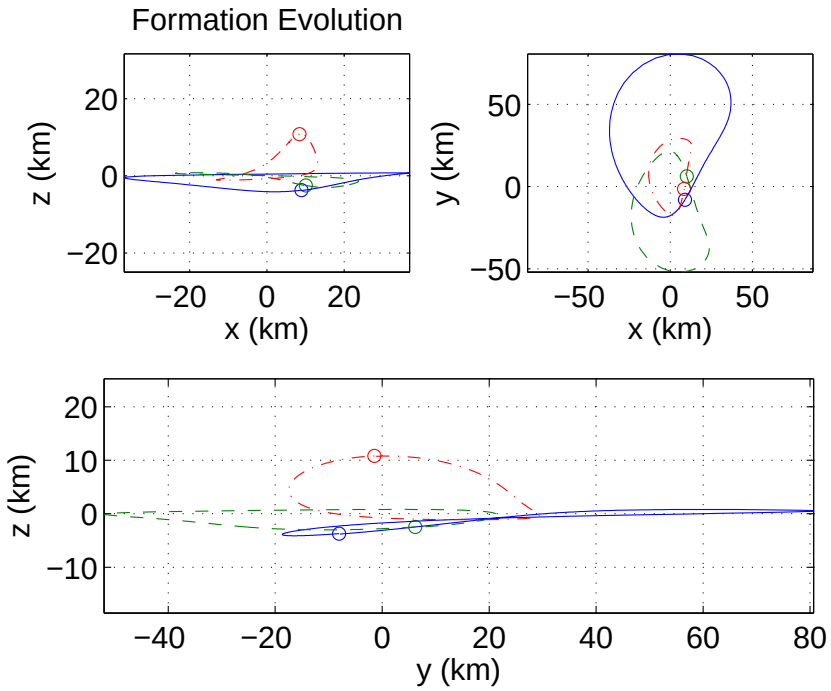

Figure IV.27. LVLH evolution of max $\bar{T}$ case.

approach case all but two of the satellites are well-spaced in the z direction, and those two only come close together near apogee with their motion otherwise out of phase in the x-z plane. As noted previously, uncertainty of δa affects primarily the y direction, so to mitigate close approach occurrences the separation in the x-z plane should be maximized.

Certain general solutions for periodic relative motion near elliptic orbits, analogous to the periodic solutions of the Hill-Clohessy-Wiltshire (HCW) equations for circular orbits, were classified in 2007 by Sengupta and Vadali [26] based on the

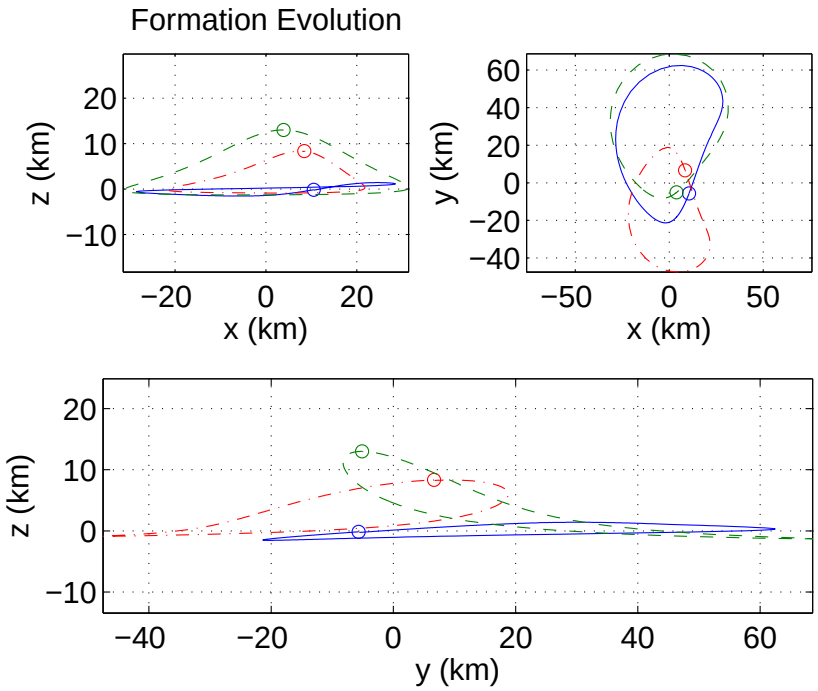

Figure IV.28. LVLH evolution of min close approach case.

Tschauner-Hempel (TH) equations:

$$\frac{x}{R} = \frac{\rho_1}{p}\sin(f+\alpha_0)(1+e\cos f) \tag{4.18}$$

$$\frac{y}{R} = \frac{\rho_1}{p}\cos(f+\alpha_0)(2+e\cos f) + \frac{\rho_2}{p} \tag{4.19}$$

$$\frac{z}{R} = \frac{\rho_3}{p}\sin(f+\beta_0) \tag{4.20}$$

where ρ_1, ρ_2, and ρ_3 are size parameters and α_0 and β_0 are phase parameters. Comparison with E/I vector separation theory suggests that satellites following these solutions should have x and z motions with opposite phases in order to minimize the risk of close approach; that is, the α_0 and β_0 directions should not be parallel (perpendicular is best). The MMS satellites do not follow these solutions exactly, but if they are assumed to do so (or at least are close) then α_0 and β_0 values for each pair of satellites can be extracted from the initial conditions. The differences between

these values are shown in Table IV.16 for the two formations, with values shown in bold indicating pairs in which α_0 and β_0 are nearly parallel. The fact that the max $\bar{T}$ case has two pairs nearly parallel while the min close approach case has only one supports this analysis and the hypothesis that separation in the x-z plane may be the key to passive collision avoidance for formations in highly eccentric orbits.

Table IV.16. α_0 and β_0 differences for pairs of satellites.

Formation	$\lvert\alpha_0 - \beta_0\rvert$ (deg)					
max T	49	241	**2**	38	**178**	165
min CI	70	10	**176**	30	195	18

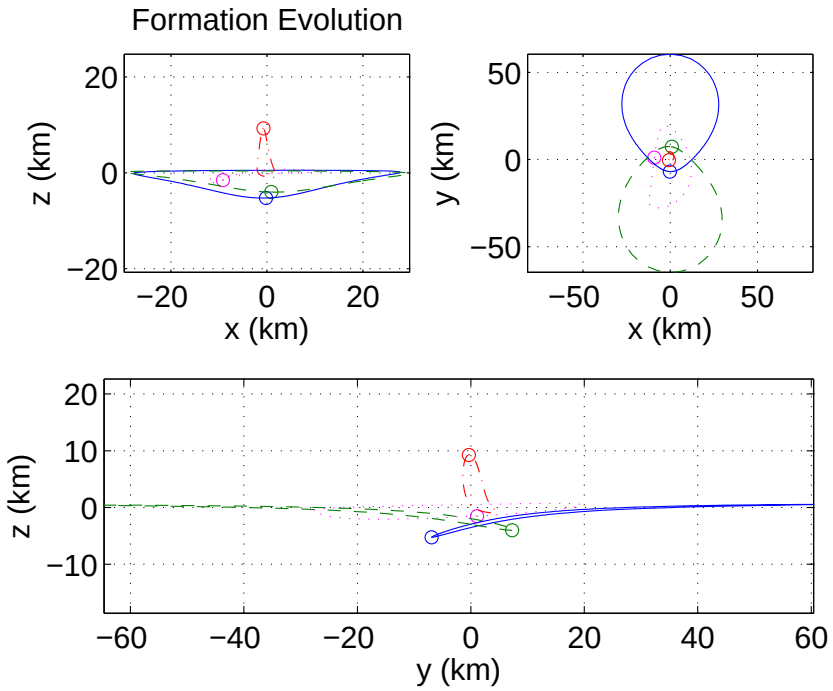

Figure IV.29. LVLH evolution of max $\bar{T}$ case about formation center.

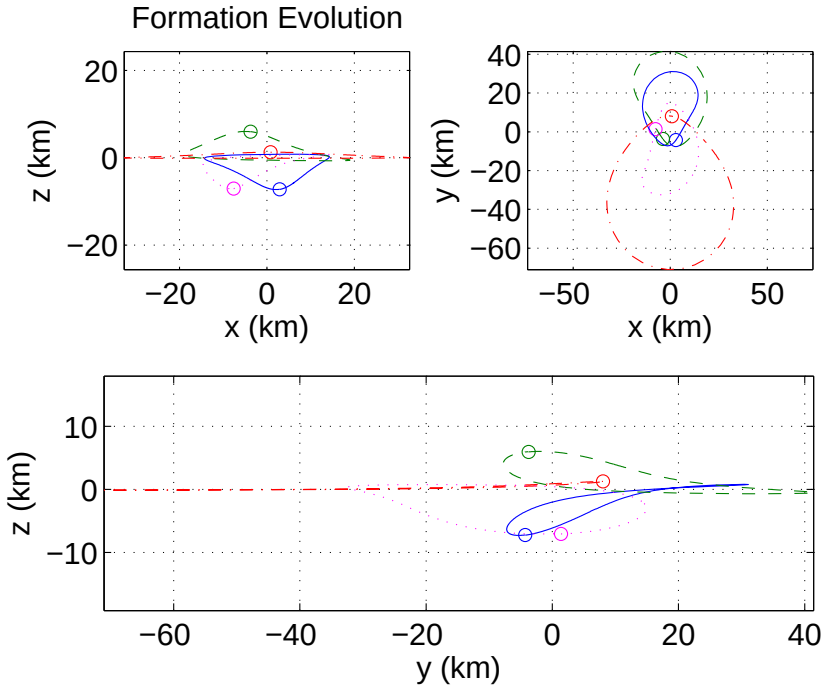

Figure IV.30. LVLH evolution of min close approach case about formation center.

CHAPTER V

THIRD-BODY PERTURBATIONS*

In this chapter, the effects of third-body perturbations on satellite formations are investigated using differential orbital elements to describe the relative motion. Absolute and differential effects of the lunar perturbation on satellite formations are derived analytically based on the simplified model of the circular restricted three-body problem, initially following a similar approach to that of Prado [55], but the method can readily be applied to the solar perturbation as well. This analytical description includes averaged long-term effects on the orbital elements, including the full transformation between the osculating elements and the lunar-averaged elements, which is absent from previous research. Without this transformation, the method of averaging produces inaccurate results over time due to the effect of discrepancies in initial conditions.

A simplified Earth-Moon system model is used, but the results are applicable to any formation reference orbit about the Earth. Simulations are performed to determine the effects of the lunar perturbation on example formations in upper MEO, highly eccentric orbits by using the formation design criteria of Phases I and II of the NASA Magnetospheric Multiscale (MMS) mission. The changes in angular differential orbital elements ($\delta\omega$, $\delta\Omega$, and δM_0) and in science return quality due to this perturbation are compared to changes due to J_2. The method is then expanded

*Part of this chapter is reprinted with permission from "Third-Body Perturbation Effects on Satellite Formations" by Roscoe, C. W. T., Vadali, S. R., and Alfriend, K. T., 2012, *AAS Jer-Nan Juang Astrodynamics Symposium*. Copyright 2012 by the American Astronautical Society.

to include the inclination of the Moon's orbit with respect to the ecliptic plane and results are compared to simulation using the NASA General Mission Analysis Tool (GMAT).

V.A. Averaged Lunar Disturbing Potential

The general third-body disturbing potential acting on a satellite in Earth orbit was described in Section II.B.2. Restricting attention in this chapter to the lunar perturbation and assuming that the satellite is much closer to the Earth than to the Moon, the disturbing potential can be written in the form of Eq. (2.34):

$$R_{\text{lun}} = \frac{1}{2}\frac{\mu' n'^2 a'^3}{R'}\left(\frac{R}{R'}\right)^2 \left(3\cos^2 S - 1\right) \tag{5.1}$$

where only the $k = 2$ term has been retained. As in Section II.B.2, if the Moon's orbit is further assumed to be in a circular, equatorial orbit about the Earth the $\cos S$ term can be written in the form of either Eq. (2.35) or (2.36).

There are three distinct time scales in the problem as defined. First, the period of the satellites is the shortest, over which time the variables exhibit short-period oscillations (for MMS Phase I, $T \approx 1$ day with $a \approx 4 \times 10^4$ km; for Phase II, $T \approx 3$ days with $a \approx 8 \times 10^4$ km). Second, over the period of the Moon (27 days) the variables exhibit medium-period oscillations. Finally, there are long-term variations in the variables, which are either non-periodic or have periods of several years.

The method presented by Prado [55] begins by first averaging Eq. (5.1) over one satellite period to remove the short-period oscillations:

$$\langle R_{\text{lun}} \rangle \triangleq \frac{1}{2\pi}\int_0^{2\pi} R_{\text{lun}}\, dM \tag{5.2}$$

This can also be done to the non-simplified model, and is in fact the same procedure that is followed in the earlier lunar perturbation analyses [50–54]. Second, the single-averaged disturbing potential is averaged again, this time over the Moon's period:

$$\langle\langle R_{\text{lun}}\rangle\rangle \triangleq \frac{1}{2\pi}\int_0^{2\pi} \langle R_{\text{lun}}\rangle \; dM' \tag{5.3}$$

This removes the medium-period oscillations as well as any dependence on the actual position of the Moon, which is very useful for simulation.

In Prado [55], summation terms in the disturbance potential, Eq. (2.32), are retained up to $k = 4$; however, in this analysis only $k = 2$ terms are retained (note that the double-averaged $k = 3$ terms are zero). The resulting second-order, double-averaged disturbing potential is [55]

$$\langle\langle R_{\text{lun}}\rangle\rangle = \frac{\mu' a^2 n'^2}{16}\left[\left(2+3e^2\right)\left(3\cos^2 i - 1\right) + 15e^2 \sin^2 i \cos 2\omega\right] \tag{5.4}$$

V.A.1. Absolute and Differential Rates

The independent variables used to describe the satellites' motion in this chapter are the classical orbital elements $(a, e, i, \Omega, \omega, M_0)$ and their differences. Given a general disturbing potential R_{dis}, the time derivatives of the classical orbital elements can be computed using Lagrange's planetary equations [82],

$$\dot{a} = \frac{2}{na}\frac{\partial R_{\text{dis}}}{\partial M_0} \tag{5.5}$$

$$\dot{e} = -\frac{b}{na^3 e}\frac{\partial R_{\text{dis}}}{\partial \omega} + \frac{b^2}{na^4 e}\frac{\partial R_{\text{dis}}}{\partial M_0} \tag{5.6}$$

$$\dot{i} = -\frac{1}{nab\sin i}\frac{\partial R_{\text{dis}}}{\partial \Omega} + \frac{\cos i}{nab\sin i}\frac{\partial R_{\text{dis}}}{\partial \omega} \tag{5.7}$$

$$\dot{\Omega} = \frac{1}{nab\sin i}\frac{\partial R_{\text{dis}}}{\partial i} \tag{5.8}$$

$$\dot{\omega} = -\frac{\cos i}{nab\sin i}\frac{\partial R_{\rm dis}}{\partial i} + \frac{b}{na^3 e}\frac{\partial R_{\rm dis}}{\partial e} \tag{5.9}$$

$$\dot{M}_0 = -\frac{2}{na}\frac{\partial R_{\rm dis}}{\partial a} - \frac{b^2}{na^4 e}\frac{\partial R_{\rm dis}}{\partial e} \tag{5.10}$$

By substituting Eq. (5.4) into Lagrange's planetary equations, the rates of change of the classical orbital elements due to the averaged lunar disturbing potential are obtained (as in Ref. 55):

$$\dot{a} = 0 \tag{5.11}$$

$$\dot{e} = \frac{15\mu' n'^2 e\eta}{8n}\sin^2 i \sin 2\omega \tag{5.12}$$

$$\dot{i} = -\frac{15\mu' n'^2 e^2}{16n\eta}\sin 2i \sin 2\omega \tag{5.13}$$

$$\dot{\Omega} = \frac{3\mu' n'^2 \cos i}{8n\eta}\left(5e^2\cos 2\omega - 3e^2 - 2\right) \tag{5.14}$$

$$\dot{\omega} = \frac{3\mu' n'^2}{8n\eta}\left[5\cos^2 i - \eta^2 + 5\left(\eta^2 - \cos^2 i\right)\cos 2\omega\right] \tag{5.15}$$

$$\dot{M}_0 = -\frac{\mu' n'^2}{8n}\left[\left(3e^2+7\right)\left(3\cos^2 i - 1\right) + 15\left(1+e^2\right)\sin^2 i\cos^2\omega\right] \tag{5.16}$$

The rates of the differential orbital elements can then be found by taking the first variation of the rates of the absolute elements,

$$\delta\dot{a} = 0 \tag{5.17}$$

$$\begin{aligned}\delta\dot{e} = \frac{15\mu' n'^2}{8n}\Bigg[&\frac{3e\eta}{2a}\sin^2 i\sin 2\omega\ \delta a + \frac{1}{\eta}\left(1-2e^2\right)\sin^2 i\sin 2\omega\ \delta e \\ &+\ e\eta\sin 2i\sin 2\omega\ \delta i + 2e\eta\sin^2 i\cos 2\omega\ \delta\omega\Bigg]\end{aligned} \tag{5.18}$$

$$\begin{aligned}\delta\dot{i} = -\frac{15\mu' n'^2}{16n}\Bigg[&\frac{3e^2}{2a\eta}\sin 2i\sin 2\omega\ \delta a + \left(\frac{2e}{\eta} + \frac{e^3}{\eta^3}\right)\sin 2i\sin 2\omega\ \delta e \\ &+\ \frac{2e^2}{\eta}\cos 2i\sin 2\omega\ \delta i + \frac{2e^2}{\eta}\sin 2i\cos 2\omega\ \delta\omega\Bigg]\end{aligned} \tag{5.19}$$

$$
\begin{aligned}
\delta\dot{\Omega} = \frac{3\mu' n'^2}{8n} \Bigg\{ & \frac{3\cos i}{2a\eta} \left(5e^2 \cos 2\omega - 3e^2 - 2\right) \delta a \\
& + \frac{e\cos i}{\eta^3} \left[\left(5e^2 \cos 2\omega - 3e^2 - 2\right) + 2\eta^2 \left(5\cos 2\omega - 3\right) \right] \delta e \\
& - \frac{\sin i}{\eta} \left(5e^2 \cos 2\omega - 3e^2 - 2\right) \delta i - \frac{10e^2}{\eta} \cos i \sin 2\omega \ \delta\omega \Bigg\}
\end{aligned} \tag{5.20}
$$

$$
\begin{aligned}
\delta\dot{\omega} = \frac{3\mu' n'^2}{8n\eta^3} \Bigg\{ & \frac{3\eta^2}{2a} \left[\left(5\cos^2 i - \eta^2\right) + 5\left(\eta^2 - \cos^2 i\right) \cos 2\omega \right] \delta a \\
& + \ e \left[5\cos^2 i - 5\left(\eta^2 + \cos^2 i\right) \cos 2\omega + \eta^2 \right] \delta e \\
& - \ 5\eta^2 \sin 2i \left(1 - \cos 2\omega\right) \delta i - 10\eta^2 \left(\eta^2 - \cos^2 i\right) \sin 2\omega \ \delta\omega \Bigg\}
\end{aligned} \tag{5.21}
$$

$$
\begin{aligned}
\delta\dot{M}_0 = & -\frac{\mu' n'^2}{8n} \Bigg\{ \frac{3}{2a} \left[\left(3e^2 + 7\right) \left(3\cos^2 i - 1\right) + 15\left(1 + e^2\right) \sin^2 i \cos^2 \omega \right] \delta a \\
& + \ 6e \left(3\cos^2 i - 1 + 5\sin^2 i \cos^2 \omega\right) \delta e \\
& - 3\sin 2i \left[3e^2 + 7 - 5\left(1 + e^2\right) \cos^2 \omega \right] \delta i \\
& - 15\left(1 + e^2\right) \sin^2 i \sin 2\omega \ \delta\omega \Bigg\}
\end{aligned} \tag{5.22}
$$

V.B. Canonical Transformation

Eqs. (5.11)–(5.16) and (5.17)–(5.22) are the rates of change of the absolute and differential classical orbital elements, respectively, due to the doubly-averaged lunar perturbation. However, because the disturbing potential has been averaged, these now represent the rates of a new set of "lunar"-averaged orbital elements rather than the instantaneous osculating elements. If Eqs. (5.11)–(5.16) and (5.17)–(5.22) were applied without correcting the initial conditions for this difference the results would become increasingly inaccurate as the equations are propagated forward in time. This concept is exactly analogous to the difference between the mean orbital elements and the osculating orbital elements in Brouwer's near-Earth satellite theory [49].

To obtain the transformation between the lunar elements and the osculating elements the problem is rewritten in Hamiltonian canonical form using the Delaunay variables,

$$\begin{aligned} l &= M & L &= \sqrt{\mu a} \\ g &= \omega & G &= L\eta \\ h &= \Omega & H &= G\cos i \end{aligned} \tag{5.23}$$

or, in vector-matrix form, $\mathbf{x} = \left[\ l\ g\ h\ \right]^T$ and $\mathbf{X} = \left[\ L\ G\ H\ \right]^T$. Defining the small quantity $\varepsilon = \left(a_0/a_0'\right)^2$, where $(\cdot)_0$ indicates a constant quantity (either the initial or averaged value, defined this way so that ε is a constant), the Hamiltonian corresponding to the gravitational potential

$$V = -\frac{\mu}{r} - \frac{1}{2}\frac{\mu' n'^2 a'^3}{R'}\left(\frac{R}{R'}\right)^2\left(3\cos^2 S - 1\right) \tag{5.24}$$

can be written as

$$\mathcal{H} = \mathcal{T} + V = \mathcal{H}_0 + \varepsilon\mathcal{H}_1 \tag{5.25}$$

where $\mathcal{T} = \frac{1}{2}v^2$ is the kinetic energy (with v being the orbit speed), $\mathcal{H}_0$ is the two-body Hamiltonian and $\mathcal{H}_1$ is the first term of the disturbing potential (the $k = 2$ term), normalized by ε. Treating this as a Lie series in ε, the two averagings of Prado [55] can be performed as near-identity canonical transformations.

A dynamic system with variables $(\mathbf{x}, \mathbf{X})$ and Hamiltonian $\mathcal{H}(\mathbf{x}, \mathbf{X}, t)$ is said to be in canonical form if it satisfies the canonical equations of Hamilton [90]

$$\dot{\mathbf{x}} = \frac{\partial\mathcal{H}}{\partial\mathbf{X}} \qquad\qquad \dot{\mathbf{X}} = -\frac{\partial\mathcal{H}}{\partial\mathbf{x}} \tag{5.26}$$

In such a case, $(\mathbf{x}, \mathbf{X})$ are also said to be canonical variables, with $\mathbf{x}$ called the generalized coordinates and $\mathbf{X}$ called the conjugate momenta. With a system in

canonical form, it is often simple to visualize how the motion will evolve by examining the form of the Hamiltonian. For example, if one of the individual momenta, L, G, or H, does not appear explicitly in the Hamiltonian, the associated coordinate, l, g, or h, will be constant. (Variables which do not appear explicitly in the Hamiltonian are called "cyclic.")

A transformation of the system from the variables $(\mathbf{x}, \mathbf{X})$ to a new set of variables $(\mathbf{y}, \mathbf{Y})$ is said to be canonical if Hamilton's equations are still valid in the new variables: that is, if it preserves the canonical form of the system for some new Hamiltonian $\mathcal{K}(\mathbf{y}, \mathbf{Y}, t)$. Canonical transformations are useful for taking systems in which all or many of the variables are time-varying and converting them into equivalent systems in which several of the variables are cyclic. If such a transformation exists for a given system, it can be defined through a special function W, called the generating function. W is not unique for a given transformation and can be expressed as a function of several different combinations of the old and new variables; however, once it has been found its derivatives yield all of the relationships between the old and new variables and Hamiltonians.

Perturbation theory—which deals with problems where the Hamiltonian is made up of a main term and small disturbance terms—makes use of near-identity canonical transformations, in which the variables and Hamiltonian are only slightly modified by the transformation. The method of averaging, which is used in the present chapter, seeks to remove small oscillations in the variables due to perturbations, leaving only long-term effects, by replacing the Hamiltonian with a new function made up of the same main term and averaged forms of the disturbance terms. The new variables

will obviously be different from the old ones, but if the disturbances terms are small they will be nearly identical.

A procedure for averaging conservative dynamic systems in which the Hamiltonian can be expressed as a power series in a small parameter was proposed by von Zeipel [91] in 1916, and this was the method used by Brouwer [49] to treat the zonal harmonic problem in 1959. The von Zeipel method has a major drawback, however, in that the generating function is derived in mixed old and new variables, which makes it mathematically cumbersome to derive explicit expressions for the required transformations. Instead, the derivation in this section will employ the method of Lie transforms, as defined by Deprit [92], who in 1968 presented an alternate theory for systematically solving problems of this type, in which the generating function is derived purely as a function of the transformed variables. The methods of von Zeipel and Lie transforms were proven to be equivalent in 1970 by Shniad [93].

At this point, it is worth examining how each of the terms in this particular Hamiltonian (Eq. (5.25)) explicitly depends on the variables of the problem. Using the vis-viva integral [82]

$$v^2 = \mu \left(\frac{2}{R} - \frac{1}{a} \right) \tag{5.27}$$

the two-body Hamiltonian $\mathcal{H}_0$ can be written,

$$\mathcal{H}_0 = -\frac{\mu^2}{2L^2} \tag{5.28}$$

which depends only on L. Since the equations of motion in canonical form are given by Eq. (5.26), under purely two-body motion the only variable which changes over

time is the mean anomaly l, as expected. The first-order disturbance term is

$$\mathcal{H}_1 = \frac{\mu' n'^2 a'^3}{2r'} \left(\frac{a_0'}{a_0}\right)^2 \left(\frac{r}{r'}\right)^2 \left[3\left(\alpha\cos f + \beta \sin f\right)^2 - 1\right] \tag{5.29}$$

which depends on all six Delaunay elements through r, f, α, and β. Recall that α and β are defined in Eqs. (2.37) and (2.38), respectively; in terms of Delaunay elements these terms are

$$\alpha = \cos g \cos\left(l' - h\right) + \sin g \sin\left(l' - h\right) \frac{H}{G} \tag{5.30}$$

$$\beta = -\sin g \cos\left(l' - h\right) + \cos g \sin\left(l' - h\right) \frac{H}{G} \tag{5.31}$$

Additionally, $\mathcal{H}_1$ depends on the lunar parameters, most of which are constant under the assumptions of the simplified model. However, the lunar mean anomaly l' varies with a rate of n', which introduces an explicit time dependence in the Hamiltonian. Therefore, the overall Hamiltonian depends explicitly on $\mathbf{x}$, $\mathbf{X}$, and t.

The first near-identity transformations will remove all terms depending on l from the Hamiltonian (up to first order in ε). The transformed Hamiltonian $\mathcal{K}$ has the form

$$\mathcal{K}\left(\mathbf{y}, \mathbf{Y}, t\right) = \underbrace{\mathcal{H}_0\left(\_, \mathbf{Y}, \_\right)}_{\mathcal{K}_0(\_,\mathbf{Y},\_)} + \varepsilon \underbrace{\left\langle \mathcal{H}_1 \right\rangle \left(\mathbf{y}, \mathbf{Y}, t\right)}_{\mathcal{K}_1(\mathbf{y},\mathbf{Y},t)} \tag{5.32}$$

where $\mathbf{y} = \begin{bmatrix} \bar{l} & \bar{g} & \bar{h} \end{bmatrix}^T$ and $\mathbf{Y} = \begin{bmatrix} \bar{L} & \bar{G} & \bar{H} \end{bmatrix}^T$ are the new single-averaged variables and the $(\_)$ notation is used to show those terms which do not depend explicitly on certain variables. Note that the two-body term is unchanged and that $\mathcal{K}_1$ does not depend on $\bar{l}$. At first order, the equations for Lie transforms [92] give the relation

$$\mathcal{K}_1\left(\mathbf{y}, \mathbf{Y}, t\right) = \mathcal{H}_1\left(\mathbf{y}, \mathbf{Y}, t\right) + L_1 \mathcal{H}_0 - \frac{\partial W_1}{\partial t} \tag{5.33}$$

where $L_1\mathcal{H}_0 = (\mathcal{H}_0; W_1)$ is the Lie derivative of $\mathcal{H}_0$ generated by W_1 and $(\cdot;\cdot)$ is the Poisson bracket with respect to the variables of interest, that is

$$(A; B) = \frac{\partial A}{\partial \mathbf{y}}\frac{\partial B}{\partial \mathbf{Y}} - \frac{\partial A}{\partial \mathbf{Y}}\frac{\partial B}{\partial \mathbf{y}} \tag{5.34}$$

W_1 is the first-order generating function for the canonical transformation. Once $W_1(\mathbf{y}, \mathbf{Y}, t)$ is determined, the transformation between the single-averaged and osculating variables is given by

$$\mathbf{x} = \mathbf{y} + \varepsilon\frac{\partial W_1}{\partial \mathbf{Y}} \qquad\qquad \mathbf{X} = \mathbf{Y} - \varepsilon\frac{\partial W_1}{\partial \mathbf{y}} \tag{5.35}$$

The inverse transformation is obtained by replacing $\mathbf{y}$ and $\mathbf{Y}$ by $\mathbf{x}$ and $\mathbf{X}$, respectively, and negating W_1:

$$\mathbf{y} = \mathbf{x} - \varepsilon\frac{\partial W_1}{\partial \mathbf{X}} \qquad\qquad \mathbf{Y} = \mathbf{X} + \varepsilon\frac{\partial W_1}{\partial \mathbf{x}} \tag{5.36}$$

The first-order term in the Lie series expansion is, therefore,

$$\begin{aligned}\langle\mathcal{H}_1\rangle(\mathbf{y}, \mathbf{Y}, t) &= \mathcal{H}_1(\mathbf{y}, \mathbf{Y}, t) + (\mathcal{H}_0; W_1) - \frac{\partial W_1}{\partial t} \\ &= \mathcal{H}_1(\mathbf{y}, \mathbf{Y}, t) - \frac{\mu^2}{\bar{L}^3}\frac{\partial W_1}{\partial \bar{l}} - \frac{\partial W_1}{\partial t}\end{aligned} \tag{5.37}$$

since $\mathcal{H}_0$ depends only on $\bar{L}$. This yields the linear partial differential equation (PDE)

$$\frac{\mu^2}{\bar{L}^3}\frac{\partial W_1}{\partial \bar{l}} + \frac{\partial W_1}{\partial t} = \mathcal{H}_1(\mathbf{y}, \mathbf{Y}, t) - \langle\mathcal{H}_1\rangle(\mathbf{y}, \mathbf{Y}, t) \tag{5.38}$$

which is not trivial to solve.

To address this issue, the differences in the time scales of the problem will be exploited. Since the period of the satellite is much shorter than the period of the Moon's motion, it is reasonable to restrict attention in this transformation to

variations with respect to $\bar{l}$. In other words, assume the position of the Moon relative to the Earth is fixed throughout one orbit of the satellite and neglect the variation of W_1 with respect to t. This yields the (approximate) simplified equation

$$\frac{\mu^2}{\bar{L}^3}\frac{\partial W_1}{\partial \bar{l}} = \mathcal{H}_1\left(\mathbf{y}, \mathbf{Y}, t\right) - \left\langle \mathcal{H}_1 \right\rangle \left(\mathbf{y}, \mathbf{Y}, t\right) \tag{5.39}$$

which has the general solution

$$W_1 = \frac{\bar{L}^3}{\mu^2}\int \left(\mathcal{H}_1 - \left\langle \mathcal{H}_1 \right\rangle\right) d\bar{l} + W_1'\left(\_, \bar{g}, \bar{h}, \bar{L}, \bar{G}, \bar{H}, t\right) \tag{5.40}$$

where W_1' is a constant of integration with respect to $\bar{l}$ which can be neglected at first order.

The second near-identity transformations will remove all terms depending on l', that is t, from the Hamiltonian up to first order. The transformed Hamiltonian $\mathcal{M}$ has the form

$$\mathcal{M}\left(\mathbf{z}, \mathbf{Z}, \_\right) = \underbrace{\mathcal{H}_0\left(\_, \mathbf{Z}, \_\right)}_{\mathcal{M}_0(\_,\mathbf{Z},\_)} + \varepsilon \underbrace{\left\langle \left\langle \mathcal{H}_1 \right\rangle \right\rangle \left(\mathbf{z}, \mathbf{Z}, \_\right)}_{\mathcal{M}_1(\mathbf{z},\mathbf{Z},\_)} \tag{5.41}$$

where $\mathbf{z} = \begin{bmatrix} \bar{\bar{l}} & \bar{\bar{g}} & \bar{\bar{h}} \end{bmatrix}^T$ and $\mathbf{Z} = \begin{bmatrix} \bar{\bar{L}} & \bar{\bar{G}} & \bar{\bar{H}} \end{bmatrix}^T$ are the new double-averaged or lunar variables. The two-body term is again unchanged and $\mathcal{M}_1$ depends on neither $\bar{\bar{l}}$ nor t. The Lie series transformation is given by

$$\mathcal{M}_1\left(\mathbf{z}, \mathbf{Z}, \_\right) = \mathcal{K}_1\left(\mathbf{z}, \mathbf{Z}, t\right) + \left(\mathcal{H}_0; \bar{W}_1\right) - \frac{\partial \bar{W}_1}{\partial t} \tag{5.42}$$

which leads to the linear PDE

$$\frac{\mu^2}{\bar{\bar{L}}^3}\frac{\partial \bar{W}_1}{\partial \bar{\bar{l}}} + \frac{\partial \bar{W}_1}{\partial t} = \mathcal{K}_1\left(\mathbf{z}, \mathbf{Z}, t\right) - \left\langle \left\langle \mathcal{H}_1 \right\rangle \right\rangle \left(\mathbf{z}, \mathbf{Z}, \_\right) \tag{5.43}$$

Since none of the terms on the right-hand side depend on $\bar{\bar{l}}$ it can be assumed that

$\bar{W}_1$ also does not depend on $\bar{\bar{l}}$. Therefore, the general solution for $\bar{W}_1$ is given by

$$\begin{aligned}\bar{W}_1 &= \int \left(\mathcal{K}_1 - \langle\langle \mathcal{H}_1 \rangle\rangle\right) dt + \bar{W}_1' \left(\_, \bar{\bar{g}}, \bar{\bar{h}}, \bar{\bar{L}}, \bar{\bar{G}}, \bar{\bar{H}}, \_\right) \\ &= \frac{1}{n'} \left(\int \mathcal{K}_1 dl' - \langle\langle \mathcal{H}_1 \rangle\rangle l' \right) + \bar{W}_1' \left(\_, \bar{\bar{g}}, \bar{\bar{h}}, \bar{\bar{L}}, \bar{\bar{G}}, \bar{\bar{H}}, \_\right) \end{aligned} \tag{5.44}$$

since

$$l' = l_0' + n't \tag{5.45}$$

and where $\bar{W}_1'$ is another constant of integration which can be neglected. The forward and inverse transformations between the lunar and single-averaged variables are given by

$$\mathbf{y} = \mathbf{z} + \varepsilon \frac{\partial \bar{W}_1}{\partial \mathbf{Z}} \qquad\qquad \mathbf{Y} = \mathbf{Z} - \varepsilon \frac{\partial \bar{W}_1}{\partial \mathbf{z}} \tag{5.46}$$

and

$$\mathbf{z} = \mathbf{y} - \varepsilon \frac{\partial \bar{W}_1}{\partial \mathbf{Y}} \qquad\qquad \mathbf{Z} = \mathbf{Y} + \varepsilon \frac{\partial \bar{W}_1}{\partial \mathbf{y}} \tag{5.47}$$

V.C. Numerical Simulation

Numerical results will now be generated based on the methods of the previous sections using the parameters of Phases I and II of the NASA MMS mission described in Chapter IV. The high reference orbit apogees of this mission suggest that the lunar perturbation could have a significant effect on long-term formation performance, especially in Phase II [85]. For each of the following simulations, initial conditions for the three deputies are determined using the nominal SOC formation design algorithm of Section III.C.1 (10 km Phase I, 25 km Phase II formation sizes) with no perturbations (that is, using only the period-matching constraint $\delta a_j = 0$).

In general, the dynamics of satellite formations depend explicitly on both ab-

solute and differential orbital elements. According to Eqs. (5.11)–(5.16) and (5.17)–(5.22), the lunar perturbation causes long-term changes in all of the absolute and differential elements except a and δa. The rates are not constant, but because they are slowly-varying they can be integrated semianalytically (with a very large time step) or assumed to be linear over sufficiently short time spans.

The J_2 perturbation, on the other hand, causes changes in only Ω, ω, and M_0 and their differences. The effects of the lunar perturbation on $\delta\Omega$, $\delta\omega$, and δM_0 are compared to J_2 for one of the deputies in Figures V.1(a), for Phase I, and (b), for Phase II. As expected, in Phase I J_2 has a much larger effect than the lunar perturbation; however, in Phase II they are of roughly the same order of magnitude. Despite this, the lunar perturbation seems to have little effect on average quality factor (QF) in the region of interest (RoI) in either phase, as shown in Figures V.2(a) and (b), whereas J_2 can be seen to have a significant effect even when the modified J_2 along-track drift condition, Eq. (3.7), is applied (shown as black diamonds in the

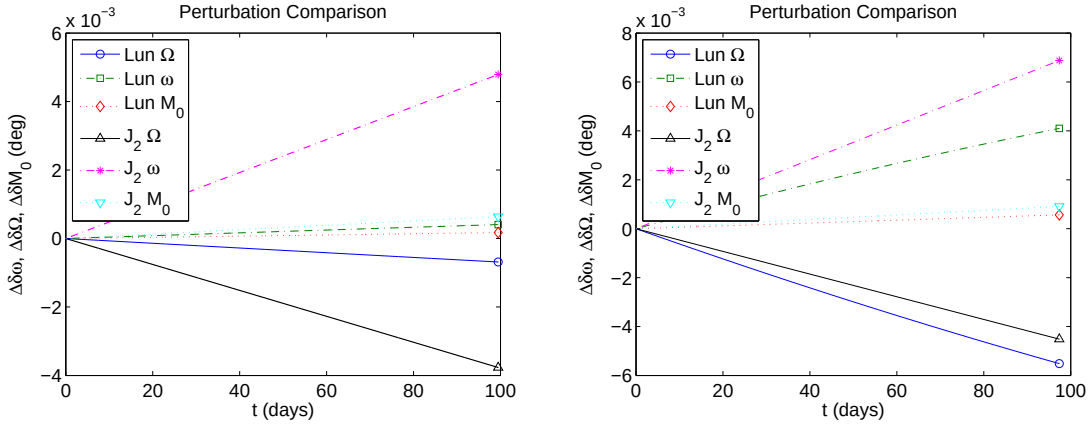

(a) Phase I. **(b) Phase II.**

Figure V.1. Comparison of secular J_2 and averaged lunar effects on differential elements.

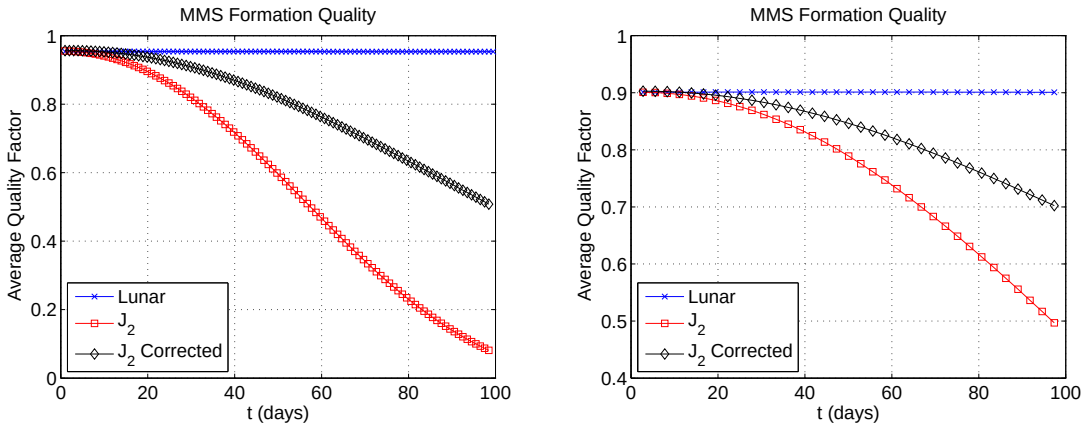

(a) Phase I. **(b) Phase II.**

Figure V.2. Comparison of average QF per RoI pass between J_2 and averaged lunar effects.

figures).

In addition, the effects of the lunar perturbation on Ω, ω, and M_0 and their differences are compared to secular J_2, J_2^2, and J_4 effects in Figures V.3, for Phase I, and V.4, for Phase II. As expected, higher order effects of the zonal harmonics are very small compared to first order J_2 and lunar perturbation effects. In both phases, changes due to J_2^2 and J_4 are virtually imperceptible on the scale shown here.

In the following sections, lunar effects on the individual orbital elements will be examined for both Phases I and II, and the averaged results will be compared with numerical integration of the actual equations of motion for the simplified (circular, equatorial lunar orbit) model with $M_0' = 90°$. Each figure in these sections will contain four sets of results: the solid blue line uses the averaged equations, Eqs. (5.11)–(5.22), with the corrected lunar-averaged elements for initial conditions (the **z**-type variables); the dash-dot green line uses the same equations with (uncorrected) osculating elements for initial conditions (the **x**-type variables); the dashed red line

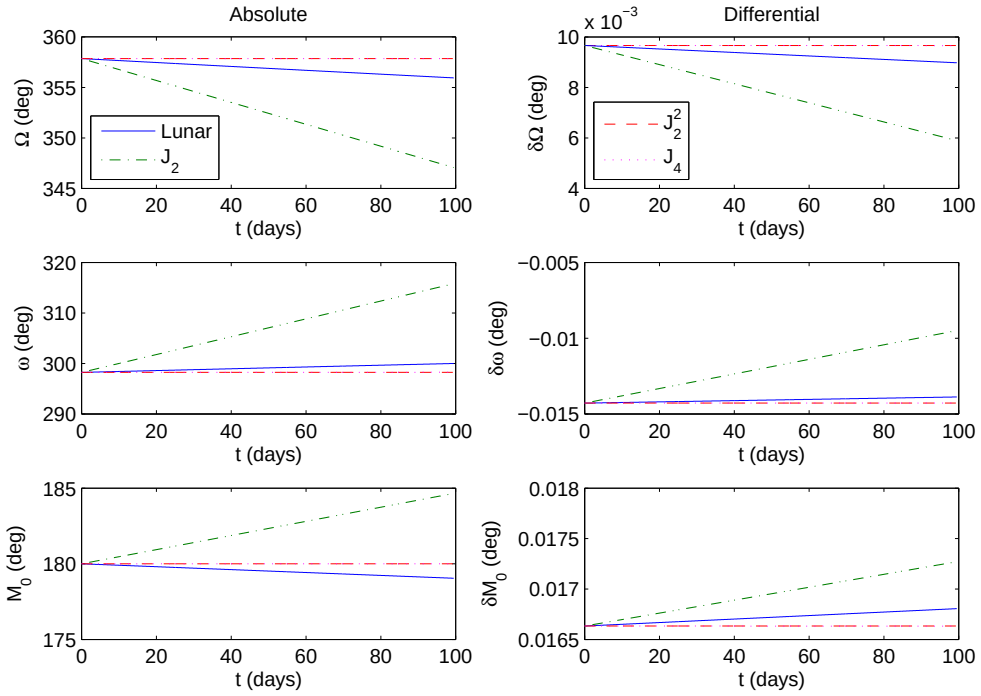

Figure V.3. Comparison of J_2, J_2^2, J_4, and lunar effects for Phase I.

uses numerical integration of the equations of motion for the indicated simulation model; and the dotted magenta line uses numerical integration of the single-averaged disturbing potential (corresponding to either Eq. (5.2) or (5.32)) with the corrected single-averaged elements for initial conditions (the **y**-type variables). In addition, $M_0 = M - nt$ is difficult to track over long time spans because oscillations in n induce large oscillations for large values of t. Instead,

$$\Delta M = M - \bar{\bar{n}}_0 t \tag{5.48}$$

will be plotted, along with its differential value.

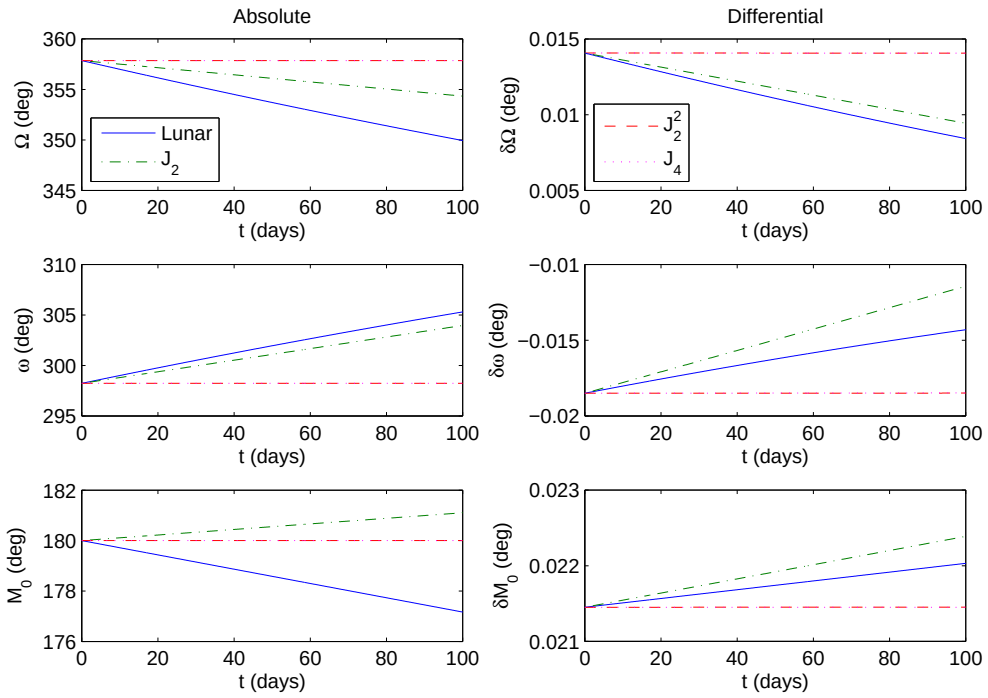

Figure V.4. Comparison of J_2, J_2^2, J_4, and lunar effects for Phase II.

V.C.1. MMS Phase I Results

Three sets of simulations are shown in this section for the MMS Phase I reference orbit. First, the averaged lunar equations are compared to the 1st-order simplified model, that is Eq. (5.1) (with only $k = 2$ terms and a circular, equatorial lunar orbit). Figure V.5 shows the evolution of the reference orbital elements and Figure V.6 shows the differential elements. Note that the lunar-averaged elements correctly track the averages of a, e, δa, and δe, while using the uncorrected osculating elements as initial conditions for the averaged equations introduces a significant bias in each. This bias influences the rates of each of the other elements but can be seen most clearly in its effect on ΔM and $\delta(\Delta M)$. For the remaining elements, there is little difference

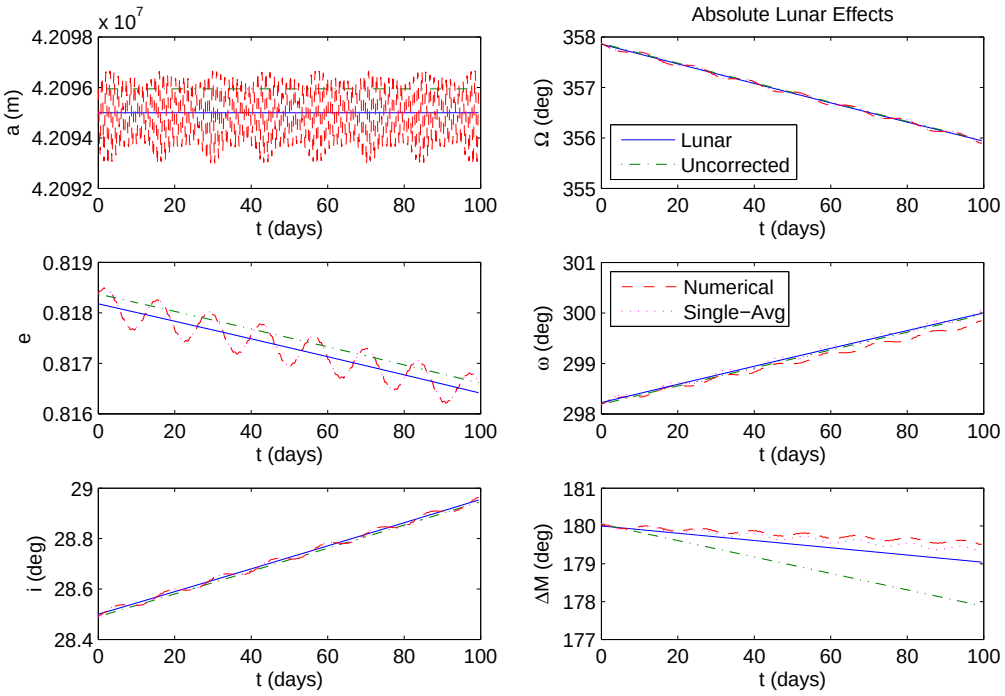

Figure V.5. Averaged lunar model for Phase I compared to 1st-order simplified model (reference elements).

between each of the results. The effect of each of the simplifying assumptions in the Lie series analysis can be seen by noting that there is a small discrepancy between the single-averaged and the numerical integration results and an additional small discrepancy between the lunar-averaged and the single-averaged results.

Second, the averaged lunar equations are compared to the full-order simplified model, that is Eq. (2.28) with a circular, equatorial lunar orbit. Figure V.7 shows the reference elements and Figure V.8 shows the differential elements. Clearly, higher-order terms in the lunar potential introduce much larger oscillations in the elements, although they do not contribute significantly to long-term changes in the average sense except in the cases of ΔM and $\delta(\Delta M)$. As was noted in the previous para-

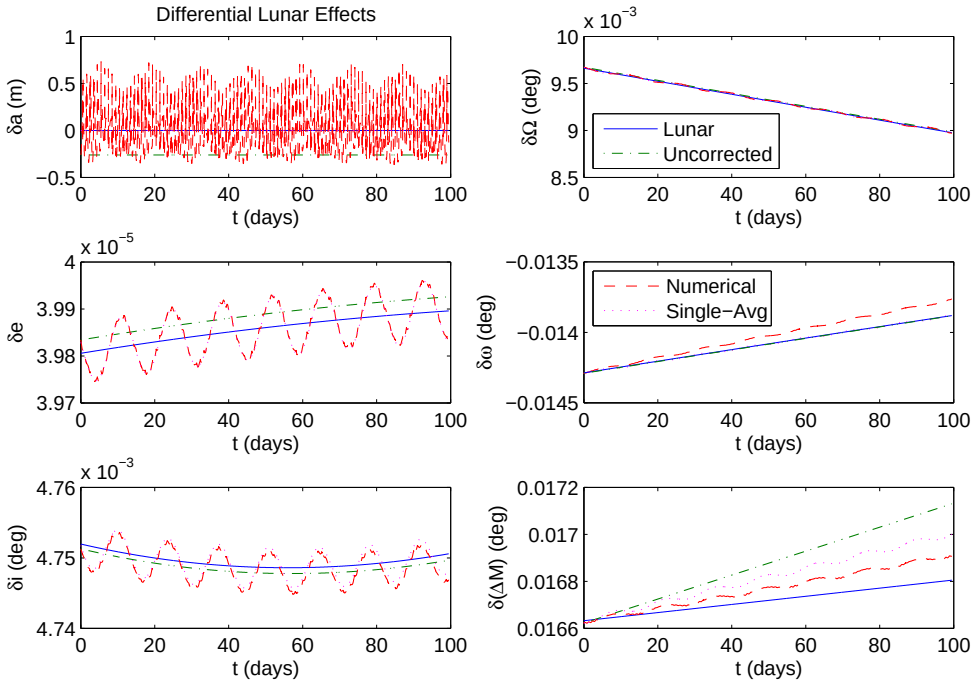

Figure V.6. Averaged lunar model for Phase I compared to 1st-order simplified model (differential elements).

graph, the now-uncorrected bias in a, e, δa, and δe introduces marked errors in the rates of ΔM and $\delta(\Delta M)$.

Finally, the first simulation (comparison with 1st-order simplified model) is propagated over a longer time span to see if the averaged equations accurately predict the satellites' motion in the long term. Only the reference elements are shown, in Figure V.9, and the semianalytic propagation performs as expected. As before, there is a predictable discrepancy between the averaged results and numerical integration, but there is no sudden divergence or large nonlinearity in the motion.

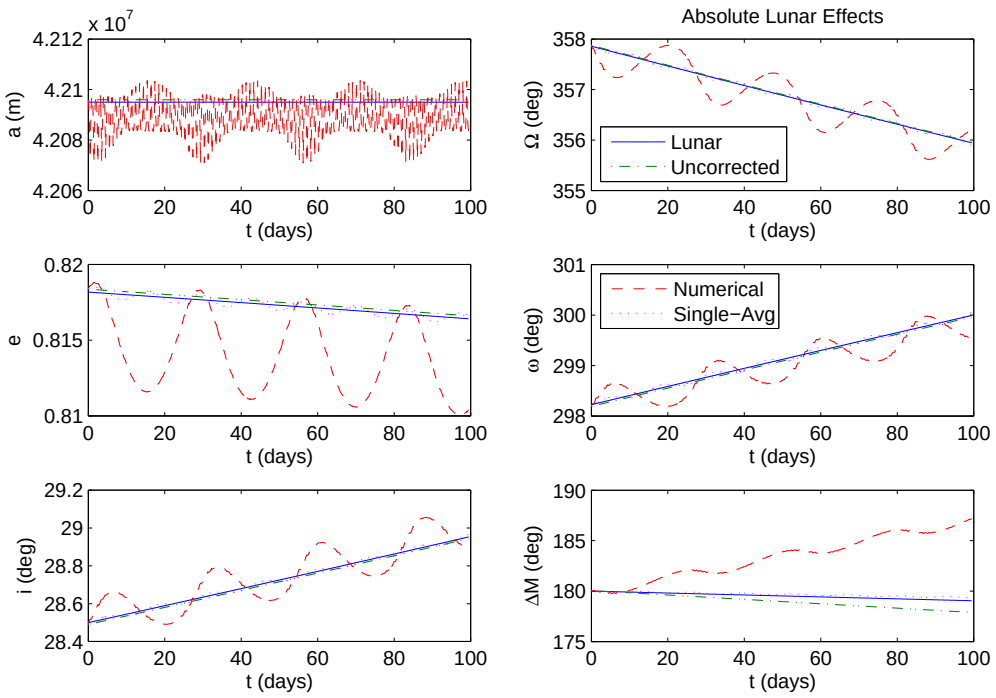

Figure V.7. Averaged lunar model for Phase I compared to full-order simplified model (reference elements).

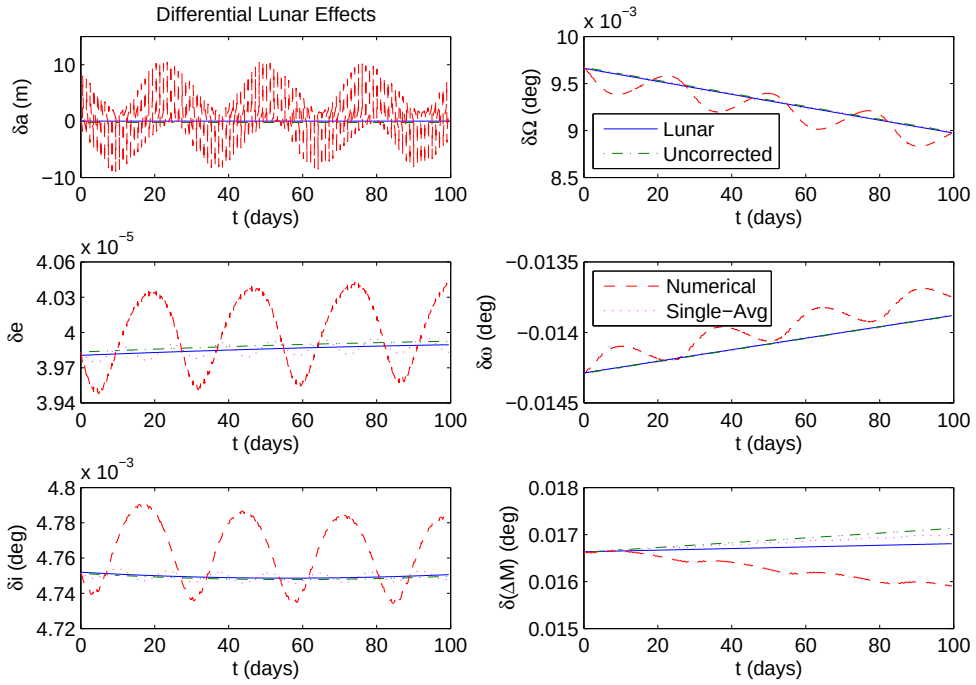

Figure V.8. Averaged lunar model for Phase I compared to full-order simplified model (differential elements).

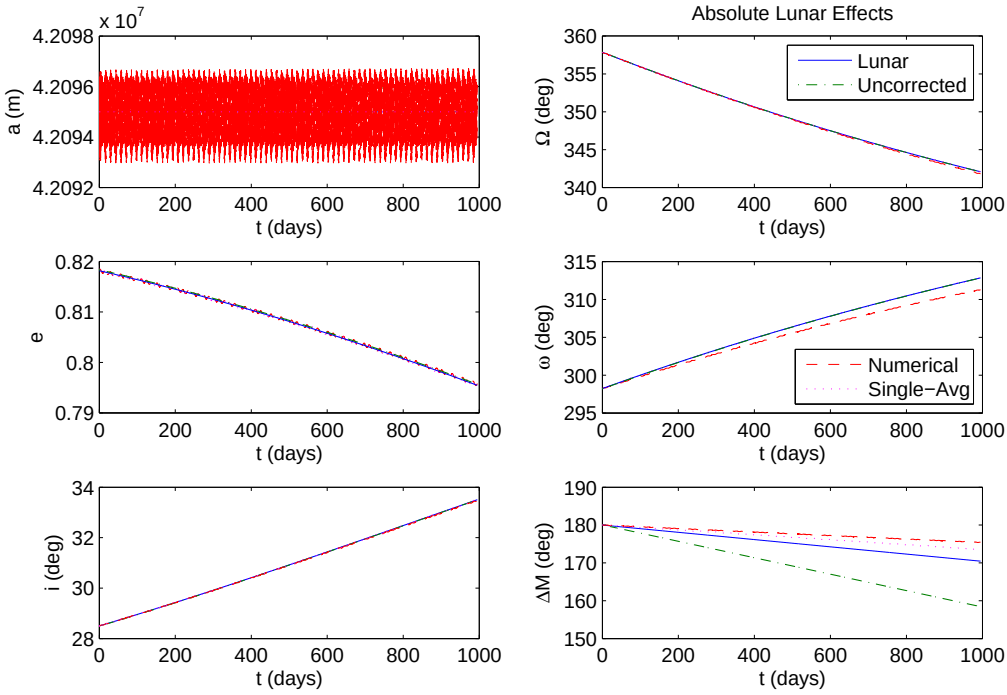

Figure V.9. Averaged lunar model for Phase I compared to 1st-order simplified model (long-term, reference elements).

V.C.2. MMS Phase II Results

The same three sets of simulations are shown in this section for the MMS Phase II reference orbit. First, the averaged lunar equations are compared to the 1st-order simplified model. Figure V.10 shows the reference elements and Figure V.11 shows the differential elements. As with Phase I, the lunar-averaged elements correctly track the averages of a, e, δa, and δe, while using the uncorrected osculating elements as initial conditions introduces a significant bias in each, which has a marked effect on ΔM and $\delta(\Delta M)$. The effect of each of the simplifying assumptions in the Lie series analysis can again be seen by noting that there is a small discrepancy between the single-averaged and the numerical integration results and an additional discrepancy

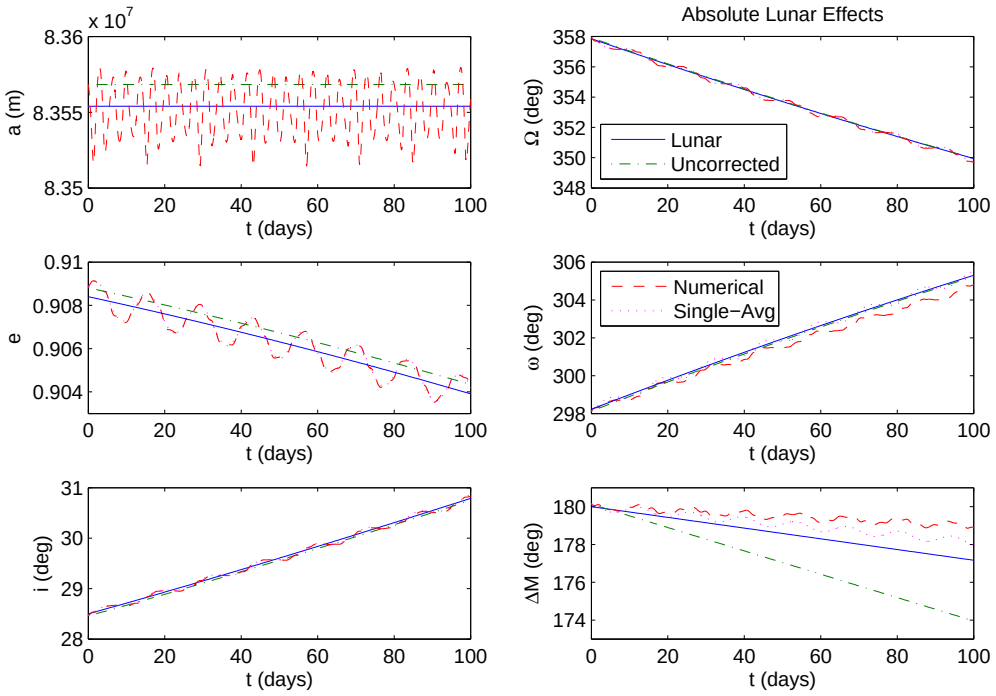

Figure V.10. Averaged lunar model for Phase II compared to 1st-order simplified model (reference elements).

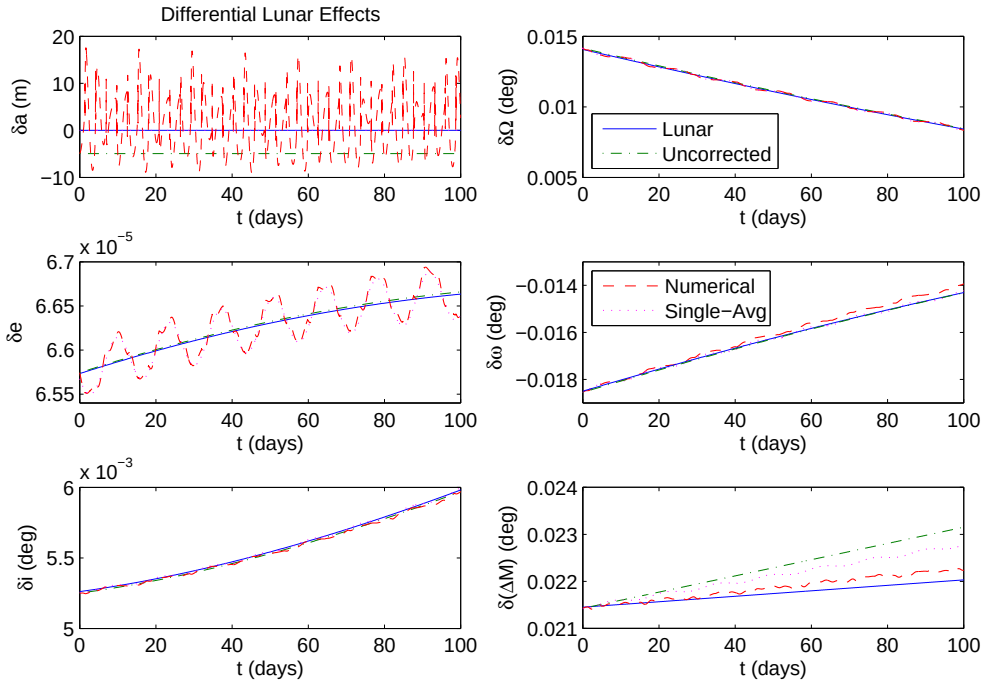

Figure V.11. Averaged lunar model for Phase II compared to 1st-order simplified model (differential elements).

between the lunar-averaged and the single-averaged results (most notable in ΔM and $\delta(\Delta M)$).

Second, the averaged lunar equations are compared to the full-order simplified model. Figure V.12 shows the reference elements and Figure V.13 shows the differential elements. Again, higher-order terms in the lunar potential introduce much larger oscillations in the elements, but in Phase II there is also a noticeable effect on the long-term rates of the elements. The now-uncorrected bias in a, e, δa, and δe introduces large errors in the rates of ΔM and $\delta(\Delta M)$.

Finally, the first simulation (comparison with 1st-order simplified model) is propagated over a longer time span to see if the averaged equations accurately predict

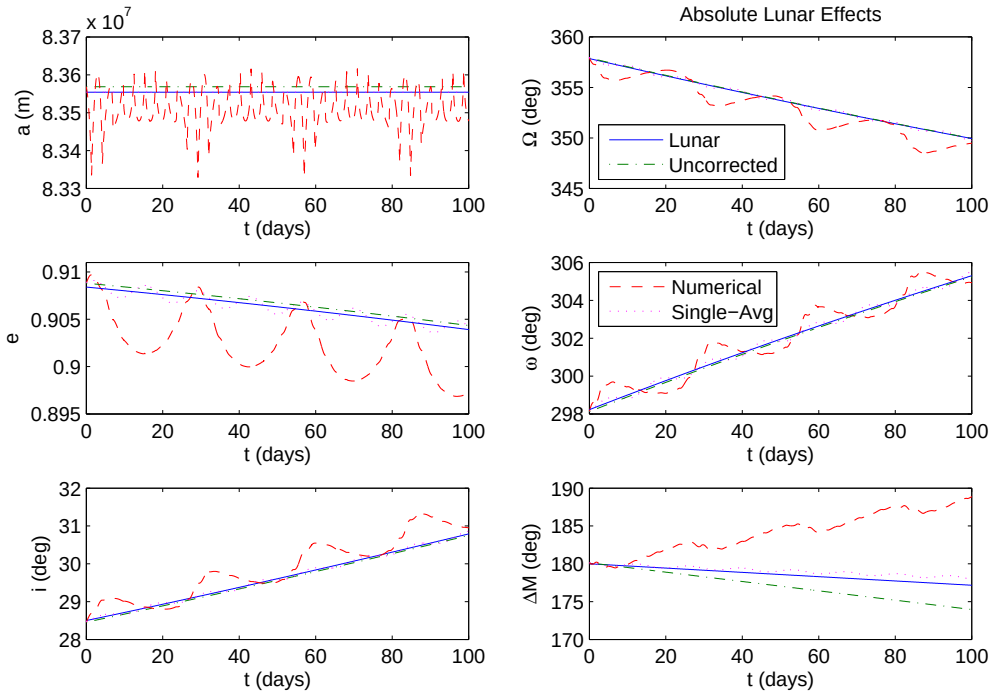

Figure V.12. Averaged lunar model for Phase II compared to full-order simplified model (reference elements).

the satellites' motion in the long term. Figure V.14 shows the reference elements and Figure V.15 shows the differential elements. The semianalytic propagation performs fairly well; however, there is considerably more nonlinearity in the evolution of the elements at the higher altitude of Phase II than there was in Phase I. Both the single-averaged and lunar-averaged ω and $\delta\omega$, in particular, begin to diverge after about 500 days. This extreme case (propagating for such a long time) illustrates the limitations of this method when the simplifying assumptions are being strained: for Phase II, the parameter $\varepsilon \approx 4.7 \times 10^{-2}$ (assumed to be small in performing the Lie series expansion) and the ratio of the satellite's period to the lunar period is approximately 0.1 (assumed to be small in solving Eq. (5.38)).

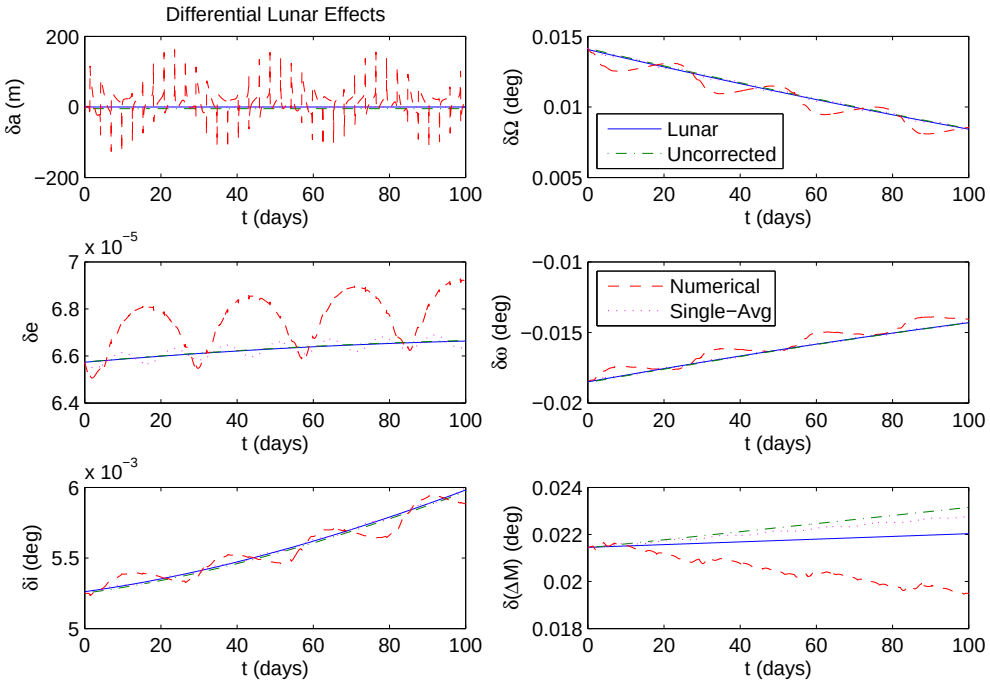

Figure V.13. Averaged lunar model for Phase II compared to full-order simplified model (differential elements).

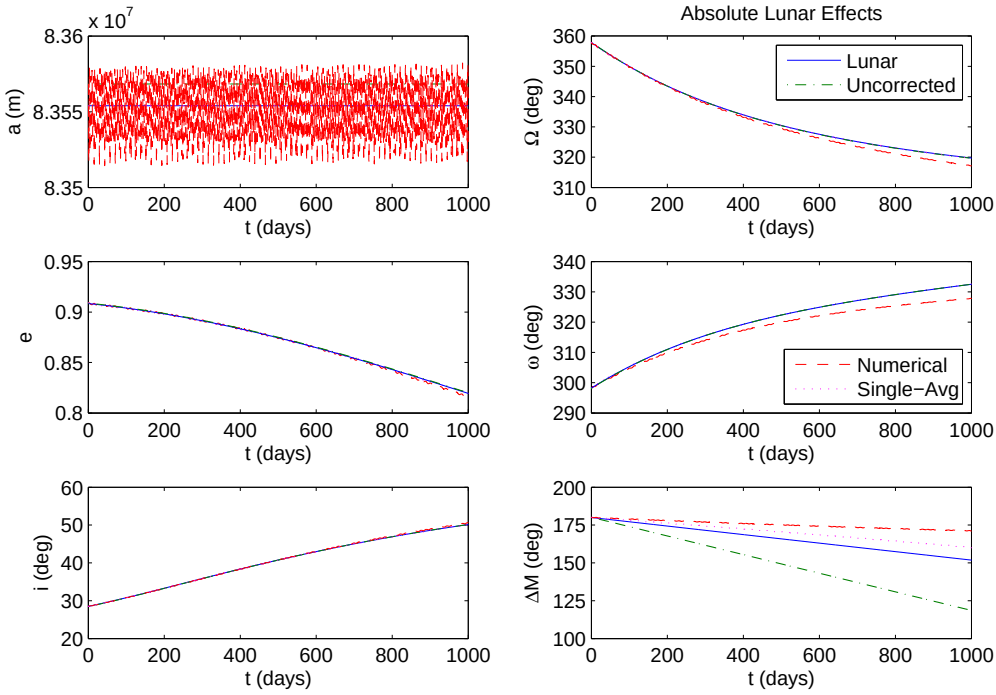

Figure V.14. Averaged lunar model for Phase II compared to 1st-order simplified model (long-term, reference elements).

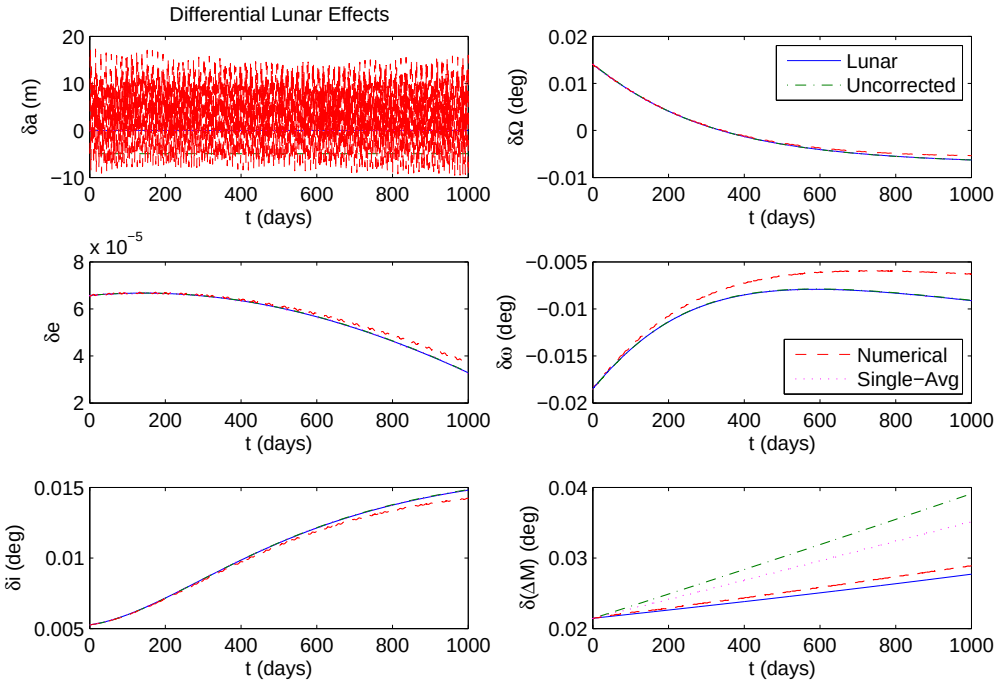

Figure V.15. Averaged lunar model for Phase II compared to 1st-order simplified model (long-term, differential elements).

V.D. High-Fidelity Verification

The analysis presented in the previous sections is based on a circular, equatorial lunar orbit, and it is expected that the accuracy of the predicted motion will degrade due to differences between this simplified model and actual lunar motion. It is expected that lunar orbit eccentricity (≈ 0.05) and inclination ($\approx 5^\circ$ with respect to the ecliptic) will cause noticeable departure from the predicted motion. In particular, the lunar inclination will significantly affect the the disturbing force since it varies between about 18° and 29° with respect to the Earth's equatorial plane throughout its almost 19 year nodal cycle. However, for sufficiently short time periods (compared to the nodal cycle) the lunar orbit can be assumed to have a constant orientation with respect to the geocentric equatorial frame to obtain satisfactory results.

V.D.1. Lunar Inclination

Retaining the assumption of a circular lunar orbit, but now including a constant right ascension of Ω' and inclination of i', the cosine of the angle between the satellite and the Moon, Eq. (2.35), becomes

$$\cos S_i = \alpha_i \cos f + \beta_i \sin f \tag{5.49}$$

where

$$\alpha_i = \left(c_\omega c_{\Delta\Omega} - s_\omega s_{\Delta\Omega} c_i\right) c_{M'} + \left(c_\omega s_{\Delta\Omega} c_{i'} + s_\omega c_{\Delta\Omega} c_i c_{i'} + s_\omega s_i s_{i'}\right) s_{M'} \tag{5.50}$$

$$\beta_i = -\left(s_\omega c_{\Delta\Omega} + c_\omega s_{\Delta\Omega} c_i\right) c_{M'} + \left(-s_\omega s_{\Delta\Omega} c_{i'} + c_\omega c_{\Delta\Omega} c_i c_{i'} + c_\omega s_i s_{i'}\right) s_{M'} \tag{5.51}$$

with $\Delta\Omega = \Omega - \Omega'$.

The first averaging of the disturbing potential, Eq. (5.2), and its generating

function, Eq. (5.40), are unchanged aside from the new form of α_i and β_i, since those quantities do not depend on M. The expressions for the double-averaged potential, Eq. (5.4), and its generating function, Eq. (5.44), become more complicated, because of the additional trigonometric terms, but the method for obtaining them is identical. The same is true of the corresponding expressions for the absolute and differential element rates, Eqs. (5.11)–(5.16) and (5.17)–(5.22). With this new formulation of the problem, the results predicted by this method can now be compared to results obtained using the GMAT with a spherical Earth and lunar point mass gravity model (based on high-fidelity lunar ephemeris data).

V.D.2. GMAT Simulation

First, the conclusion drawn based on Figures V.2(a) and (b) regarding the effect of the lunar perturbation on QF performance is verified. Figures V.16(a) and (b) show QF performance for Phases I and II based on several initial lunar orientations. As with the simplified model analysis, the lunar perturbation has little effect on QF evolution at either orbit altitude. To illustrate the effect of initial lunar orientation more distinctly, Figures V.16(c) and (d) show zoomed-in versions of the last five orbits of the previous figures. Clearly, the Moon's actual position does not have a significant impact on overall science return quality for missions such as MMS, so it is reasonable to use averaged lunar effects in evaluating this criterion.

Second, lunar-averaged results (based on the 1st-order simplified model, including lunar inclination) are compared to simulation in GMAT for Phase I. The 100 day simulation was computed based on lunar ephemeris data starting on January 19,

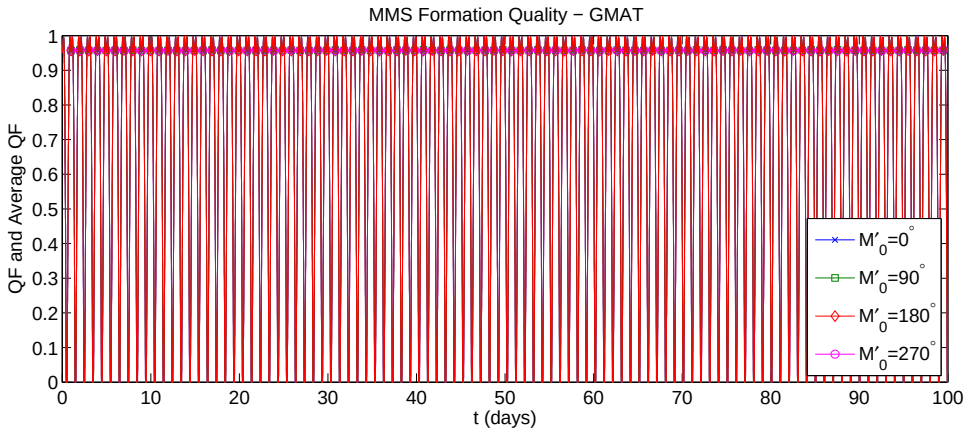

(a) Phase I.

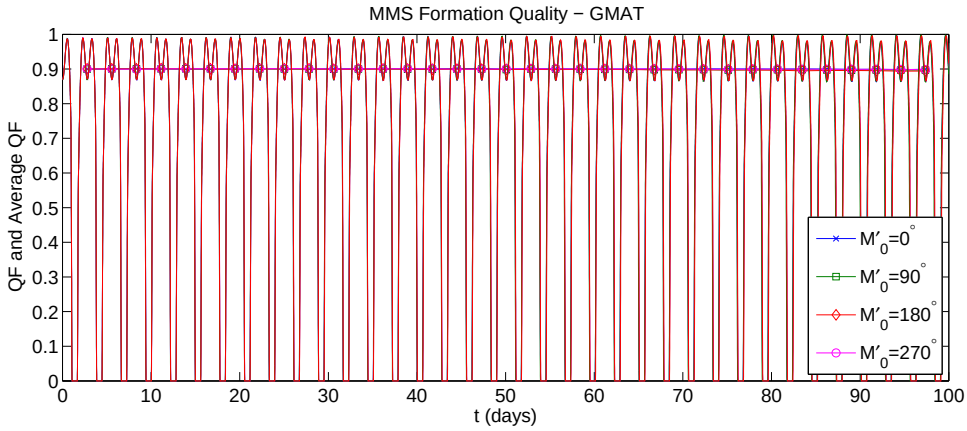

(b) Phase II.

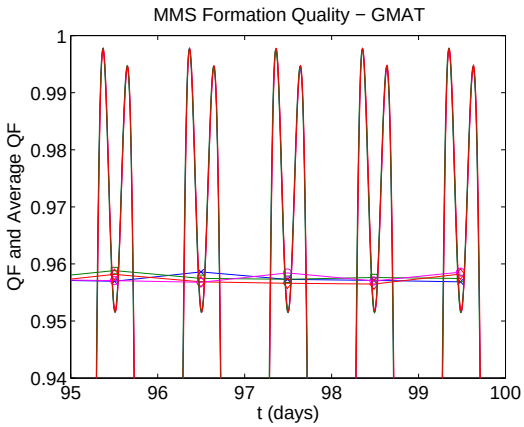

(c) Phase I (magnified).

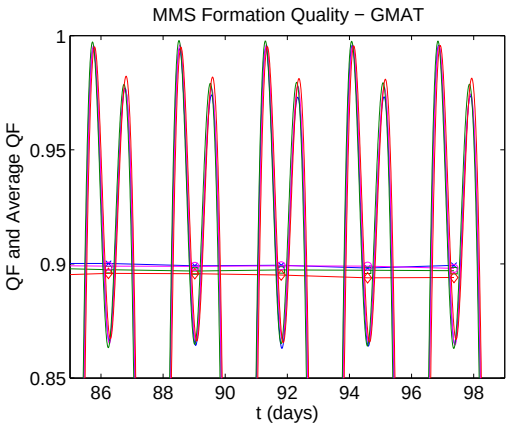

(d) Phase II (magnified).

Figure V.16. GMAT simulations for different M_0' values.

2000 (Julian Date 2451562.7), during which period the average values of Ω' and i' are approximately 10° and 21°, respectively, and $M_0' \approx 80°$. Figure V.17 shows the reference elements and Figure V.18 shows the differential elements. The simplified model does a good job predicting the average rates of the elements, with a moderate bias which affects ΔM and $\delta(\Delta M)$ (although the effect is worse in the case of the uncorrected initial conditions).

Finally, the lunar-averaged results are compared to simulation in GMAT for Phase II over the same time period. Figure V.19 shows the reference elements and Figure V.20 shows the differential elements. As with the Phase I results, the simplified model predicts the average rates of the elements well but there is a moderate

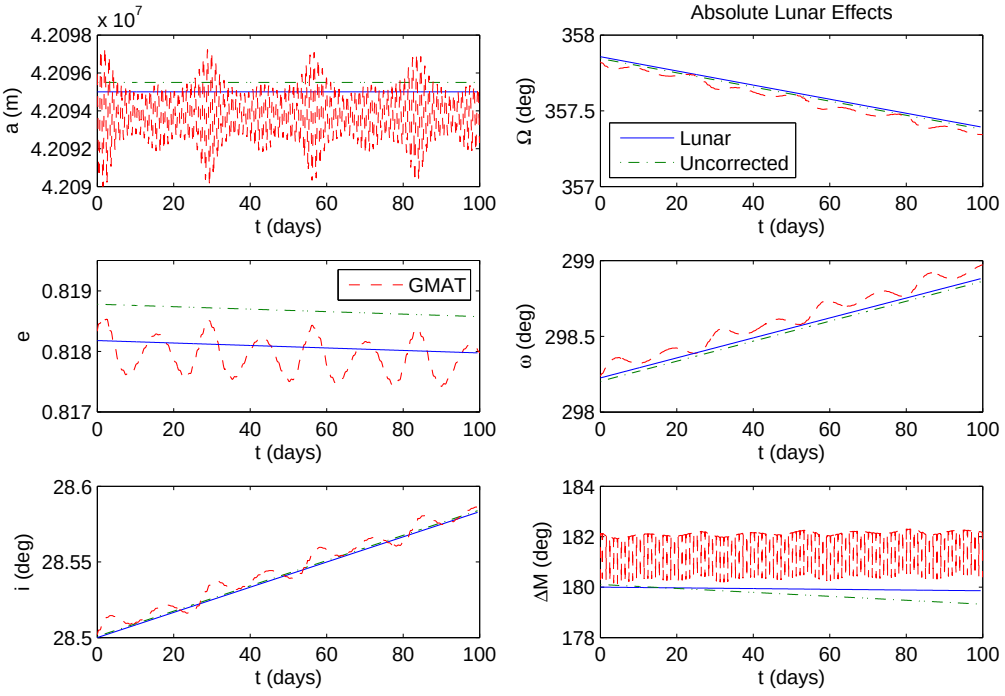

Figure V.17. Averaged lunar model for Phase I compared to GMAT simulation (reference elements).

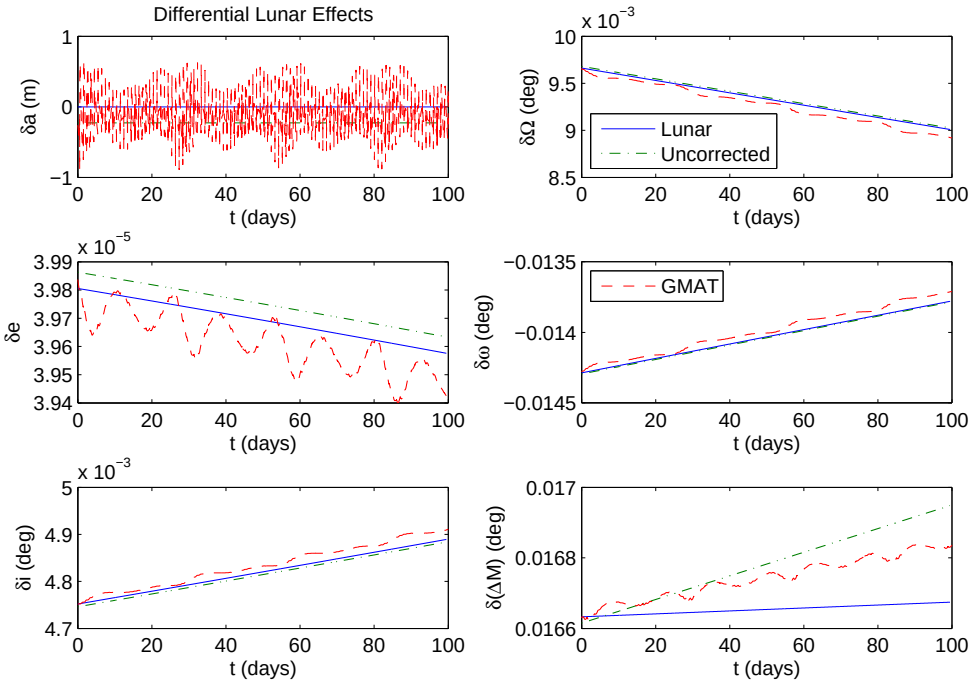

Figure V.18. Averaged lunar model for Phase I compared to GMAT simulation (differential elements).

bias which affects ΔM and $\delta(\Delta M)$. Again, using the uncorrected initial conditions produces a greater inaccuracy.

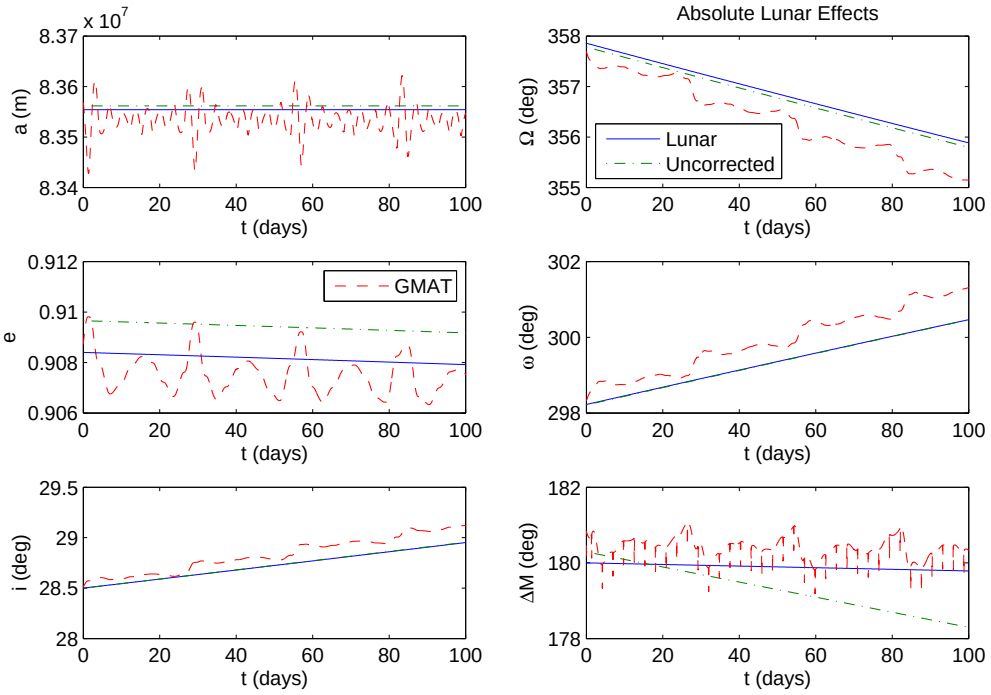

Figure V.19. Averaged lunar model for Phase II compared to GMAT simulation (reference elements).

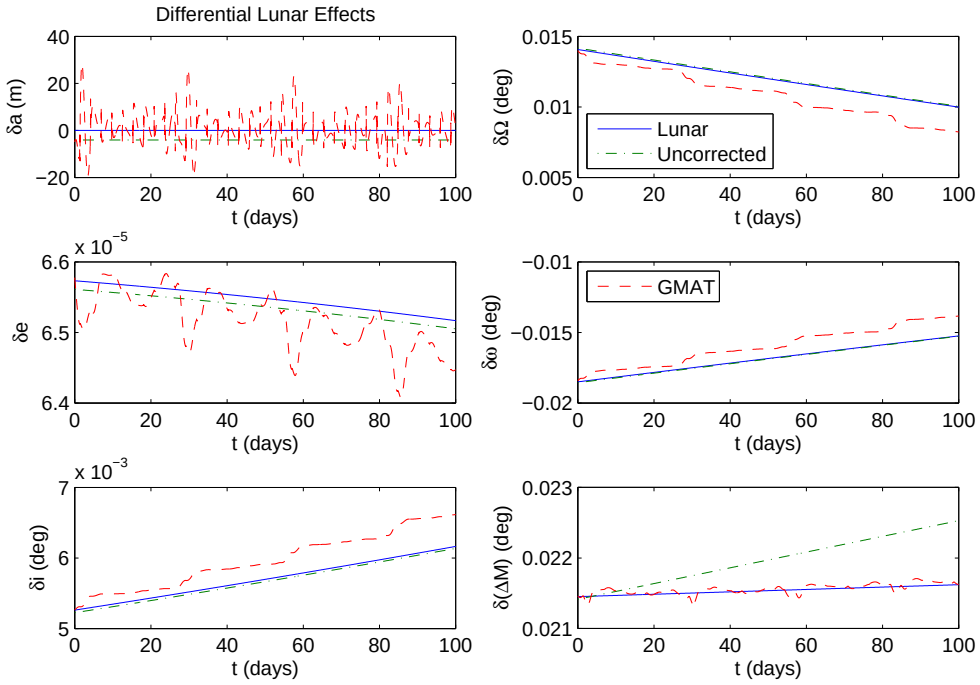

Figure V.20. Averaged lunar model for Phase II compared to GMAT simulation (differential elements).

CHAPTER VI

SUMMARY AND CONCLUSIONS

Many theories and techniques exist in the spacecraft dynamics and control literature for designing satellite formations for a variety of applications. The majority of work in this field has made use of simplified dynamic systems: circular or near-circular reference orbits, unperturbed equations of motion, short-duration timespans over which coarse integral approximations can be used, etc. In recent years, a number of more ambitious formation flying missions have been proposed, necessitating the development of advanced techniques which account for more general dynamic formulations. The present work augments the literature in this field with a set of formation design tools that are applicable to missions in high-eccentricity, high-altitude orbits involving general science return criteria specified over a specific portion of the orbit called the "Region of Interest" (RoI).

Two nominal formation design algorithms (FDAs), the single-orbit constrained (SOC) and multi-orbit unconstrained (MOU) optimizations, were defined using initial differential mean orbital elements as design variables and the Gim-Alfriend state transition matrix (G-A STM) for relative motion propagation. This choice of design variables and use of the G-A STM provide for a very efficient optimization framework and allow for simple, closed-form, analytical determination of the cost function gradients. A robust FDA was then defined using stochastic optimization, which uses knowledge of the distribution of expected formation initialization errors to allow for the sacrifice of some performance in the nominal case in order to gain robustness

with respect to these errors. The robust FDA is somewhat complex, so its application and effects were demonstrated by using a simple, scalar example problem. In addition, a new form of the traditional along-track drift condition was introduced, which accounts for the fact that performance criteria are only specified in the RoI and not throughout an entire orbit. Finally, the initialization process of a tetrahedron formation of satellites in terms of initial differential mean elements was outlined, including the application of the modified along-track drift condition while maintaining a desired tetrahedron geometry.

As a numerical example, the nominal and robust FDAs were applied to the complete formation design problem of the NASA Magnetospheric Multiscale (MMS) mission, which involves two distinct reference orbit phases. With appropriate use of the modified along-track drift condition, the SOC optimization was found to produce results almost as good as the MOU optimization in the error-free case, but at a fraction of the computational cost. As expected, formations designed using the nominal FDAs did not perform well in the presence of initialization errors. Thus, the robust FDA was used to modify the designs to lessen their sensitivities to initialization errors and improved performance was verified by statistical analysis of the resulting formation lifetime distributions. This algorithm will now be used by NASA as part of the process of planning formation maintenance maneuvers for MMS mission operations. The computation and analysis was performed in MATLAB using the G-A STM and results were validated using the NASA General Mission Analysis Tool (GMAT).

A physical analysis of the results of the MMS formation design example was

performed to investigate the geometric properties of the various design methods and resulting formation configurations. Orbit problems are generally replete with symmetry, and this one is no exception. On a single-orbit scale, the best formations exhibit a "double-hump" behavior, in which the quality factor (QF) is symmetric about apogee with peaks near 1 (the ideal, desired value) on either side (indicating a time at which the tetrahedron formation is nearly regular). On a multi-orbit scale, the average QF is also approximately symmetric about its peak value. Taking advantage of this behavior, the MOU optimization produced formations which had lower qualities in the zeroth orbit, but which remained stable nearly twice as long as formations with the peak QF in the zeroth orbit. This analysis also discovered that optimal formations generally fall into certain families, with geometries that can be characterized straightforwardly in the orbital coordinate frame, an insight which could not be obtained from purely numerical results. In addition, formations with different close approach tendencies were investigated and some conclusions were drawn about what geometric or dynamic characteristics govern such behavior in highly eccentric orbits.

Absolute and differential third-body perturbation effects on satellite formations were derived analytically using canonical transformation theory and the method of averaging, including the transformation between the averaged and osculating variables. The analysis was performed in particular for the perturbing effect of the Moon, but it is possible to adapt the method for other perturbing bodies, provided careful attention is paid to the relative time scales of the problem. Simulations were again performed using the MMS mission as an example problem and the results were

verified using GMAT. Results were more accurate when the transformed, averaged initial conditions are used, rather than the uncorrected, osculating initial conditions.

VI.A. Future Work

Several avenues are available for expanding on the developments of the work presented here. First, the k_j parameter defined in the modified along-track drift condition of Section III.A.1 is not entirely satisfactory. Acceptable results were obtained by selecting k_j heuristically, based on the results of numerical analyses and approximate analytical techniques, but it may be possible to refine the analysis to yield a better, analytical solution. Second, the robust FDA dealt exclusively with δa errors, which is reasonable since their effect on formation stability is $\mathcal{O}(1)$, whereas the effect of errors in any other element is $\mathcal{O}(J_2)$ or smaller. However, for certain applications it may be desirable to incorporate errors in other parameters into the optimization framework as well. As long as some knowledge of the particular error distribution can be assumed, this should be possible by a relatively straightforward application of the methods of Section III.D.1. Third, if any of the present algorithms or models are used in flight, for example on the MMS mission, then detailed post-flight analysis should be done for real-world validation of the methods.

One topic of paramount interest for missions such as MMS is that of collision or close approach avoidance. The FDAs defined in Chapter III did not include any explicit minimum separation distance constraints in the problem formulation. Including such a path constraint is not computationally attractive since it must be evaluated an every point throughout the orbit. Therefore, the development of general

techniques or conditions for passively guaranteeing minimum safe distances between the satellites in a formation would be an extremely valuable contribution to the formation flying literature. Such techniques exist for designing formations in circular and near-circular reference orbits, but extending these to cases of general reference orbits (in particular for high-eccentricity orbits) is not at all straightforward. Some intuitive results were obtained and conclusions were drawn regarding this topic for the particular case of MMS in Chapter IV, but the analysis is incomplete and satisfactory general results could not be obtained. The results of that chapter could serve as a useful starting point for future investigations in this area.

The third-body perturbation analysis could be extended or generalized in a number of ways. The equations presented in Chapter V are particular to the lunar perturbation: a natural next step would be to repeat the analysis for the solar perturbation. Furthermore, lunar perturbation effects were compared to J_2 effects, but the combination of these perturbations was not considered in the analytical analysis. In addition, more accurate lunar or solar orbit models could be incorporated into the analysis. However, the problem should not be made overly general or else the dynamics will become too complex to be useful for analytical analysis. The primary utility of this method is to solve simplified analytical models in order to provide design insights not available from numerical simulations. Such models are also easily adaptable to different problems and are extremely fast to evaluate. For these reasons, it is advantageous to develop simple, relatively accurate (but not necessarily perfect) analytical methods for designing satellite formations, even if only to provide overall physical analysis and initial guesswork for high-fidelity numerical solvers/optimizers.

REFERENCES

[1] Kong, E. M., Miller, D. W., and Sedwick, R. J., "Optimal Trajectories and Orbit Design for Separated Spacecraft Interferometry," Tech. Rep. SERC #13-98, Massachusetts Institute of Technology, Cambridge, MA, November 1998.

[2] Rodriguez-Canabal, J., "Cluster: Consolidated Report on Mission Analysis," Tech. Rep. ESOC CL-ESC-RP-0001, European Space Operation Centre, Darmstadt, Germany, July 1990.

[3] Schoenmaekers, J., "Cluster: Fuel Optimum Spacecraft Formation Control," *ESA Symposium on Space Flight Dynamics*, Darmstadt, Germany, December 1991, pp. 419–425.

[4] Dow, J., Matussi, S., Dow, R. M., Schmidt, M., and Warhaut, M., "The Implementation of the Cluster II Constellation," *Acta Astronautica*, Vol. 54, No. 9, 2004, pp. 657–669.

[5] Moreira, A., Krieger, G., Hajnsek, I., Werner, M., Hounam, D., Riegger, S., and Settelmeyer, E., "TanDEM-X: A TerraSAR-X Add-On Satellite for Single-Pass SAR Interferometry," *International Geoscience & Remote Sensing Symposium*, Anchorage, AK, 2004.

[6] Werninghaus, R. and Buckreuss, S., "The TerraSAR-X Mission and System Design," *IEEE Transactions on Geoscience and Remote Sensing*, Vol. 48, No. 2, February 2010, pp. 606–614.

[7] Persson, S., Jakobsson, B., and Gill, E., "PRISMA Demonstration Mission for Advanced Rendezvous and Formation Flying Technologies and Sensors," *56th International Astronautical Congress*, October 2005.

[8] Persson, S., Veldman, S., and Bodin, P., "PRISMA — A Formation Flying Project in Implementation Phase," *Acta Astronautica*, Vol. 65, No. 9–10, 2009, pp. 1360–1374.

[9] Orr, N. G., Eyer, J. K., Larouche, B. P., and Zee, R. E., "Precision Formation Flight: The CanX-4 and CanX-5 Dual Nanosatellite Mission," *21st AIAA/USU Conference on Small Satellites*, Salt Lake City, UT, August 2007.

[10] Yoshihara, K., van Mierlo, M., Ng, A., Kumar, B. S., de Ruiter, A., Komatsu, Y., Horiguchi, H., and Hashimoto, H., "JC2Sat-FF: An International Collaboration Nano-Sat Project—Overview of the System Analyses and Design," *Small Satellite Systems and Services (4S) Symposium*, Rhodes, Greece, May 2008.

[11] Curtis, S., "The Magnetospheric Multiscale Mission... Resolving Fundamental Processes in Space Plasmas," *Report of the NASA Science and Technology Definition Team for the MMS Mission*, NASA/TM-2000-209883, 1999.

[12] Alfriend, K. T., Vadali, S. R., Gurfil, P., How, J. P., and Breger, L. S., *Spacecraft Formation Flying: Dynamics, Control and Navigation*, Elsevier, Oxford, UK, 2010.

[13] Hill, G. W., "Researches in the Lunar Theory," *American Journal of Mathematics*, Vol. 1, No. 1, 1878, pp. 5–26.

[14] Clohessy, W. H. and Wiltshire, R. S., "Terminal Guidance System for Satellite Rendezvous," *Journal of the Aerospace Sciences*, Vol. 27, No. 9, 1960, pp. 653–658.

[15] London, H. S., "Second Approximation to the Solution of the Rendezvous Equations," *AIAA Journal*, Vol. 1, No. 7, July 1963, pp. 1691–1693.

[16] Anthony, M. L. and Sasaki, F. T., "Rendezvous Problem for Nearly Circular Orbits," *AIAA Journal*, Vol. 3, No. 9, September 1965, pp. 1666–1673.

[17] de Vries, J. P., "Elliptic Elements in Terms of Small Increments of Position and Velocity Components," *AIAA Journal*, Vol. 1, No. 11, November 1963, pp. 2626–2629.

[18] Lawden, D. F., *Optimal Trajectories for Space Navigation*, Butterworths, London, UK, 1963.

[19] Tschauner, J. and Hempel, P., "Rendezvous zu einem in elliptischer Bahn umlaufenden Ziel," *Astronautica Acta*, Vol. 11, No. 5, 1965, pp. 312–321.

[20] Tschauner, J., "Elliptic Orbit Rendezvous," *AIAA Journal*, Vol. 5, No. 6, June 1967, pp. 1110–1113.

[21] Carter, T. E., "New Form for the Optimal Rendezvous Equations Near a Keplerian Orbit," *Journal of Guidance, Control, and Dynamics*, Vol. 13, No. 1, January–February 1990, pp. 183–186.

[22] Euler, E. A. and Shulman, Y., "Second-Order Solution to the Elliptic Rendezvous Problem," *AIAA Journal*, Vol. 5, No. 5, May 1967, pp. 1033–1035.

[23] Carter, T. E., "State Transition Matrices for Terminal Rendezvous Studies: Brief Survey and New Example," *Journal of Guidance, Control, and Dynamics*, Vol. 21, No. 1, January–February 1998, pp. 148–155.

[24] Melton, R. G., "Time-Explicit Representation of Relative Motion between Elliptical Orbits," *Journal of Guidance, Control, and Dynamics*, Vol. 23, No. 4, July–August 2000, pp. 604–610.

[25] Inalhan, G., Tillerson, M., and How, J. P., "Relative Dynamics and Control of Spacecraft Formations in Eccentric Orbits," *Journal of Guidance, Control, and Dynamics*, Vol. 25, No. 1, January–February 2002, pp. 48–59.

[26] Sengupta, P. and Vadali, S. R., "Relative Motion and the Geometry of Formations in Keplerian Elliptic Orbits," *Journal of Guidance, Control, and Dynamics*, Vol. 30, No. 4, July–August 2007, pp. 953–964.

[27] Broucke, R. A., "Solution of the Elliptic Rendezvous Problem with the Time as Independent Variable," *Journal of Guidance, Control, and Dynamics*, Vol. 26, No. 4, July–August 2003, pp. 615–621.

[28] Yamanaka, K. and Ankersen, F., "New State Transition Matrix for Relative Motion on an Arbitrary Elliptical Orbit," *Journal of Guidance, Control, and Dynamics*, Vol. 25, No. 1, January–February 2002, pp. 60–66.

[29] Schaub, H. and Alfriend, K. T., "J_2 Invariant Reference Orbits for Spacecraft Formations," *Celestial Mechanics and Dynamical Astronomy*, Vol. 79, No. 2, February 2001, pp. 77–95.

[30] Vadali, S. R., Vaddi, S. S., and Alfriend, K. T., "A New Concept for Controlling Formation Flying Satellite Constellations," *Advances in the Astronautical Sciences*, Vol. 108, 2001, pp. 1631–1648.

[31] Gim, D.-W. and Alfriend, K. T., "State Transition Matrix of Relative Motion for the Perturbed Noncircular Reference Orbit," *Journal of Guidance, Control, and Dynamics*, Vol. 26, No. 6, November–December 2003, pp. 956–971.

[32] Gim, D.-W. and Alfriend, K. T., "Satellite Relative Motion using Differential Equinoctial Elements," *Celestial Mechanics and Dynamical Astronomy*, Vol. 92, No. 4, August 2005, pp. 295–336.

[33] Vadali, S. R., "An Analytical Solution for Relative Motion of Satellites," *5th Dynamics and Control of Systems and Structures in Space Conference*, Cranfield, UK, July 2002.

[34] Sengupta, P., Vadali, S. R., and Alfriend, K. T., "Modeling and Control of Satellite Formations in High Eccentricity Orbits," *Journal of the Astronautical Sciences*, Vol. 52, No. 1–2, 2004, pp. 149–168.

[35] Yan, H., Sengupta, P., Vadali, S. R., and Alfriend, K. T., "Development of a State Transition Matrix for Relative Motion using the Unit Sphere Approach," *Advances in the Astronautical Sciences*, Vol. 119, No. 1, 2004, pp. 935–946.

[36] Garrison, J. L., Gardner, T. G., and Axelrad, P., "Relative Motion in Highly Elliptical Orbits," *Advances in the Astronautical Sciences*, Vol. 89, 1995, pp. 1359–1376.

[37] Alfriend, K. T. and Schaub, H., "Dynamics and Control of Spacecraft Formations: Challenges and Some Solutions," *Journal of the Astronautical Sciences*, Vol. 48, No. 2–3, 2000, pp. 249–267.

[38] Alfriend, K. T. and Yan, H., "An Orbital Elements Approach to the Nonlinear Formation Flying Problem," *International Formation Flying Symposium*, Toulouse, France, October 29–31 2002.

[39] Schaub, H., "Relative Orbit Geometry through Classical Orbit Element Differences," *Journal of Guidance, Control, and Dynamics*, Vol. 27, No. 5, September–October 2004, pp. 839–848.

[40] Hughes, S. P. and Hall, C. D., "Optimal Configurations of Rotating Spacecraft Formations," *Journal of the Astronautical Sciences*, Vol. 48, No. 2–3, 2000, pp. 225–247.

[41] Chichka, D. F., "Satellite Cluster with Constant Apparent Distribution," *Journal of Guidance, Control, and Dynamics*, Vol. 24, No. 1, January–February 2001, pp. 117–122.

[42] Hamel, J.-F. and de Lafontaine, J., "Linearized Dynamics of Formation Flying Spacecraft on a J_2-Perturbed Elliptical Orbit," *Journal of Guidance, Control, and Dynamics*, Vol. 30, No. 6, November–December 2007, pp. 1649–1658.

[43] Gurfil, P., "Generalized Solutions for Relative Spacecraft Orbits under Arbitrary Perturbations," *Acta Astronautica*, Vol. 60, 2007, pp. 61–78.

[44] Sengupta, P., Vadali, S. R., and Alfriend, K. T., "Averaged Relative Motion and Applications to Formation Flight near Perturbed Orbits," *Journal of Guidance, Control, and Dynamics*, Vol. 31, No. 2, March–April 2008, pp. 258–272.

[45] Leonard, C. L., Hollister, W. M., and Bergmann, E. V., "Orbital Formation-keeping with Differential Drag," *Journal of Guidance, Control, and Dynamics*, Vol. 12, No. 1, January–February 1989, pp. 108–113.

[46] Humi, M. and Carter, T. E., "Rendezvous Equations in a Central-Force Field with Linear Drag," *Journal of Guidance, Control, and Dynamics*, Vol. 25, No. 1, January–February 2002, pp. 74–79.

[47] Carter, T. E. and Humi, M., "Clohessy-Wiltshire Equations Modified to Include Quadratic Drag," *Journal of Guidance, Control, and Dynamics*, Vol. 6, No. 6, November–December 2002, pp. 1058–1063.

[48] Bevilacqua, R. and Romano, M., "Rendezvous Maneuvers of Multiple Spacecraft using Differential Drag under J_2 Perturbation," *Journal of Guidance, Control, and Dynamics*, Vol. 31, No. 6, November–December 2008, pp. 1595–1607.

[49] Brouwer, D., "Solution of the Problem of Artificial Satellite Theory Without Drag," *The Astronomical Journal*, Vol. 64, No. 1274, November 1959, pp. 378–397.

[50] Kozai, Y., "On the Effects of the Sun and the Moon upon the Motion of a Close Earth Satellite," Smithsonian Astrophysical Observatory Special Report 22 (Part 2), 1959.

[51] Musen, P., Bailie, A., and Upton, E., "Development of the Lunar and Solar Perturbations in the Motion of an Artificial Satellite," NASA-TN D494, 1961.

[52] Kaula, W. M., "Development of the Lunar and Solar Disturbing Functions for a Close Satellite," *The Astronomical Journal*, Vol. 67, No. 5, June 1962, pp. 300–303.

[53] Giacaglia, G. E. O., "Lunar Perturbations of Artificial Satellites of the Earth," *Celestial Mechanics and Dynamical Astronomy*, Vol. 9, No. 2, April 1974, pp. 239–267.

[54] Kozai, Y., "A New Method to Compute Lunisolar Perturbations in Satellite Motions," Smithsonian Astrophysical Observatory Special Report 349, 1973.

[55] Prado, A. F. B. A., "Third-Body Perturbation in Orbits around Natural Satellites," *Journal of Guidance, Control, and Dynamics*, Vol. 26, No. 1, January–February 2003, pp. 33–40.

[56] Broucke, R. A., "Long-Term Third-Body Effects via Double Averaging," *Journal of Guidance, Control, and Dynamics*, Vol. 26, No. 1, January–February 2003, pp. 27–32.

[57] Lara, M., San Juan, J. F., and López, L. M., "Semianalytic Integration of High-Altitude Orbits under Lunisolar Effects," *Mathematical Problems in Engineering*, Vol. 2012, Article ID 659396, 17 pages, 2012.

[58] McLaughlin, C. A., Sabol, C., Swank, A., Burns, R. D., and Luu, K. K., "Modeling Relative Position, Relative Velocity, and Range Rate for Formation Flying," *Advances in the Astronautical Sciences*, Vol. 109, No. 3, 2002, pp. 2165–2186.

[59] Wnuk, E. and Golebiewska, J., "The Relative Motion of Earth Orbiting Satellites," *Celestial Mechanics and Dynamical Astronomy*, Vol. 91, No. 3–4, March 2005, pp. 373–389.

[60] Williams, T. and Wang, Z.-S., "Uses of Solar Radiation Pressure for Satellite Formation Flight," *International Journal of Robust and Nonlinear Control*, Vol. 12, 2002, pp. 163–183.

[61] Wang, Z.-S. and Williams, T., "Solar Wing Steering Law for Satellite Formation Flight," *Journal of the Astronautical Sciences*, Vol. 51, No. 2, 2003, pp. 227–246.

[62] Gong, S., Yunfeng, G., and Li, J., "Solar Sail Formation Flying on an Inclined Earth Orbit," *Acta Astronautica*, Vol. 68, 2011, pp. 226–239.

[63] Karlgaard, C. D. and Lutze, F. H., "Second-Order Relative Motion Equations," *Journal of Guidance, Control, and Dynamics*, Vol. 26, No. 1, January–February 2003, pp. 41–49.

[64] Richardson, D. L. and Mitchell, J. W., "A Third-Order Analytical Solution for Relative Motion with a Circular Reference Orbit," *Journal of the Astronautical Sciences*, Vol. 51, No. 1, 2003, pp. 1–12.

[65] Vaddi, S. S., Vadali, S. R., and Alfriend, K. T., "Formation Flying: Accomodating Nonlinearity and Eccentricity Perturbations," *Journal of Guidance, Control, and Dynamics*, Vol. 26, No. 2, March–April 2003, pp. 214–223.

[66] Gurfil, P., "Relative Motion Between Elliptic Orbits: Generalized Boundedness Conditions and Optimal Formationkeeping," *Journal of Guidance, Control, and Dynamics*, Vol. 28, No. 4, July–August 2005, pp. 761–767.

[67] Sengupta, P., Sharma, R., and Vadali, S. R., "Periodic Relative Motion near a Keplerian Elliptic Orbit with Nonlinear Differential Gravity," *Journal of Guidance, Control, and Dynamics*, Vol. 29, No. 5, September–October 2006, pp. 1110–1121.

[68] Junkins, J. L., Akella, M. R., and Alfriend, K. T., "Non-Gaussian Error Propagation in Orbital Mechanics," *Journal of the Astronautical Sciences*, Vol. 44, No. 4, October–December 1996, pp. 541–563.

[69] Junkins, J. L., "How Nonlinear Is It?" *Advances in the Astronautical Sciences*, Vol. 115, 2003, pp. 3–52.

[70] Alfriend, K. T., Yan, H., and Vadali, S. R., "Nonlinear Considerations in Satellite Formation Flying," *AIAA/AAS Astrodynamics Specialist Conference*, Monterey, CA, August 5–8 2002.

[71] Sengupta, P., Vadali, S. R., and Alfriend, K. T., "Second-Order State Transition for Relative Motion near Perturbed, Elliptic Orbits," *Celestial Mechanics and Dynamical Astronomy*, Vol. 97, 2007, pp. 101–129.

[72] Alfriend, K. T., Schaub, H., and Gim, D.-W., "Gravitational Perturbations, Nonlinearity and Circular Orbit Assumption Effects on Formation Flying Control Strategies," *Advances in the Astronautical Sciences*, Vol. 104, 2000, pp. 139–158.

[73] Schaub, H., Vadali, S. R., Junkins, J. L., and Alfriend, K. T., "Spacecraft Formation Flying Control using Mean Orbit Elements," *Journal of the Astronautical Sciences*, Vol. 48, No. 1, January–March 2000, pp. 69–87.

[74] Alfriend, K. T. and Yan, H., "An Evaluation and Comparison of Relative Motion Theories," *Journal of Guidance, Control, and Dynamics*, Vol. 28, No. 2, March–April 2005, pp. 254–263.

[75] D'Amico, S. and Montenbruck, O., "Proximity Operations of Formation-Flying Spacecraft using an Eccentricity/Inclination Vector Separation," *Journal of Guidance, Control, and Dynamics*, Vol. 29, No. 3, May–June 2006, pp. 554–563.

[76] Eckstein, M. C., Rajasingh, C. K., and Blumer, P., "Colocation Strategy and Collision Avoidance for the Geostationary Satellites at 19 Degrees West," *International Symposium on Space Flight Dynamics*, 1989.

[77] Griffith, J. D., Singh, L., and How, J. P., "Optimal Microsatellite Cluster Design for Space-Based Tracking Missions," *AIAA Guidance, Navigation and Control Conference and Exhibit*, Hilton Head, SC, August 20–23 2007.

[78] Eyer, J. K., Damaren, C. J., Zee, R. E., and Cannon, E., "A Formation Flying Control Algorithm for the CanX-4&5 Low Earth Orbit Nanosatellite Mission," *Space Technology*, Vol. 27, No. 4, 2007, pp. 147–158.

[79] Roscoe, C. W. T., "Reconfiguration and Recovery of Formation Flying Spacecraft in Eccentric Orbits," M.A.Sc. Thesis, University of Toronto, Toronto, Canada, June 2009.

[80] Yan, H., Alfriend, K. T., Vadali, S. R., and Sengupta, P., "Optimal Design of Satellite Formation Relative Motion Orbits using Least-Squares Methods," *Journal of Guidance, Control, and Dynamics*, Vol. 32, No. 2, March–April 2009, pp. 599–604.

[81] Hughes, S. P., "General Method for Optimal Guidance of Spacecraft Formations," *Journal of Guidance, Control, and Dynamics*, Vol. 31, No. 2, March–April 2008, pp. 414–423.

[82] Battin, R. H., *An Introduction to the Mathematics and Methods of Astrodynamics*, American Institute of Aeronautics and Astronautics, Inc., Reston, VA, Rev. ed., 1999.

[83] Schaub, H. and Junkins, J. L., *Analytical Mechanics of Space Systems*, American Institute of Aeronautics and Astronautics, Inc., Reston, VA, 2003.

[84] Gim, D.-W. and Alfriend, K. T., "Criteria for Best Configuration and Sub-Optimal Reconfiguration for MMS Mission," *Advances in the Astronautical Sciences*, Vol. 119, 2004, pp. 947–968.

[85] Hughes, S. P., "Formation Design and Sensitivity Analysis for the Magnetospheric Multiscale Mission (MMS)," *AIAA/AAS Astrodynamics Specialist Conference*, Honolulu, HI, August 18–21 2008.

[86] Marti, K., *Stochastic Optimization Methods*, Springer, Berlin, Germany, 2005.

[87] Irving, R. S., *Integers, Polynomials, and Rings*, Springer, New York, NY, 2004.

[88] Paschmann, G. and Daly, P. W., *Analysis Methods for Multi-Spacecraft Data*, ESA Publications Division, Netherlands, 1998.

[89] Guzman, J. and Schiff, C., "A Preliminary Study for a Tetrahedron Formation: Quality Factors and Visualization," *AIAA/AAS Astrodynamics Specialist Conference*, Monterey, CA, August 5–8 2002.

[90] Goldstein, H., Pool, C., and Safko, J., *Classical Mechanics*, Addison Wesley, Reading, MA, 3rd ed., 2001.

[91] von Zeipel, H., "Recherches sur le Mouvement des Petites Planètes," *Arkiv för Matematik, Astronomi och Fysik*, Vol. 11–13, 1916–1917.

[92] Deprit, A., "Canonical Transformations Depending on a Small Parameter," *International Journal of Celestial Mechanics & Dynamical Astronomy*, Vol. 1, 1969, pp. 12–30.

[93] Shniad, H., "The Equivalence of von Zeipel Mappings and Lie Transforms," *Celestial Mechanics and Dynamical Astronomy*, Vol. 2, No. 1, 1970, pp. 114–120.